Vrije Universiteit Brussel

Faculty of Engineering
Department of Applied Physics and Photonics

Simulation, Fabrication and Characterization of Bragg Gratings in Microstructured Fibers for Sensing Purposes

Simulatie, Fabricage en Karakterisering van Bragg Roosters in Microgestructureerde Vezels voor Sensor Toepassingen

Graduation thesis submitted in partial fulfillment of the requirements for the degree of Master in Engineering

Sanne Sulejmani

Promotors: Prof. Dr. Ir. Francis Berghmans
Prof. Dr. Ir. Hugo Thienpont
Advisor: Ir. Thomas Geernaert

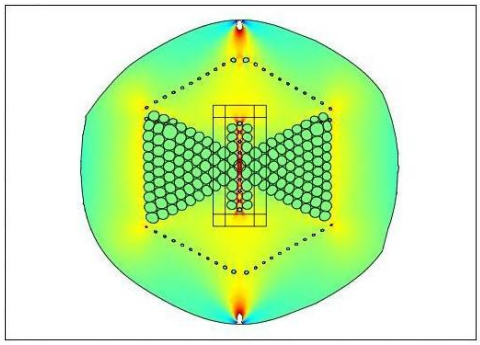

MAY 2010

Acknowledgements

When starting five years ago, I was convinced that the last year of my education would be the best. Not just because I would achieve my degree, but also because of the high level of research attached to a Master thesis.
Now, at the end of my trials, I'm happy to say it was even better than I had expected it to be. The many interesting and diverse aspects related to the subject of my thesis and the knowledge that my results can contribute to the solving of real-life problems, are some of the reasons why this year was such a great experience. It could never have been such a success without the support and opportunities provided by the people surrounding me. That's why I would like to take a moment to thank some of them.

I wish to thank my promotors Prof. Francis Berghmans and Prof. Hugo Thienpont for giving me the opportunity to do a thesis in a subject that suited my ambitions perfectly. I highly appreciated every moment you took to come by the lab, give some motivational words or attend my monthly presentations. The level of devotion you show towards your students and their work inspired me, and it was often your believe in my capabilities that moved me to work even harder. I look forward to start my PhD and career in photonics by working with you.

I like to express my gratitude to my supervisor Thomas Geernaert. Somehow you managed to always find time in your busy schedule to answer my many questions with great detail and enthusiasm. In the past year you taught me how to critically analyze results, master the fundaments of research and showed me that there is more to it than just photonics. Great thanks for all your guidance and support!

I would also like to thank the members of the jury Prof. Dr. Ir. Hugo Thienpont, Prof.

Dr. Ir. Francis Berghmans, Prof. Dr. Ir. Heidi Ottevaere, Prof. Dr. Steve Vanlanduit, Dr. Jan Van Roosbroeck and Ir. Thomas Geernaert for taking the time to evaluate my work and attending my presentation.

As a part of my thesis required knowledge of other research areas, I had the opportunity to work with people from different universities and research institutes. Many thanks to Christophe Caucheteur from UMons for the help with the grating inscription. I would also like to thank Bram Van Hoe and Peter Geerinck from CMST for the fabrication of the polymer skins, and FOS&S for letting me use their FBG scan, which greatly facilitated the testing of these photonic skins. And finally, I would like to thank Geert Luyckx, Eli Voet and Nicolas Lammens from UGent–MMS for the cooperation in the embedding of fibers in CFRP, and the extensive testing of these samples.

Special thanks to Camille Sonnenfeld for helping me out with the numerical simulations and being the extra pair of hands that were crucial whenever fibers needed to be spliced.

Besides the serious work, there also had to be some entertainment. For that I would like to thank the many fellow students and friends I had the pleasure to meet during my college-time!

And of course, the two persons who made it possible for me to study at all, my parents. You taught me that I can accomplish anything I want, as long as I work hard for it. Your everlasting support and efforts to make sure that my weekends at home felt like a stay in a five-star hotel, have always been precious to me. I would also like to thank my brother Niels, who even took the time to read my thesis.

Last but not least, I would like thank my partner Djamo. Your support over the years has meant a lot to me. Although it may seem trivial to you, it has meant the world to me that you did not once complain that we had to change plans for the weekend because of my work. And of course, thanks for the background music!

I am aware that the number of people that have contributed in some way to my education or thesis is much greater. With these closing remarks I would like to thank you all!

Summary

This Master thesis investigates a novel type of optical fiber sensors, i.e. fiber Bragg gratings written in a special design of highly birefringent photonic crystal fibers. Optical fiber sensors have many advantages such as their small dimensions and low weight, multiplexing capabilities, immunity to electromagnetic interference, ... Additionaly, they can be integrated as sensing elements in smart materials and smart structures. These are materials and structures that can respond an adapt to their environment by sensing the forces acting upon them and by continuous monitoring of their structural health. One example is a network of optical fiber sensors embedded in the wings of an airplane to monitor loading during flight. Another application is embedding optical fibers in a polymer sheet that can be used to track the movements of a patient undergoing an MRI scan. Fiber Bragg gratings are the sensor elements of choice for embedding applications. Moreover, by fabricating these sensors in microstructured (photonic crystal) fibers, their sensitivity can be tailored to the needs of a specific application.

In the first stage of this work, we inscribed fiber Bragg gratings in photonic crystal fibers. We characterized the temperature and strain sensitivity of these sensors with experiments and numerical simulations. The results we obtained show that the sensor is highly insensitive to temperature changes and features a high sensitivity to transverse line loading (–372 pm/(Nmm)) and hydrostatic pressure (–1.47 pm/bar). The ratio of these sensitivities to the temperature sensitivity, is a figure of merit for optical fiber sensors and the values we achieved have not been reported before.

We embedded this sensor in a composite material to investigate whether the high transverse line load sensitivity of the bare fiber allowed to provide a high transverse strain sensitivity when embedded in this material. This was indeed the case and we measured a transverse strain

sensitivity of –0.16 pm/$\mu\varepsilon$, which is an improvement of an order of magnitude with respect to earlier reported values of fiber Bragg grating sensors fabricated in highly birefringent fibers and embedded in composite materials.

We also embedded the sensor in biocompatible polymers for applications in the field of healthcare ('artificial optical skins'). With experiments and 2D finite element analyses, we showed that the transverse load sensitivity of an embedded sensor is higher for polymers with a lower elastic modulus, which indicates that the sensitivity is not limited by the flexibility of the polymer.
In addition, we investigated the relation between the sensitivity of the sensor and the position of the skin on which the transverse strain is applied. The results we obtained, show that by embedding the sensor in a polymer foil, an artificial optical skin is created that can be used to monitor pressure distributions in applications like body mapping.

In summary, we have shown

- a fiber Bragg grating sensor that is insensitive to temperature and has a high transverse line load sensitivity (–372 pm/(N/mm)) and hydrostatic pressure sensitivity (–1.47 pm/bar). These sensitivities have not been achieved before and almost reach the value of –2 pm/bar that the industry requires.

- that this sensor can be embedded in composite materials and provides a high transverse strain sensitivity when embedded. We measured a transverse strain sensitivity of –0.16 pm/$\mu\varepsilon$, which is ten times higher than previous reported results.

- that this sensor can be embedded in biocompatible and flexible polymer foils. From the performed experiments we can conclude that this sensor can be used in artificial optical skins to monitor pressure distributions acting upon them.

Samenvatting

Optische vezelsensoren voor slimme materialen

Optische vezelsensoren

Optische vezels geleiden licht omwille van totale interne reflectie die ontstaat door het verschil in brekingsindex n van de kern en de mantel van de vezel. Ze hebben allerlei toepassingen, en een daarvan zijn de optische vezelsensoren. Licht in een vezel wordt gekarakteriseerd door intensiteit, golflengte, fase en polarisatie. Externe invloeden zoals temperatuur en krachten beïnvloeden deze parameters waardoor ze gebruikt kunnen worden als basis voor een sensor. Optische vezelsensoren hebben verscheidene voordelen: ze zijn compact, flexibel en zeer licht, ze zijn immuun voor elektromagnetische interferentie en kunnen gemultiplexed worden wat zeer voordelig is in gedistibueerde meetsystemen. De unieke combinatie van al deze voordelen maakt optische vezelsensoren zeer interessant voor domeinen zoals lucht- en ruimtevaart, bouwconstructies of biomedische toepassingen.

Een ander zeer groot voordeel van optische vezelsensoren is dat ze gebruikt kunnen worden in zogenaamde slimme materialen. Dit houdt in dat de sensoren ingebed zijn in een materiaal zodat ze krachten hierop inwerkend kunnen opmeten. Er zijn verschillende toepassingen van zulke slimme materialen, maar mijn thesis richt zich vooral op het inbedden van Bragg rooster sensoren in composiet materialen of (flexibele) polymeren.

Composiet materialen

Composiet materialen bestaan uit versterkingsvezels (koolstof, glas, ...) die zich in een matrix materiaal (epoxy, polyester, ...) bevinden, en worden ook wel vezelversterkte materialen genoemd. Ze hebben het voordeel dat ze licht zijn, maar toch ook zeer sterk, en worden

daarom vaak gebruikt in grote constructies, zoals vliegtuigen, windmolens en bruggen.
De composiet materialen zijn enkel zeer sterk in de richting van de versterkingsvezels, en in de andere richtingen kan er bijgevolg makkelijk schade optreden. Deze schade is niet zichtbaar voor het blote oog, maar kan wel catastrofale gevolgen hebben aangezien ze de stevigheid van een constructies sterk verminderen. Door optische vezelsensoren in te bedden in deze materialen, zou schade vroegtijdig opgemerkt kunnen worden. Bovendien zouden deze sensoren continu de belasting van de constructies kunnen opmeten, zodat er voortdurend een betrouwbare schatting gemaakt kan worden van de overblijvende levensduur van de constructie.

Flexibele optische huid

Een andere toepassing van slimme materialen is in artificiële 'optische huiden', die rond bewegende of grillige objecten gewikkeld kunnen worden om de krachten te meten die hierop inwerken. Optische vezelsensoren zijn hiervoor voordelig omdat ze zeer compact zijn en gemultiplexed kunnen worden. Deze optische huiden kunnen dan gebruikt worden in biomedische toepassingen zoals 'body mapping' om de bewegingen op te volgen van een patient die een MRI scan ondergaat. Een ander voordeel van het inbedden van een optische vezelsensor in een flexibele folie is dat deze ook bescherming biedt aan de breekbare vezel. Bovendien zou voor specifieke toepassingen de elektronische aansturing en uitlees-unit ook ingebed kunnen worden in de folie, zodat er enkel nog een conventionele elektonische connectie voorzien moet worden naar de optische huid toe. Dit maakt het concept zeer toegankelijk voor niet-gespecialiseerd personeel.
Polymeren zijn de materialen bij voorkeur voor optische huiden, omdat de eigenschappen ervan aangepast kunnen worden naargelang de toepassing. Zo kunnen polymeren inert en biocompatibel zijn en kan hun flexibileit sterk variëren.

Bragg roosters in dubbelbrekende microgestructureerde vezels

De focus van mijn thesis ligt op Bragg rooster sensoren die gebruikt kunnen worden om temperatuur of rek op te meten. Een Bragg rooster in een optische vezel werkt als een spiegel voor een welbepaalde golflengte ('Bragg golflengte'), terwijl alle andere golflengtes gewoon

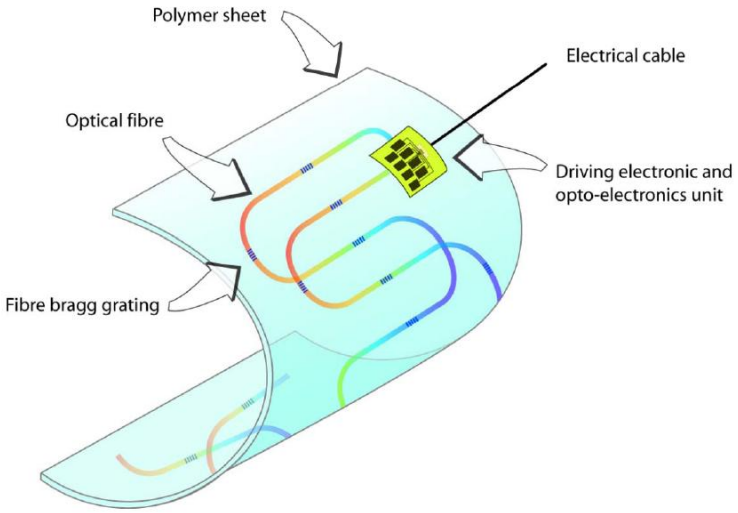

Figure 1: Concept tekening van een flexibele optische huid waarin meerdere optische vezelsensoren (Bragg roosters) zijn ingebed. [11]

doorgelaten worden. Als er een breedbandig spectrum in de vezel gestuurd wordt, dan zal een Bragg piek gecentreerd rond deze Bragg golflengte gereflecteerd worden en dezelfde piek ontbreekt in het transmissie spectrum. In Fig. 2 is het principe weergegeven.
Een rooster wordt gefabriceerd door over een lengte van enkele millimeters de brekingsindex van de kern periodisch te moduluren. De Bragg golflengte λ_B wordt bepaald door de periode Λ van de brekingsindex modulatie Δn en de effectieve brekingsindex $n_{eff} = (n + (n + \Delta n))/2$ van de kern, en de relatie is $\lambda_B = 2n_{eff}\Lambda$.De periode Λ of effectieve brekingsindex n_{eff} verandert onder invloed van temperatuur of rek en daarom kan een Bragg rooster gebruikt worden als sensor voor temperatuur en rek.

Het type vezel dat in dit werk gebruikt wordt, is een microgestructureerde vezel, of fotonische kristalvezel, waarbij de kern bestaat uit silica en de mantel uit een microstructuur van luchtgaten in silica. Deze luchtgaten verlagen de gemiddelde brekingsindex van de mantel zodat er een aangepaste vorm van 'totale interne reflectie' optreedt. Door het aantal, de positie en grootte van de luchtgaten aan te passen, kan een vezel gefabriceerd worden met allerlei specifieke eigenschappen. Een mogelijkheid is om de microstructuur tweevoudig asymmetrisch te maken waardoor de vezel dubbelbrekend wordt. Dit betekent dat licht aan de ingang van een vezel opgesplitst wordt in twee orthogonaal gepolarizeerde modes die elk een verschillende fase snelheid hebben. Dubbelbreking wordt niet alleen veroorzaakt door een tweevoudige

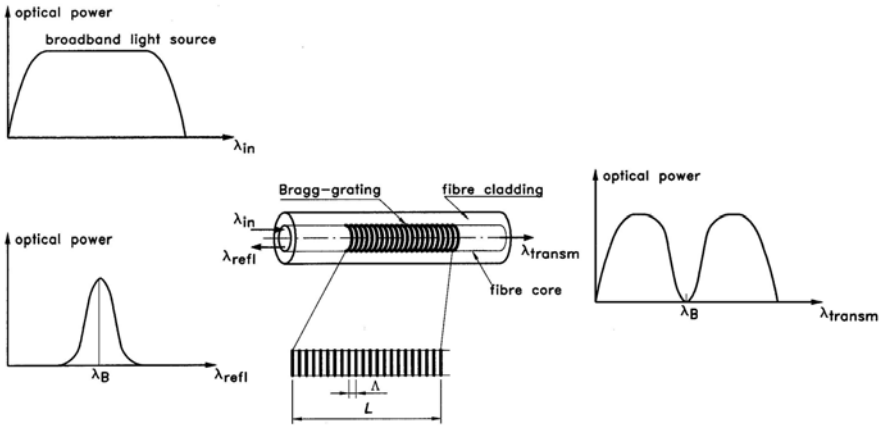

Figure 2: Een Bragg rooster is een periodische modulatie van de brekingsindex van de kern van een optische vezel. Dit rooster werkt dan als een spiegel voor een welbepaalde golflengte (λ_B) en laat alle andere golflengtes gewoon door. [8]

asymmetrie van de microstructuur, maar ook door een asymmetrische kern. Deze bijdrage aan de totale modale dubbelbreking wordt 'golfgeleider dubbelbreking' genoemd. Er is ook een bijdrage van materiaal dubbelbreking die veroorzaakt wordt door anisotropie van het materiaal die kan ontstaan door er een kracht op te plaatsen (stress-optisch effect).

De combinatie van een Bragg rooster in een dubbelbrekende vezel, zorgt ervoor dat het rooster twee Bragg pieken gecentreerd rond golflengtes $\lambda_{B,fast}$ en $\lambda_{B,slow}$ zal reflecteren. Beide Bragg pieken kunnen anders reageren op externe invloeden zoals rek en temperatuur, en daarom kan het verschil $\Delta\lambda = \lambda_{B,slow} - \lambda_{B,fast}$ ook gebruikt worden als sensor voor temperatuur of rek.

Sensor concept en objectieven

De Bragg golflengte $\lambda_{\mathrm{B}} = 2n_{eff}\Lambda$ is afhankelijk van temperatuur T en rek ε omdat zowel n_{eff} als Λ hiervan afhankelijk zijn. De verandering in Bragg golflengte $\delta\lambda_{\mathrm{B}}$ door een verandering in temperatuur δT of rek $\delta\varepsilon$ wordt gegeven door:

$$\delta\lambda_{\mathrm{B}} = 2\left(n_{\mathrm{eff}}\frac{\partial\Lambda}{\partial\varepsilon} + \Lambda\frac{\partial n_{\mathrm{eff}}}{\partial\varepsilon}\right)\delta\varepsilon + 2\left(n_{\mathrm{eff}}\frac{\partial\Lambda}{\partial T} + \Lambda\frac{\partial n_{\mathrm{eff}}}{\partial T}\right)\delta T \tag{1}$$

De thermische bijdrage aan $\delta\lambda_{\mathrm{B}}$ wordt bepaald door de thermische expansie van de vezel en

verandering in effectieve brekingsindex (thermo-optische effect) door opwarming. De invloed van de thermische expansie is vooral afhankelijk van het materiaal, terwijl het thermo-optisch effect sterk beïnvloed wordt door de aanwezigheid van thermische stress in de vezel.
$\delta\lambda_B$ is ook afhankelijk van de rektoestand van de vezel. Zo zal axiale rek vooral ten uiting komen in een toename van rooster periode Λ, terwijl een transversale kracht tot verschillende effecten kan leiden.

Voor een dubbelbrekende vezel zijn zowel $\lambda_{B,fast}$ als $\lambda_{B,slow}$ afhankelijk van temperatuur en rek en deze afhankelijkheid moet niet hetzelfde zijn voor beide golflengtes. Centraal in deze thesis staat een sensor die onwtorpen is zodat $\lambda_{B,fast}$ en $\lambda_{B,slow}$ dezelfde verschuiving ondergaan ten gevolge van een temperatuursverandering of aangelegde axiale rek, terwijl ze zich anders gedragen voor transversaal aangelegde krachten. Dit betekent dus dat de Bragg piek separatie enkel verandert onder invloed van transversale krachten. Dit concept is weergegeven in Fig. 3.

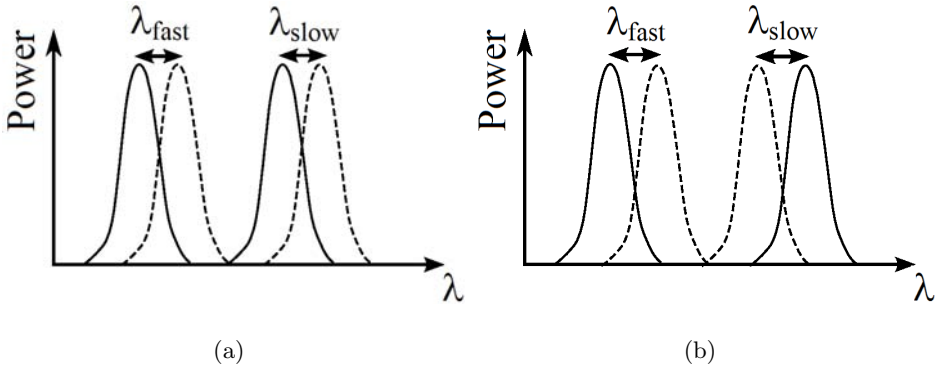

(a) (b)

Figure 3: Invloed van (a) temperatuursveranderingen en axiale rek, of (b) transversale lijnbelasting op de Bragg pieken en piek separatie van dubbelbrekende vezel.

In een eerste fase van mijn Master thesis voer ik onderzoek naar de gevoeligheid van Bragg roosters gefrabriceerd in verschillende types dubbelbrekende microgestructureerde vezels. Met experimenten en numerieke analyses, zal hun gevoeligheid voor temperatuur, axiale rek, hydrostatische druk en een transversale lijnbelasting bepaald worden. Enkele van de getestte sensoren zijn ontworpen om een hoge gevoeligheid te hebben van de Bragg piek separatie voor hydrostatische druk en een transversale lijnbelasting, terwijl deze (bijna) ongevoelig moeten

zijn voor temperatuurschommelingen.

De sensoren zullen ingebed worden in composiet materialen om na te gaan of de verhoogde gevoeligheid voor transversale lijnbelasting van de sensor zelf, leidt tot een verhoogde gevoeligheid voor transversale belasting wanneer de sensor is ingebed in een composiet materiaal. De gevoeligheid van de ingebedde sensoren voor veranderingen in temperatuur of aangelegde axiale rek wordt ook onderzocht.

Uiteindelijk zullen de sensoren ook ingebed worden in flexibele polymeren om een 'optische huid' te vormen. De invloed van de materiaaleigenschappen en dikte van het polymeer op de gevoeligheid van de ingebedde sensor zal onderzocht worden.

Fabricage en karakterisering van een optische vezelsensor

In totaal werden er vier types dubbelbrekende vezels getest. Drie ervan zijn microgestructureerde vezels die dubbelbrekend zijn omwille van een asymmetrische microstructuur en kern ('Type 1, 2 en 3 PCF'). Een ander type vezel is een bow-tie vezel, die dubbelbrekend is omwille van thermische stress geïnduceerd door de aanwezigheid van twee materialen met een verschillende thermische expansiecoëfficiënt. In Fig. 4 worden de verschillende types getoond, samen met de aanduiding van de richting waarin de 'fast' en 'slow' modes gepolarizeerd zijn.

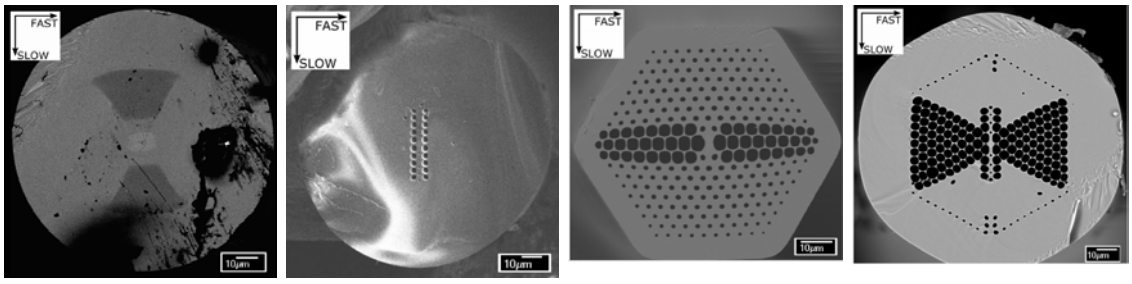

(a) (b) (c) (d)

Figure 4: Verschillende types dubbelbrekende vezels worden getest: (a) bow-tie vezel, (b) Type 1 PCF, (c) Type 2 PCF en (d) Type 3 PCF.

De sensoren werden gefabriceerd door Bragg roosters in de vezels te schrijven. Hun reflectiespectra toonden aan dat de Bragg piekseparatie voor een bow-tie vezel slechts 0.3

nm is, terwijl dit voor de microgestructureerde vezels ongeveer 2 nm is.

Een temperatuurstest toonde aan dat een sensor gefabriceerd in een Type 3 PCF, een zeer lage temperatuursgevoeligheid heeft voor de Bragg pieken ($\sim$ 9 pm/°C), terwijl de Bragg piekseparatie nauwelijks beïnvloed wordt (Fig. 5(a)). Vergeleken met eerder gerapporteerde resultaten over sensoren gefabriceerd in andere types dubbelbrekende vezels is dit een zeer lage gevoeligheid.

Simulaties (en eerder uitgevoerde experimenten) hebben aangetoond dat de Bragg piek separatie van een sensor gefabriceerd in een Type 3 PCF een zeer hoge gevoeligheid heeft voor hydrostatische druk en de piekseparatie afneemt met -1.5 pm/bar (Fig. 5(b)). Ook sensoren gefabriceerd in Type 2 PCFs hebben een hoge drukgevoeligheid voor de Bragg piek separatie (-1.2 pm/bar). Bovendien is uit eerdere experimenten gebleken dat deze gevoeligheid onafhankelijke is van de temperatuur.

Via experimenten en numerieke simulaties werd een transversale lijnbelasting aangelegd op een sensor gefabriceerd in een Type 3 PCF, en dit onder verschillende hoeken op de vezel (Fig. 5(c)). Dit resulteerde in een gevoeligheid die sterk afhankelijk is van orientatie van de vezel. Een maximale gevoeligheid van -372 pm/(N/mm) voor de Bragg piek separatie werd gevonden als een belasting wordt aangelegd volgens de 'slow' richting (180°).

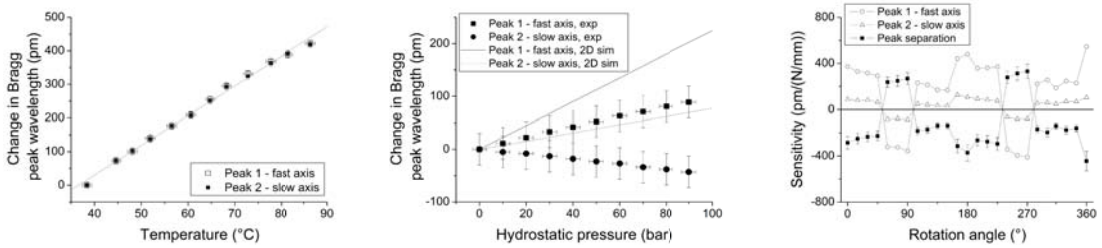

(a) (b) (c)

Figure 5: Gevoeligheid van de Bragg pieken van een sensor gefabriceerd in een Type 3 PCF (a) voor temperatuur, (b) voor hydrostatische druk en (c) voor een transversale lijnbelasting die is aangelegd op de vezel onder verschillende hoeken.

De gevonden resultaten toonden aan dat een Bragg rooster gefabriceerd in een Type 3 PCF

gebruikt kan worden voor temperatuursongevoelige metingen van transversale lijnbelastingen. Nooit eerder werden zulke hoge waarden gerapporteerd voor de temperatuursongevoeligheid en gevoeligheid voor transversale lijnbelasting van een Bragg rooster sensor.

Optische vezelsensoren ingebed in composiet materialen

Bragg sensoren gefabriceerd in een Type 3 PCF werden ingebed in koolstofvezel/epoxy composiet materialen met een 'cross-ply' opbouw bestaande uit 16 lagen, waarbij de sensor ingebed werd in het midden (Fig. 6(a) en 6(b)). De vezels werden ingebed met de 'fast' richting parallel met het sample-oppervlak. Vergelijking van de reflectie spectra voor en na embedding toonde aan dat de delicate vezels het inbeddingproces hadden overleefd en dat de Bragg piek separatie afgenomen was door de aanwezigheid van residuele stress in het composiet na fabricage. Nadat alle andere testen uitgevoerd waren, werden de samples doorgesneden om de orientatie van de ingebedde sensor na te gaan en dit toonde aan dat de vooraf aangeduidde orientatie goed behouden blijft (Fig. 6(c)).

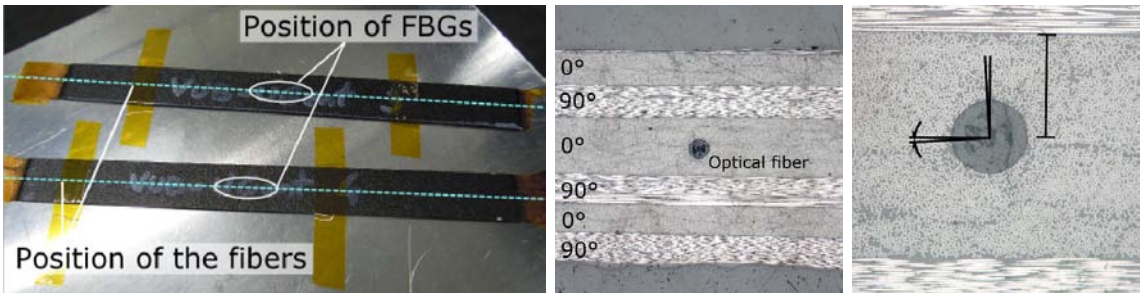

(a) (b) (c)

Figure 6: (a) Gefabriceerde composiet samples met een ingebedde sensor, waarbij de orientatie van de sensor (b en c) gecontroleerd kan worden met een destructieve test nadat alle andere testen uitgevoerd waren.

De samples werden onderworpen aan een temperatuurstest die uitgevoerd werd met behulp van een autoclaaf waarvan de temperatuur gecontroleerd kon worden (Fig. 7(a)). Uit de resultaten bleek dat de Bragg piek separatie van de ingebedde sensoren niet langer ongevoelig is voor temperatuur, deze nam namelijk toe met 4.4 pm/°C. Dit is een gevolg van de residuele stress die afneemt wanneer de samples opgewarmd worden, maar ook weer toenemen zodra

ze afgekoeld worden.

Een test waarbij axiale rek werd aangelegd op de samples (Fig. 6(b)) toonde aan dat de axiale gevoeligheid van de sensor zelf of ingebed in een composiet materiaal niet sterk verschilt. De Bragg piek separatie is dan ook ongevoelig voor axiale belasting van een composiet materiaal.

In een laatste reeks testen werd de gevoeligheid van de ingebedde sensoren voor een transversale belasting bepaald (Fig. 6(c)). De resultaten toonden aan dat de Bragg piek separatie afneemt met -24.4 pm/MPa, en dit komt overeen met -0.16 pm/$\mu\varepsilon$ als de elasticiteit modulus gelijk genomen wordt aan die van het matrix materiaal, namelijk epoxy ($E = 6.3$ GPa).

(a) (b) (c)

Figure 7: Opstellingen om de gevoeligheid van de sensor ingebed in een composiet materiaal te testen voor (a) temperatuur, (b) axiale rek en (b) transversale belasting.

Tabel 1 geeft een overzicht van de gevonden gevoeligheden van sensoren gefabriceerd in een Type 3 PCF en ingebed in een composiet materiaal. Alhoewel de Bragg piek separatie onafhankelijk is van de temperatuur voor de sensor zelf, is dit zeker niet het geval voor een sensor ingebed in een composiet materiaal. Dit geeft aan dat er een andere methode gebruikt moet worden om temperatuursonafhankelijke metingen uit te kunnen voeren.
De hoge gevoeligheid voor transversale lijnbelasting van de sensor zorgt wel voor een verhoogde gevoeligheid voor transversale belasting van de ingebedde vezel. De gevoeligheid van de Bragg piek separatie van -0.16 pm/$\mu\varepsilon$ is minstens tien keer hoger dan eerder gerapporteerde waarden voor sensoren gefabriceerd in bow-tie vezels of Type 1 PCFs, die

ingebed waren in een composiet sample met unidirectionele opbouw.

Table 1: Gemiddelde gevoeligheid van de Bragg sensoren ingebed in composiet materialen voor (a) temperatuur, (b) axiale rek en (c) transversale belasting.

	Temperatuur (pm/°C)	Axiale rek (pm/$\mu\varepsilon$)	Transversale belasting (pm/$\mu\varepsilon$)
piek 1 (fast)	3.92	1.22	0.25
piek 2 (slow)	8.35	1.21	0.10
piek separatie	4.42	-0.01	-0.16

Optische vezelsensoren ingebed in polymeren

Het inbedden van optische vezelsensoren in (flexibele) polymeren is onderzoek dat nog maar recent gestart is. In mijn Master thesis heb ik me dan ook gefocust op de mogelijkheden om de vezels in te bedden in verschillende soorten polymeren met zeer verschillende materiaaleigenschappen. Van deze verschillende samples heb ik dan de gevoeligheid van de ingebedde sensor bepaald.

Om na te gaan wat de invloed van de elasticiteitsmodulus is op de gevoeligheid van een ingebed Bragg rooster, werden er simulaties en experimenten uitgevoerd op bow-tie vezels en Type 3 PCFs die ingebed waren in een polymeer staafje met verschillende elasticiteitsmoduli (Fig. 8(a)). Uit transversale lijnbelasting proeven is gebleken dat de gevoeligheid van de sensor afneemt wanneer deze is ingebed in een polymeer staafje. Bovendien neemt deze gevoeligheid nog af wanneer het polymeer een hogere elasticiteitsmodulus heeft.

Sensoren gefabriceerd in Type 2 en Type 3 PCFs werden ingebed in een polymeer laag om een 'optische huid' te vormen (Fig. 8(c)). Twee soorten polymeer werden gebruikt, namelijk PDMS dat een zeer flexibel materiaal is, en Ormocer dat een harder materiaal is. Deze samples werden getest door op verschillende posities een gewicht van 0.45 N neer te laten (Fig. 8(b)) en de uitwijking van de Bragg pieken te registreren. In Fig. 9 wordt de uitwijking weergegeven van beide Bragg pieken en de piek separatie, als het gewicht op verschillende posities neergelaten wordt. Hierin is duidelijk te zien dat op de positie van de ingebedde

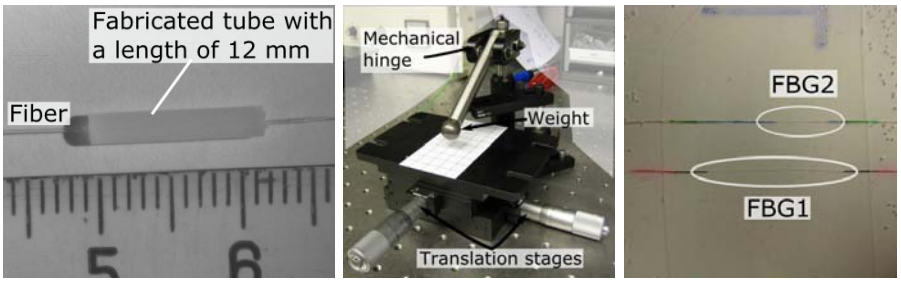

(a) (b) (c)

Figure 8: (a) Een Bragg grating sensoren ingebed in een polymeer staafje. (b) Om grotere folies te testen wordt een optstelling gebruikt waarbij een gewicht van 0.45 N op verschillende posities geplaatst kan worden. (c) Een voorbeeld van twee sensoren ingebed in een folie van PDMS.

sensor de verandering in Bragg piek golflengte het grootst is. Bovendien is er ook een (kleine) verhoogde gevoeligheid van de Bragg piek separatie op de positie van de sensor.

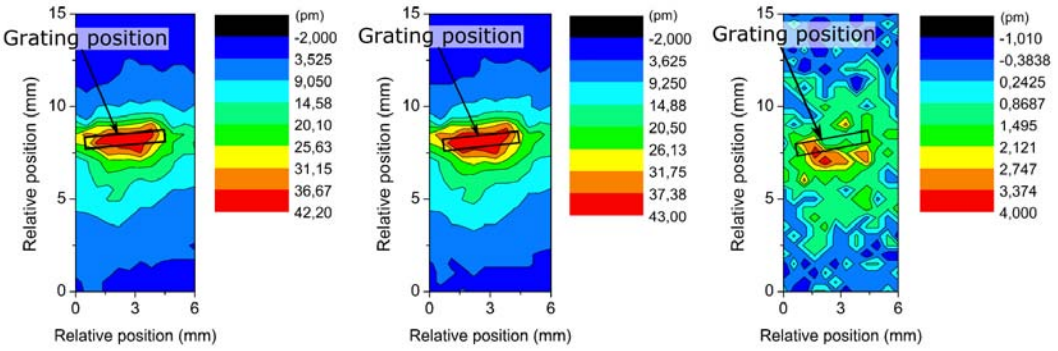

(a) (b) (c)

Figure 9: Deze grafieken geven de verschuiving van de Bragg golflengten weer als er een gewicht van 0.45 N geplaatst wordt op verschillende posities van de folie. (a) Bragg piek 1 (fast), (b) Bragg piek 2 (slow) en (c) Bragg piek separatie.

Conclusie

In mijn Master thesis heb ik aangetoond dat door het ontwerp van een microgestructureerde vezel aan te passen er sensoren in gefabriceerd kunnen worden die een hoge gevoeligheid hebben voor hydrostatische druk of transversale lijnbelasting, en bijna ongevoelig zijn voor temperatuur. Deze sensoren kunnen ingebed worden in composiet materialen, waar ze leiden tot een zeer hoge gevoeligheid voor transversale belasting hebben. Dit zou een oplossing kunnen bieden om de belastingen en schade die het composiet materiaal ondervinden, op te volgen. Bovendien heb ik aangetoond dat deze sensoren ingebed kunnen worden in flexibele 'optische huiden' en dat deze gebruikt kunnen worden voor het opmeten van drukverdelingen die inwerken op grote en grillige oppervlakken.

Résumé

Les capteurs à fibres optiques présentent de nombreux avantages tels que leurs faibles dimensions et poids, leur capacité de multiplexage et leur immunité face aux interférences électromagnétiques. Ces fibres optiques offrent également l'avantage de pouvoir être intégrées dans des matériaux: on forme alors des matériaux intelligents. Il s'agit de matériaux dotés de la capacité de diagnostic de leur santé structurale en temps réel et en continu par l'intermédiaire de capteurs en fibres optiques, insérés dans la masse. Une des applications possibles de ce type de structure est un réseau de capteurs à fibres optiques intégré dans une aile d'avion permettant le monitorage des forces s'exerçant sur l'aile pendant le vol. Un autre d'exemple d'application est l'intégration de fibres optiques au sein de fines feuilles de polymères afin de suivre les mouvements d'un patient au cours d'un examen IRM. Les fibres à réseaux de Bragg présentent toutes les qualités requises pour être intégrées dans des matériaux. De plus, en réalisant ces capteurs dans des fibres microstructurées (fibres à cristal photonique), on peut modifier la sensibilité des fibres et l'adapter à une application particulière.

Dans la première partie de ce travail, les fibres à réseaux de Bragg ont été fabriquées dans des fibres à cristal photonique. Ces capteurs ont été soumis Ã différents tests afin de caractériser leur sensibilité face à des sollicitations thermomécaniques (changement de température, déformations axiale et transversale). Les résultats expérimentaux et ceux provenant des simulations numériques montrent, tout d'abord, une grande insensibilité du capteur vis-à-vis de la température. Ils présentent également une sensibilité élevée du capteur face à une contrainte transversale.

Ensuite, le capteur est intégré dans un matériau composite pour comparer la sensibilité de la fibre seule soumise à une contrainte transversale par rapport à la sensibilité obtenue après

intégration dans le composite. Le capteur intégré dans le composite a été soumis à une contrainte transversale. Cette dernière présente une sensibilité plus importante que celle de la fibre seule et environ dix fois plus élevée que celle précédemment reportée dans des études antérieures.

Finalement, le capteur est intégré dans de fines et flexibles feuilles de polymères reproduisant une 'peau optique'. Divers types d'échantillons ont été testés (différents types de polymères) afin de déterminer l'influence du module élastique sur la sensibilité de la fibre intégrée. Ces tests et les simulations numériques montrent que le capteur est plus sensible quand il est intégré dans un polymère de faible module élastique. De plus, la sensibilité en fonction de la position du point d'application de la force (plus ou moins éloignée du capteur) a été étudiée. On a ainsi mis en évidence que la sensibilité du capteur est très dépendante des propriétés et dimensions du polymère. Ce concept de 'peau optique' est très récent et pour le moment très peu de résultats ont été publiés.

Contents

Chapter 1

Introduction

Optical fiber sensors have revolutionized the field of measurement science and technology. They have enabled a realm of new applications and they have brought tremendous added value to numerous other applications. One can think of distributed measurements since multiple sensors can be fabricated in one single fiber, aerospace where small dimensions and low weight are of importance, oil pipelines and fuel tanks where electrical sparks could have catastrophic consequences, ... In several of these applications it would be even more advantageous to embed the fiber optic sensors in a material or inside the structure itself. For example, load monitoring of mechanical structures or buildings will be more reliable when the internal strain field is directly monitored as opposed to attaching a sensor to the surface that can only estimate the internal strains.

Fiber Bragg grating (FBG) sensors are the sensors of choice for embedding purposes as they can sense multi-axial strain fields and temperature. When combined with photonic crystal fibers (PCF), the sensitivities of the FBG sensor can be tailored to the needs of a specific application. My Master thesis focuses on FBG sensors fabricated in highly birefringent (HiBi) PCFs that are intended to have an enhanced transverse line load and hydrostatic pressure sensitivity. These sensors can be used in their bare state, but also when embedded in different types of materials. More specifically, we will investigate the possibilities of embedding the sensors in carbon fiber reinforced polymers (CFRP) and different types of (flexible) polymers. Via experiments and simulations, the strain sensitivity of the embedded fiber will be determined and from these results a conclusion will be drawn on whether the enhanced transverse line load sensitivity of the bare fiber is an added-value for embedded optic fiber sensor systems.

1.1 Outline

This work starts with three introductory chapters. Chapter 2 gives a brief review of fiber optic sensors and touches upon the market aspects. A very interesting application of optical

fiber sensors are the so-called smart materials and structures, and this concept will also be explained in chapter 2 with an emphasis on structural health monitoring and artificial optical skins.
In chapter 3 the necessary theoretical aspects of FBGs and PCFs wil be explained. The working principle of FBG sensors is discussed together with their fabrication methods. PCFs are used here because their properties can be tuned with an unprecedented design freedom by adapting their microstructure. The details of their unusual features, such as a high birefringence, are also discussed in this chapter.

The last introductiory chapter, chapter 4, deals with the sensor concept we envisioned in this work. The principles of multi-parameter sensing with FBG sensors fabricated in HiBi PCFs will be discussed in more detail. Chapter 4 concludes with an elaborate description of the objectives of my Master thesis.

Chapter 5 starts with a detailed description of the characteristics of the different fiber types that are tested and the grating inscription in these fibers. The fabricated sensors are tested for their thermal sensitivity and an overview is given of previous reported axial strain and hydrostatic pressure sensitivities. The transverse line load sensitivity is determined with experiments and 2D numerical simulations. A short conclusion is drawn to indicate the added value of the tested sensors.

The subject of chapter 6 is the embedding of the FBG sensor in CFRP. First, several sensors are embedded in CFRP samples. These samples are then subjected to temperature, axial strain and transverse strain tests. Afterwards, cross-sections of the samples are made to verify the orientation of the embedded fiber and to evaluate the effects of the embedding process on the fiber sensor.

In chapter 7, the sensor is embedded in a completely different type of material: flexible polymers. To determine the influence of the embedding material on the sensitivity of the fiber sensor, several polymers with different mechanical properties are investigated. This is done via experimental characterizations and numerical simulations.

Finally, in chapter 8 I draw conclusions regarding the obtained results and the possibilities for or advantages of embedding the sensor in different materials. I will also discuss future prospects and provide hints towards possible improvements of the sensor itself and of the embedding techniques.

Chapter 2

Optical fiber sensors for smart materials

2.1 Optical fiber sensors

2.1.1 Optical fibers

An optical fiber is a thin strand of silica (or plastic) that consists out of a core and a surrounding cladding. Light entering the core of the fiber under a small angle ($< \theta_{CA}$) is guided in the core by means of total internal reflection, caused by the refractive index difference between the core and cladding of the fiber (typical values in conventional fibers: $n_{core} \approx 1.48$, $n_{cladding} \approx 1.46$). This principle is shown in Fig. 2.1.
Optical fibers can be classified according to their guiding characteristics. Depending on the number of modes they can confine, they are called 'single mode' or 'multimode'. Single mode fibers typically have a core diameter of several micrometers (~ 8 μm), while the core diameter of a multimode fiber can reach tens of micrometers ($\sim$ 50-100 μm). The cladding diameters for both types of fibers are often 125 μm, but smaller or larger cladding diameters are also used. A protective (often acrylate-based) layer 'the buffer' can be added around the cladding to protect the (brittle) fiber against mechanical actions and environmental conditions (e.g. water, chemicals, ...).

Light guided in an optical fiber has a modal behaviour, with every mode characterized by a mode profile and wavenumber $k = 2\pi/\lambda$, with λ the free space wavelength. In a circular waveguide each mode is degenerate as two orthogonal polarized modes exist for each wavenumber.
Although the light is guided mainly in the core of the fiber, a small part of the mode profile extends into the cladding. This has an influence on the refractive index n that the mode sees, as both the refractive index of the core and of the cladding influence the propagation constant $\beta = kn_{eff} = 2\pi n_{eff}/\lambda$. Therefore one speaks of the effective refractive index n_{eff}

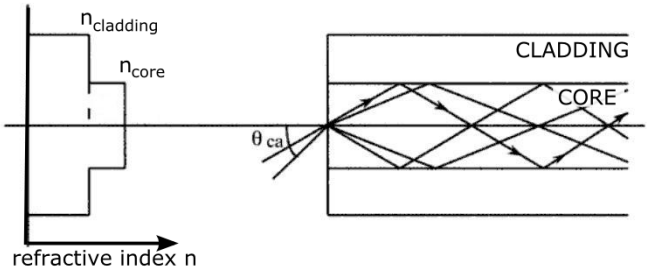

Figure 2.1: Light entering an optical fiber under an angle smaller than the critical angle θ_{CA} is guided in the core by means of total internal reflection caused by a refractive index difference between the core and cladding.

of a propagating mode in an optical fiber.

Optical fibers are ubiquitous nowadays, with applications ranging from high speed data carriers for telecommunication to high power lasers for material processing. Another application of optical fibers lies in optical metrology where a change in environmental parameters (strain, temperature, chemical composition, ...) corresponds to a change in the properties of the guided light. These are the optical fiber sensors.

2.1.2 Sensor configurations and types

There are several different ways to produce a sensor in or from an optical fiber and they can be classified in several categories depending on their configuration and implementation [1], [2]. A first subdivision is in intrinsic sensors, where the measurand interacts with the light guided in the optical fiber, or extrinsic sensors, where the light is coupled out of the fiber to and from an interaction region where the light beam is influenced by the measurand.

Optical fiber sensors can also be classified according to their implementation as a point sensor, as a distributed sensor or as a quasi-distributed sensor, as shown in Fig. 2.2. One speaks of a point sensor if the measurement is performed at only one specific location in the fiber or at the end of the fiber. Sensors where the measurement is performed along the entire length of the fiber are called distributed sensing systems. A quasi-distributed sensing system is a combination of the previous configurations, and consists of multiple point sensors located at different positions in the same fiber.

A third subdivision can be made depending on the modulation principle. Light guided in the core of an optical fiber has several properties that can be used for sensing purposes. If the fiber is bended or twisted, the intensity of the light will vary ('intensiometric sensors'). The mode guided in a fiber has a certain phase that can be used in interferometric setups ('interferometric sensors'). The difference in phase velocity between two orthogonally polarized modes propagating in the fiber can also be used as a sensing principle ('polarimetric

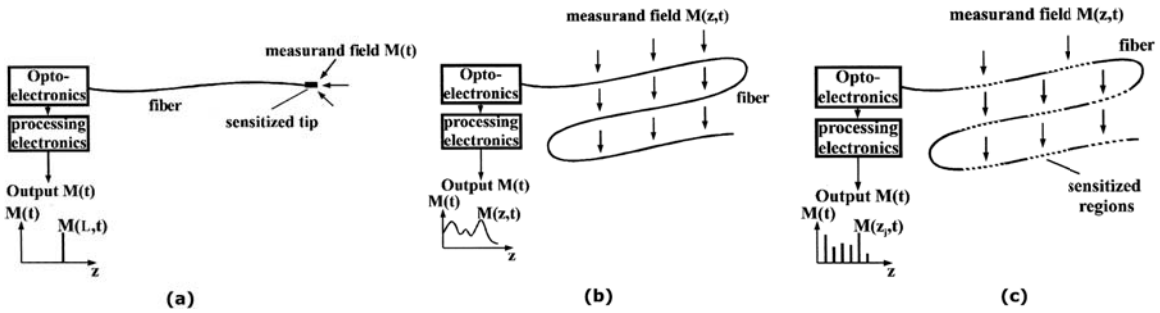

Figure 2.2: Sensor configurations: (a) Point sensor, (b) Distributed sensor and (c) Quasi-distributed sensor. [1]

sensors'). The wavelength of the guided light can also change due to absorption or fluorescence ('spectroscopic sensors').

Based on the classification system itself, one can conclude that there are many different types of optical fiber sensor. Some examples will be discussed in more detail to show the variety of sensing principles and possible applications.

- Fiber optic gyroscope
  - A fiber optic gyroscope is an all-fiber interferometer, which is based on the Sagnac effect (Fig. 2.3). Light is launched into a fiber loop in two directions. When the loop rotates, light travelling in the same direction as the rotation will propagate over a longer distance and thus longer time, than light travelling in the counterdirection. This time difference will result in a specific fringe pattern when the two light beams are combined again. [2]
  Fiber optic gyroscopes are very robust systems as they have no moving parts and are not affected by accelerations or vibrations. This makes them very popular in navigation systems for cars, airplanes or ships.

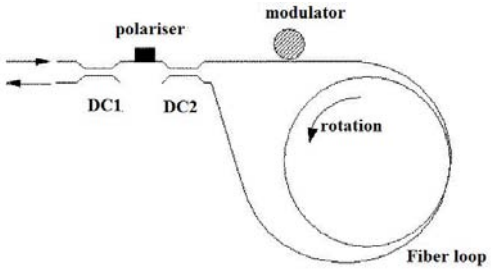

Figure 2.3: Principle of a fiber optic gyroscope. [2]

- Fiber optic Fabry Pérot interferometer
  - A fiber optic Fabry Pérot interferometer is obtained if light is coupled out of the fiber,

into a cavity with at the end a reflecting surface or fiber, such that light is reflected and coupled back into the fiber (Fig. 2.4). Depending on the length or depth of the cavity, the ratio of the power of the light entering the fiber (mode_{in}) and the power of the light reflected from the end facet of the cavity (mode_{out}) will vary, as this ratio is dependent on the phase difference between the two modes. [1]
There are different types of setups for fiber optic Fabry Pérot interferometers, and some of their applications are pressure or strain sensing.

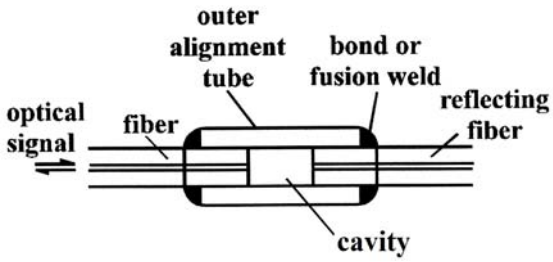

Figure 2.4: Principle of a fiber optic Fabry Pérot interferometer. [1]

- Fiber Bragg grating sensor
  - In a fiber Bragg grating, the sensor is created by locally modulating the refractive index of the core of the fiber. If this refractive index variation is periodic, a wavelength selective mirror is formed ('Bragg grating'); when broadband light is coupled in the fiber, the Bragg grating will reflect only a narrow part of the spectrum and this part is centered around the Bragg wavelength λ_B (Fig. 2.5). This Bragg wavelength will shift when the fiber Bragg grating undergoes a change in strain (axial, transverse or radial) or temperature [1]. This shift forms the basis of fiber Bragg grating sensors and the focus of this Master thesis is on this type of fiber sensor.

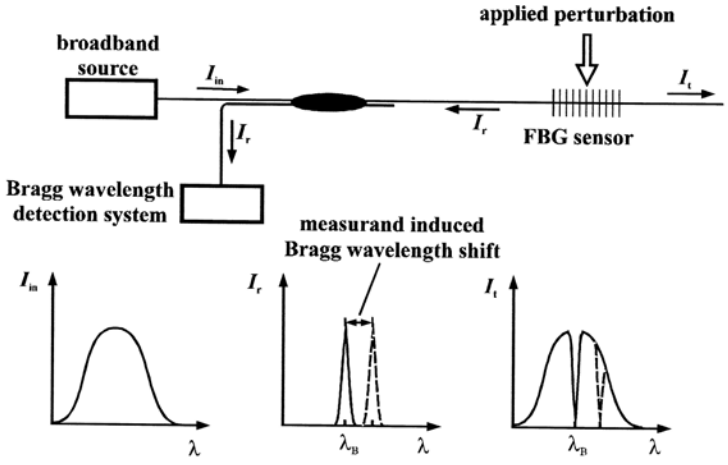

Figure 2.5: Principle of a fiber Bragg grating. [1]

2.1.3 (Dis)advantages and economical aspects

Optical fiber sensors have turned into an economic success story because of their long list of advantages and because they can be deployed in situations where conventional sensors are no longer functioning properly. [1], [2], [3], [4]
For applications such as aerospace, the weight and compactness of a sensing system is of high importance. Building a distributed strain measurement system based on conventional electrical strain gauges, requiring up to four electrical wires for each strain gauge, results in a large and heavy bundle of wires. Fiber optic sensors are low weight, flexible and compact. They can be multiplexed to form (quasi) distributed systems, with very low optical loss as they are intrinsic sensors. Optical fiber sensors can also withstand a high number of loading cycles at high strain (e.g. in [4] 10 million loading cycles), making them a possible candidate for long term load measuring.
Other unique advantages of optical fiber sensors, is that they are immune to electromagnetic interference (EMI) and can be deployed in explosion hazardous, chemical aggresive or nuclear environments. This creates the possibility to perform measurements at nuclear waste sites, in oil pipelines or fuel tanks where electrical sensors cannot be used because of possible sparks and on windmills where the performance of electrical sensors would suffer from lightning strikes.

There are also some disadvantages to optical fiber sensors, but most of these can be overcome with the necessary research and investments [2], [5].
Optical fibers are very brittle 'objects' that can break easily when handled without proper care. Installing fiber based sensing systems therefore requires trained personnel. A disadvantage that is inherent to fiber optic sensors is their cross-sensitivity, i.e. the measured signal is a combination of several measurands. For example, a sensor that is sensitive to both strain and temperature requires a temperature compensating system when only strain is of interest.

The high installation cost of fiber optic systems where they have no real added value might be another drawback. It is therefore often said that the key to success of optical fiber sensors will be in those applications where conventional fibers are inadequate.

In Fig. 2.6 an overview is given of the different application fields of optical fiber distributed sensing systems, and their corresponding market share. Although the global market for fiber optic sensors has strongly increased over the last years, market penetration is still slower than expected in many areas [5]. This is mainly due to lack of awareness by the industry and a shortage of regulations. Some industries are not aware of the benefits that optical fiber sensors have, resulting in a misinterpretation of the rather high initial cost attached to them. Industry coordination, meaning defining a common language and understanding of optical

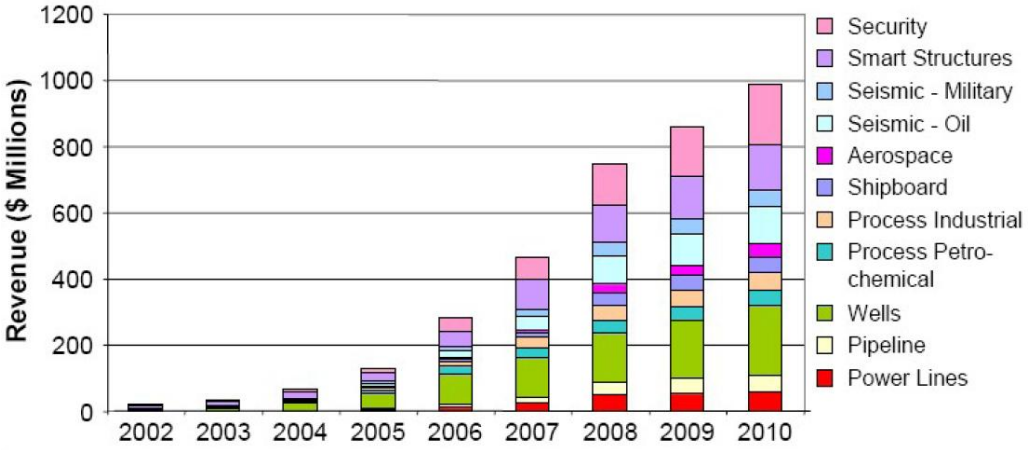

Figure 2.6: Application fields and market share of distributed fiber optic sensors. [3]

fiber sensors, would encourage the use of optical fiber sensors. This was for example initiated by COST Action 299 "FIDES" (European Cooperation in Science and Technology, Optical FIbres DEdicated to Society) which has contributed to develop standards and regulations regarding optical fibers [6].

2.2 Smart materials

A very specific advantage of fiber Bragg grating (FBG) sensors that has not been mentioned yet, is that they can be embedded inside a material or structure. This introduces several new opportunities, especially in the field of smart materials and smart systems.

A smart system consists of sensors and actuators that are embedded in or attached to a structure, such that it can 'interact' with external influences, i.e. the smart system senses something and possibly even reacts in an appropriate way [7]. The sensing part is done by a so-called smart-material, for which embedded optical fibers are an excellent candidate. The combination of the unique properties of optical fiber sensors (immune to EMI, light weight, multiplexed and distributed systems, ...) and the wide range of materials in which they can be embedded (polymers, composite materials, concrete, clay, ...) result in a long list of possible application areas.

The focus of this work will be on fiber Bragg grating sensors embedded in composite materials (fiber reinforced polymers) and polymers. A short overview of both materials and their possible applications as smart material is given below.

2.2.1 Optical fiber sensors embedded in composite materials

Introduction

Many buildings or mechanical constructions that have been operational over several years have exceeded their design lifetime and some even show signs of deterioration. This raises the question of safety of these constructions. This is especially the case for composite structures, as the long-term behaviour of these materials in real situations is still very unpredictable. Moreover, the initial damage to a composite construction does not have to cause any trouble, but as this damage will grow over time, the consequence on the structural integrity can be catastrophic. It is therefore crucial to be able to (continuously) estimate the remaining lifetime of a construction. Continuously observing the structural integrity of a building or construction, is referred to as 'structural health monitoring' (SHM) or in short 'monitoring'. In Fig. 2.7 a schematic view is given of SHM installation on a bridge.

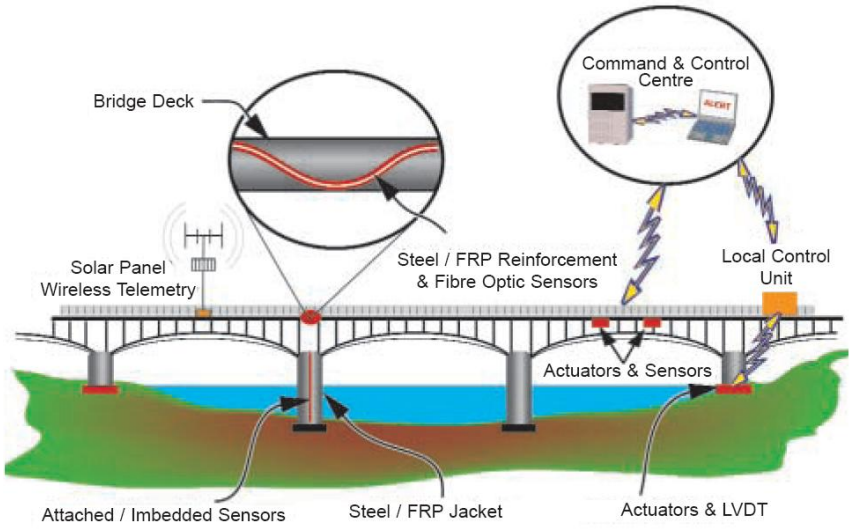

Figure 2.7: A schematic view of a smart bridge with fiber optic sensors embedded in FRP structures. [7]

Today, the surveillance of (composite) structures is based mostly on (regular) visual inspections and more specific non-destructive tests such as ultrasonic inspection, acoustic emission or radiography. These various inspection techniques are labour intensive and require specialized personnel. Moreover, there is always the risk of suffering large damage in between inspection rounds. Additionally, the structure can not be operational during such an inspection, resulting in a high financial impact.
This is why branches such as aerospace or infrastructure construction are highly interested in other non-destructive inspection techniques that can continuously monitor parameters such as vibrations, deformations or damage (growth). Optical fiber sensors, for example, are a promising candidate for such applications.

Continuously monitoring structures would result in less or no visual inspections and would allow making a sensible estimation of the remaining lifetime of these structures at all time. Moreover, monitoring the effective loading of a structure could lead to a better insight in the long-term behaviour of composite structures. This would result in an enhanced confidence in the usage of composite materials, which up untill now has been farely limited despite the numerous advantages composite materials have to offer.

Composite Materials

A composite is a heterogenous material consisting out of two or more materials that remain clearly distinguishable on a macroscopic level. The best known example is fiber reinforced polymer (FRP): by embedding reinforcement fibers in a polymer (matrix), its mechanical properties can be improved. There are different types of reinforcement fibers (glass, carbon, organic, ...), each having their own specific properties and applications. The matrix can consist of either thermosetting or thermoplastic polymers, and examples are epoxy, polyester and nylon.
The reinforcement fibers are there to absorb the load, while the matrix protects and bundles the fibers, and redistributes the introduced load.

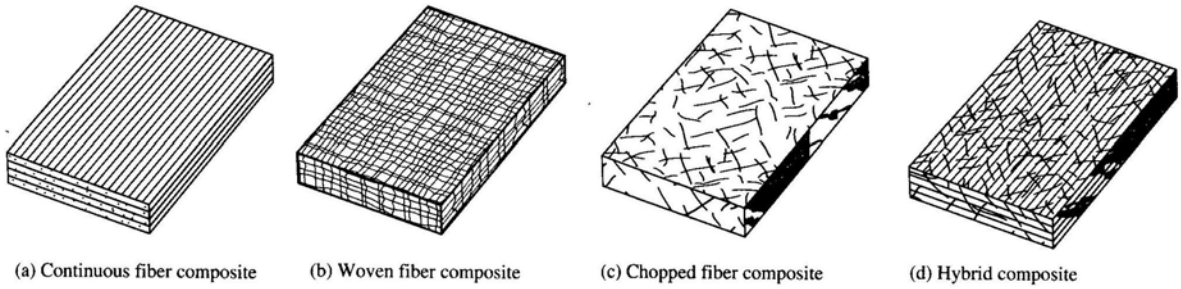

Figure 2.8: (a) Continuous fiber composite has individual fiber/matrix lamina, with continuous unidirectional reinforcement fibers. (b) Woven fiber composites do not always have distinct lamina and have a lower strength and stiffness than continuous fiber laminates. (c) Chopped fibre composites have short fibres randomly dispersed in the matrix and their mechanical properties are considerably poorer than those of continuous fiber composites. (d) Hybrid composites may consist of mixed chopped and continuous fibers, or mixed fiber types. [8]

It is this combination of reinforcement fibers in a matrix, that gives a composite material very specific mechanical properties (high strength and stiffness) compared to other, more traditional materials like steel or concrete. This means that composite structures weigh much less, while being as strong as they would be if they were made from other materials. However, a composite is intrinsically anisotropic, meaning that it only has a high specific stiffness and strength in the direction of the reinforcement fibers, while these are low in the directions

perpendicular to those fibers.
Stacking different layers ('laminae') of composite on top of each other ("to laminate"), with a different orientation of the reinforcement fibers in each layer, increases the specific strength and stiffness in multiple directions. One can tune the pattern of the laminate to the stress field in the component of interest. In Fig. 2.8 various types of composites are shown, with fiber directions in different well-defined or random orientations.

Because of their exceptional properties, composite materials are very interesting for applications in sportmaterials (bikes, skis, ...), aerospace, transport (cars, airplanes, ...) or construction (bridges, buildings, ...).

Influence of the embedded fiber on the mechanical properties of the composite

Optical fiber sensors could be a very interesting solution for structural health monitoring of composite structures, but they have to fulfill several requirements. It is obvious that they have to be cost-effective and easy in use, but as they remain embedded in the structure for its complete lifetime, the sensors also have to be stable and useable for a long period of time. Another important requirement is that they have to survive the fabrication process of the composite material.

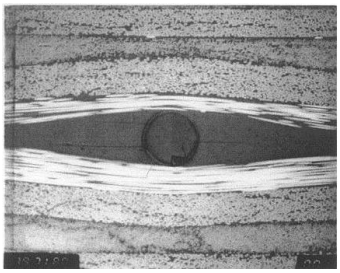

Figure 2.9: The large difference in diameter between an optical fiber and the reinforcement fibers can cause a local disturbance in the composite, forming an 'eye'. These weak zones can be avoided by embedding the optical fiber in the same direction as the reinforcement fibers. [8]

The large difference in diameter between an optical fiber ($\sim$ 125-250 μm) and the reinforcement fibers of the composite ($\sim$ 5-20 μm), can cause a local disturbance in the fiber pattern of the composite. As shown in Fig. 2.9, there can be more resin (epoxy) around the fiber than reinforcement fibers, causing a typical 'eye' in the structure. This will disturb the distribution of internal stains in the composite material, and result in a mis-interpretation of the global strain on the material by the optical fiber sensor. To ensure correct predictions of the structural integrity, these 'eyes' have to be prevented. It has been shown that when the optical fiber is embedded in the same direction as the reinforcement fibers, the disturbance is very small and has very little influence on the mechanical properties of the composite [8].

2.2.2 Optical fiber sensors embedded in (flexible) polymers

Introduction

Today, many research efforts are being put in the domain of tactile sensing, where an artificial skin is used to measure a spatial distribution of forces acting on the sensor. There are numerous applications for tactile sensors ranging from robotic fingers to body mapping and prosthetics that can adapt the shape of the socket to minimize pressure points (Fig. 2.10).

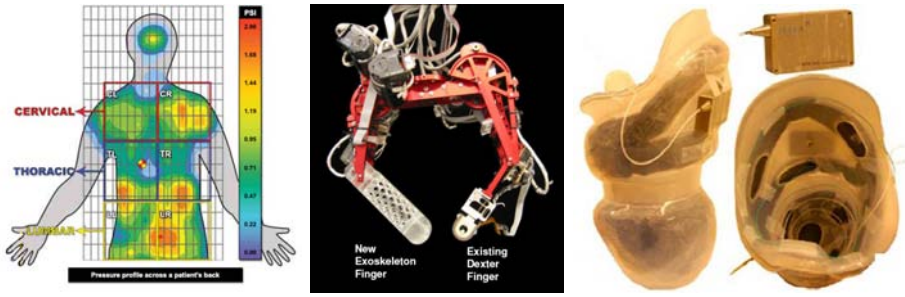

(a) (b) (c)

Figure 2.10: Some applications of tactile sensors: (a) Body mapping [9], (b) Robotics [10] and (c) Prosthetics with an adaptable socket ('Smart socket').

In certain application domains the usage of electronic skins is not preferred or simply dangereous. First of all, electrical sensors are quite bulky as each strain gauge needs four electrical contact wires. This can result in an unnatural feeling and limited flexibility of the surface, which is not ideal in applications like body mapping. The combination of electrical currents and humid environments should also be prevented at all costs as this could lead to short circuits. Moreover, since electrical sensors are not immune to EMI they cannot be used in several medical imaging applications (e.g. MRI).
An artificial skin based on optical sensors ('optical skin') would be a solution to these problems, and fiber Bragg grating sensors could replace the conventional strain gauge. By embedding FBG sensors in a flexible or stretchable foil, a tactile sensor is created that can be wrapped around, attached to or embedded in irregular shaped or moving objects to monitor pressure distribution on the surface. [7], [11]

Several FBG sensors can be multiplexed in one single fiber without significant power loss such that large sensing areas can be achieved with one single optical fiber. One of the disadvantages of optical fibers is that they are fragile and not stretchable. This problem could be solved by embedding the fiber in a meandered layout in a stretchable foil. If the application allows it, the driving electronics and opto-electronics unit can be co-embedded in the optical skin, such that the output of the artificial skin is just one electrical cable, eliminating the requirement

for specialized personnel. This optical skin concept is shown in Fig. 2.11. [11]

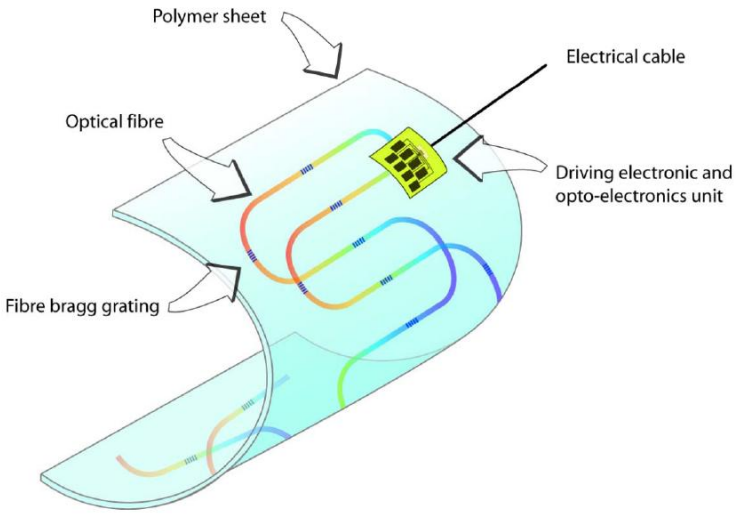

Figure 2.11: Concept of a flexible optical skin in which fiber Bragg gratings are used for quasi distributed tactile sensing. [11]

Polymers are ideal host materials for (flexible) optical skins. Silicones or methyl methacrylate (MMA) based polymers are preferred because of their tuneability and wide range of mechanical properties. Both polymer types are biocompatible and silicones are chemically inert, which makes them ideal materials for medical applications. By changing the production process of the polymers, their mechanical properties (strength, stiffness, flexibility, necking, ...) can be tuned to match the application and required sensitivity.

2.2.3 Other applications of embedded optical fiber sensors

Embedded FBG sensors are not only ideal for tactile sensing, but they can also be used for more trivial purposes. As mentioned before, FBG sensors are the optical version of the strain gauge, but have the disadvantage that they are difficult to handle. There are however applications where optical strain gauges are preferable and to facilitate the handling, the FBG sensor can be embedded in a 'patch' to protect the fragile sensor and resemble an electrical strain gauge.

Another application of an embedded FBG sensor is in combination with specialized polymer coatings to create biophotonic sensors. This principle is called 'lab-on-a-fiber' and is a research area that is still little explored. A polymer can be modified such that when it is brought into contact with a certain molecule, it will shrink or expand. When an FBG sensor is embedded in that polymer, it will measure the shrinkage or expansion, and thus indicate the presence of the molecule. Applications could be testing drinking water or blood for the presence of molecules.

Chapter 3

Fiber Bragg gratings in highly birefringent photonic crystal fibers

3.1 Fiber Bragg gratings

3.1.1 Working principle

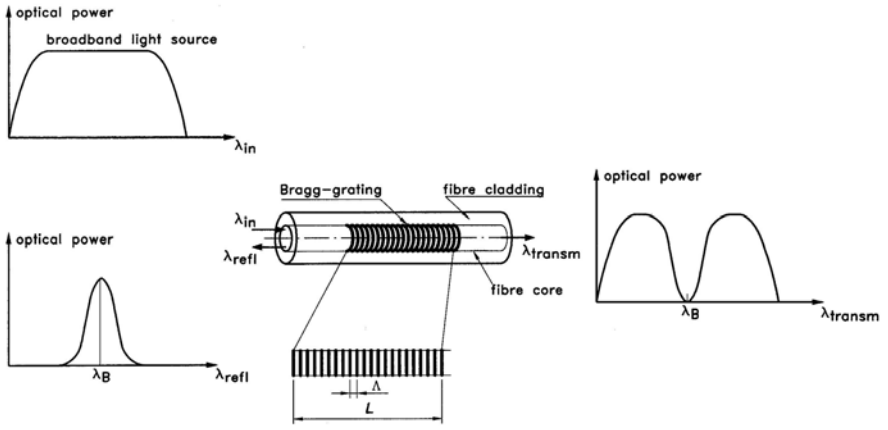

Figure 3.1: Basic principles of a fiber Bragg grating that works as a wavelength selective mirror. [8]

A fiber Bragg grating (FBG) is obtained when the characteristics of the core of an optical fiber are locally changed over a length L (typically a few millimeters). More specifically, a FBG is a periodic modulation of the refractive index, that will act as a wavelength selective mirror (Fig. 3.1). When light propagating in the fiber encounters a change in refractive index Δn, a small part of this light will be reflected, while the rest is transmitted. Consecutive refractive index changes will result in many small reflections, together forming one large reflection with reflectivity R. Moreover, if the change in refractive index is periodical with period Λ, coupling

between the forward and backward propagating mode will occur if their phases match ('phase matching condition'), i.e. $\beta_{\text{bwd}} = -\beta_{\text{fwd}}$. But β_{bwd} is determined by β_{fwd} and by the period Λ of the grating, with $\beta_{\text{bwd}} = \beta_{\text{fwd}} + \beta_{\text{FBG}}$. Combining these equations will lead to the Bragg condition, as given in equation (3.1c).

$$\beta_{\text{bwd}} = -\beta_{\text{fwd}} \ \wedge \ \beta_{\text{bwd}} = \beta_{\text{fwd}} + \beta_{\text{FBG}} = \beta_{\text{fwd}} + \frac{2\pi}{\Lambda} \tag{3.1a}$$

$$\Rightarrow 2\left(\frac{2\pi}{\lambda_{\text{B}}}\right) n_{\text{eff}} = \frac{2\pi}{\Lambda} \tag{3.1b}$$

$$\Rightarrow \boxed{\lambda_{\text{B}} = 2n_{\text{eff}}\Lambda} \tag{3.1c}$$

with λ_{B} the Bragg wavelength that is determined by $n_{\text{eff}}=\frac{n+(n+\Delta n)}{2}$ which is the effective refractive index of the core of the fiber, and Λ which is the period of the grating. When a broadband light spectrum enters the fiber, the FBG will reflect a narrow part of the spectrum centered around the Bragg wavelength λ_{B}. Both Λ and n_{eff} are influenced by strain and temperature, implying that λ_{B} is also sensitive to strain and temperature, and will change when strain or temperature varies.

In Fig. 3.2 two FBG reflection spectra are shown. Both spectra show a (broad) peak centered around the Bragg wavelength ('Bragg peak'), but some other characteristics as well. The reflectivity R and the spectral width of the Bragg peak are determined by the length L and period Λ of the grating and the amplitude of the refractive index modulation Δn in the core. Some sidelobes are also present due to the abrupt start and end of the grating.
By changing the parameters Λ and Δn of the grating, the power of the sidelobes or the spectral width of the spectrum can be reduced. Depending on whether or not they are constant, the grating can be classified under 3 types:

- Apodized: An apodized grating is created if Δn is modulated along the length, with a Gaussian or raised-cosine refractive index profile. Such a refractive index profile will result in strong sidelobe suppresion.

- Chirped: If Λ is increased over the length of the grating, a so-called chirped grating is obtained. This type of grating can be used for dispersion compensation.

- Uniform: If both Λ and Δn are constant, one speaks of a uniform grating. This type of FBG is commonly used for sensing purposes.
  Typical values for uniform gratings are a grating length L of about 1 cm, a reflectivity R of 90%, a FWHM of about 0.2 nm, and a refractive index modulation Δn of the core on the order of 10^{-5} - 10^{-4}.

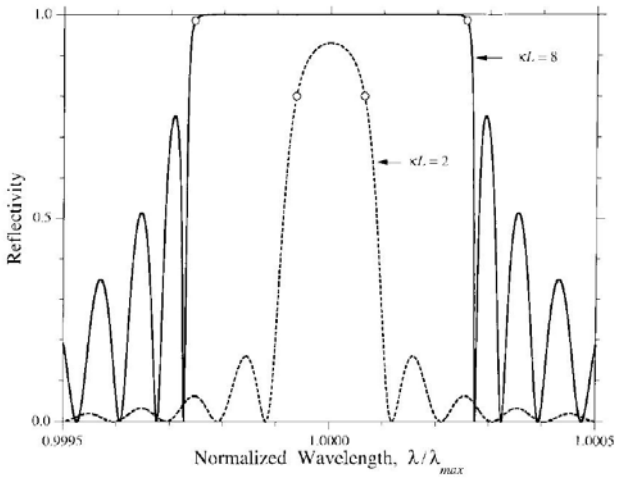

Figure 3.2: Reflection spectrum of two gratings with different parameters for grating length L, period Λ and refractive index modulation Δn of the core. [13]

3.1.2 Bragg grating inscription

Photosensitivity

By exposing silica to UV light, its refractive index will (most often) increase due to changes in the silica's chemical bonds and internal structure. The term 'photosensitivity' refers to this (permanent) change in refractive index. It is the presence of defects in the silica structure that causes a fiber to be photosensitive, but there is still much debate about the exact link between the defects and UV-induced change in refractive index, as it is not straightforward to detect all types of defects. However, there are already some important well-known defects that causes silica to be photosensitive. [12]
Silica fibers have such a high number of defects because of their specific fabrication process in which several chemical processes are involved. As these chemical reactions are never 100 % complete, suboxides and defects within the glass structure arise. As a result, the silica of a fiber is a material that is highly inhomogeneous on a microscopic scale with little order beyond the range of a few molecular distances.

The amount of defects in silica can be increased by doping it with germanium and creating GeO-type defects. These defects have an absorption peak at 240 nm, and upon UV illumination the bond of the defect will break causing a reconfiguration of the shape of the molecule and changing the densitiy of the material.
Other types of defects are Ge(n)-type of defects with an absorption peak around 213 nm or 280 nm, NBOHC-type (non-bridging oxygen-hole center) of defects with absorption peaks around 260 nm and 600 nm, and P-OHC-type (phosphorous-oxygen-hole center) of defects that are believed to absorb at 260 nm.

Another technique to increase the number of defects in Ge-doped fibers is hydrogenation to form GeH-type of defects. There are several ways to hydrogenate Ge-doped fibers, and one possibility is to H_2-load the fiber for several days at a high pressure (180-700 bar). This hydrogenation is not permanent as the hydrogen gas will outdiffuse rather quickly after hydrogen loading. This can be prevented by storing the fiber at low temperatures (-70°) since the diffusion process is temperature dependent.

Inscription techniques

Photosensitivity is exploited to change the refractive index of the fiber and create a fiber Bragg grating in the fiber by illuminating it with UV light. There are several different setups to illuminate the fiber with a periodic pattern but in general they fall into two categories: holographic or phase mask exposure. [12]

- In a holographic setup a beam splitter is used to divide a single input UV beam into two beams that recombine at the fiber and create an interference pattern.
  In the Talbot interferometric setup (Fig. 3.3(a)) a phase mask (Λ_{PM}) is used as beam splitting element and two rotatable mirrors are used to create the periodic pattern at the fiber position. The period Λ of the inscribed grating is determined by the wavelength of the UV light λ_{UV} and the half angle ϕ between the two interfering beams, and the relation is given by equation (3.2) [14]. When these mirrors are at the right angle to the axis of the fiber, the period of the inscribed grating will be half that of the phase mask. But by rotating the mirrors simultaneously in opposite directions, the period of the grating can be adjusted, making it a very favourable technique to inscribe gratings with varying λ_{B}. With this technique one can easily create arrays of gratings, i.e. multiple gratings with different λ_{B} that are inscribed close together.

$$\Lambda_{\mathrm{FBG}} = \frac{\lambda_{\mathrm{UV}}}{2\sin\varphi} \text{ and } \lambda_{\mathrm{B}} = \frac{n_{\mathrm{eff}}\lambda_{\mathrm{UV}}}{\sin\varphi} \tag{3.2}$$

  Talbot interferometry is one of the grating inscription techniques that is used for draw tower gratings (DTG). These gratings are directly inscribed in the fiber while the latter is being fabricated (Fig. 3.3(b)). This makes it possible to first inscribe the grating in the fiber, and afterwards coat the fiber so that fiber and grating are well protected. In all other situations where one wants to inscribe a grating in the fiber that is already coated, the coating will have to be removed resulting in fragile parts or the grating has to be inscribed through the coating which requires special techniques.

- In the phase mask technique the fiber is periodically exposed to a pulsed light source or through a spatially periodic mask. In section 5.3.1 this technique will be used for the fabrication of the tested sensors.

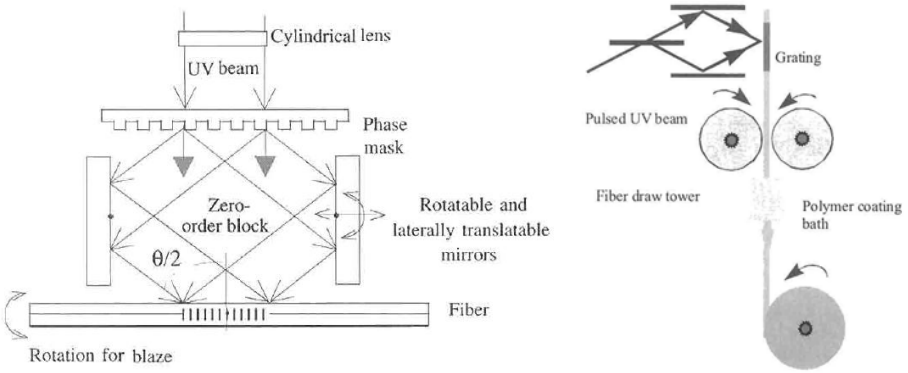

(a) (b)

Figure 3.3: (a) Talbot interferometry and (b) Setup to inscribe a grating while fiber is being drawn (Draw Tower Grating).[12]

The scanning phase mask interferometer setup (Fig. 3.4) uses a phase mask to diffract an incoming UV beam into multiple higher order beams. If the fiber is placed close to the phase mask at the position where the +1 and –1 orders intersect, a periodic pattern will appear in the fiber. This pattern results in a grating with a period equal to half that of the phase mask ($\Lambda_{\mathrm{PM}} = 2\Lambda_{\mathrm{FBG}}$). The thickness of the phase mask is chosen such that the power of the 0^{th} diffraction order is suppressed and the distance between the fiber and the phase mask is large enough to avoid interference between the higher order ($> 1^{th}$) modes.

The advantage of this setup is that the length of the grating can be controlled by translating the UV beam during inscription and is only limited by the length of the phase mask. Moreover, as there are no additional components other than the phase mask, it is a very robust and stable system, making it a good candidate for mass production of gratings. However, it is disadvantegeous that one phase mask is needed for each desired grating period and Bragg wavelength.

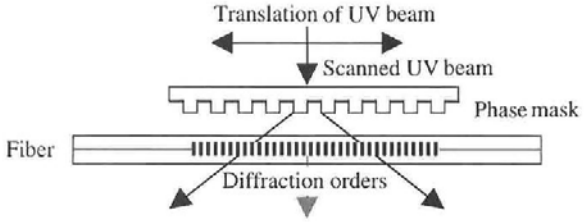

Figure 3.4: Scanning phase mask technique [12]

3.2 Photonic crystal fibers

3.2.1 Different types of photonic crystal fibers

The most common known optical fibers have a high-index solid core surrounded by a cladding of low-index material, and light propagation is based on total internal reflection. However, photonic crystal fibers (PCFs) are an alternative fiber technology. PCFs consist of a periodic arrangement of a low-index material (e.g. air) in a background of high-index material (e.g. silica), forming a so-called 2.5D photonic crystal. PCFs can be categorized under mainly two types, depending on their guiding mechanism: photonic bandgap fibers and high-index guiding fibers. In references [15], [16], [17] and [18], some excellent reviews are given on photonic crystal fibers and their sensing abilities.

Photonic bandgap fibers

The core of a photonic bandgap fiber (Fig. 3.5) has a lower refractive index (e.g. an airhole) than the surrounding photonic crystal cladding and light is guided in the core by the presence of a photonic bandgap (PBG) in the microstructured cladding. A PBG is the optical analogue of an electronic bandgap, and prohibits the propagation of a certain wavelength in a material with periodic dielectric properties. As light propagates through air, it can be used for low-loss guidance and high power applications. Another very specific application is (bio-) chemical sensing where the empty core can be filled with a gas or liquid.

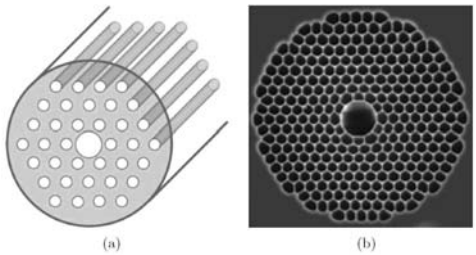

Figure 3.5: (a) Schematic of a hollow core PCF with a triangular lattice of air-holes, which guides light through the photonic bandgap effect. (b) Microscope picture of a fabricated hollow-core triangular PCF. [15]

Index guiding fibers

PCFs with a silica core and silica/air-hole microstructured cladding can guide light based on the principle of (modified) total internal reflection, because the cladding has a lower overall refractive index due to the presence of air-holes. The refractive index seen by the fundamental mode guided in the core is dependent on the refractive index of both core and cladding, and is thus highly dependent on the number, shape, size, pitch and position of the airholes in the cladding.

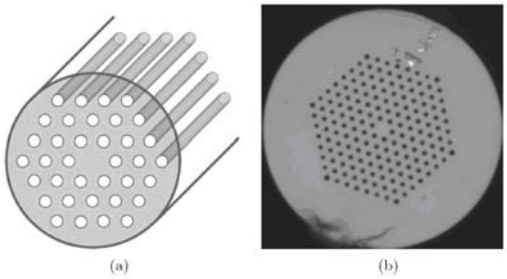

Figure 3.6: (a) Schematic of a solid-core PCF with a triangular lattice of air-holes, which guides light for (modified) total internal reflection. (b) Microscope picture of a fabricated solid-core triangular PCF. [15]

The main advantage of this type of fiber is therefore that by changing the geometry of the microstructure (adapting the size, position or number of air-holes), the properties of the PCF can strongly be tailored. For example, a triangular lattice PCF as shown in Fig. 3.6, is characterized by the air-filling fraction d/Λ of the cladding, with d the diameter of the air-hole and Λ the hole-to-hole spacing. By changing this fraction one can alter the properties of the PCF, and a few examples are given below:

- Single mode fiber: If d/Λ<0.4 the PCF is endlessly single mode, meaning that it is single mode for all wavelengths. If the air-filling fraction is increased, higher order modes will also be trapped in the core, resulting in a multimode fiber.
- Dispersion tailoring: When the PCF has a very small (solid) core, but is surrounded with very large airholes, one can shift the zero-dispersion wavelength of the PCF to the visible range.
- Large-mode area fibers: These fibers have small air-holes and large hole-to-hole distances, implying a large modal area, that is useful for high-power applications.
- Birefringent fibers: By introducing significant assymetry in the microstructure, one can create highly birefringent fibers (Fig. 3.7). This will be discussed in more detail in section 3.3.
- Low bending loss fiber: If the air-filling fraction d/Λ is large, only a small part of the light will escape the core when the fiber is bended. However, if d/Λ is small, light will not be tightly confined in the core, resulting in larger bending losses.

3.2.2 Fabrication of PCFs

The high design flexibility in PCFs is possible because of their specific fabrication method. There are different ways to fabricate PCFs, but the so-called stack and draw technique shown

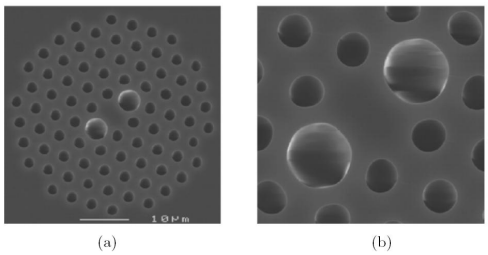

Figure 3.7: Microscope picture of (a) the cross-section and (b) the core region of a highly birefringent triangular PCF. [15]

in Fig. 3.8, is most common [15]. As for standard fibers, first there is a preform fabricated that already has the structure of interest on a macroscopic scale. In the stack-and-draw technique, this preform is obtained by stacking silica tubes and rods to form the desired structure. Some of these rods can be doped, some tubes can have thicker or thinner walls, and on some places rods or tubes can be left out.
Once the preform is ready, the fiber is drawn like a conventional fiber on a drawing tower, reducing the PCF structure to the desired size. As the fiber is heated during drawing, one has to prevent the airholes from collapsing. This is done by using a drawing temperature of only 1900°C instead of 2100°C, and by applying a slight overpressure inside the airholes during fabrication. However, it is still very difficult to maintain the circular shape and exact position of the airholes, and the eventual microstructure will be heavily dependent on fabrication parameters such as temperature, drawing speed and over- or underpressure.

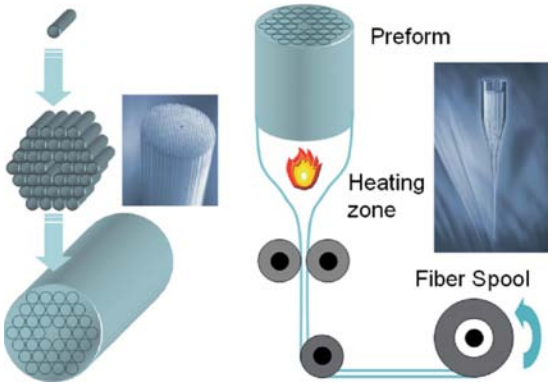

Figure 3.8: Scheme of the PCF fabrication process: a preform made with the stack-and-draw techniques is drawn to a photonic crystal fiber. [15]

3.2.3 Grating inscription in PCFs

There are some difficulties related with inscribing gratings in PCFs, because of the multiple reflections at the air/silica interfaces that cause high levels of reflected, refracted and diffracted light. Moreover, because of the microstructure there will also be rotational variance, and at

certain angles the scattering will be higher, while at other angles there can be a lensing effect. [20]
For example, in Fig. 3.9 the scattering is shown for a certain microstructure when transversely illuminated under an angle of 0° or 30°. There are clearly big differences in the scattering pattern and the illumination level in the core.

Several solutions have been proposed to overcome this problem of scattering. One could insert an index-matching fluid into the airholes to reduce the amount of scattering, but this is already a very elaborate technique [19]. The easiest way to cope with the high levels of scattering, is by Ge-doping the core of the microstructured fiber such that the photosensitivity of the core is very high and only small amounts of light are needed to change the refractive index. Not all applications of PCFs allow Ge-doping because dopants increase the transmission loss and can affect the temperature sensitivity, but this is certainly not a problem for sensing applications.

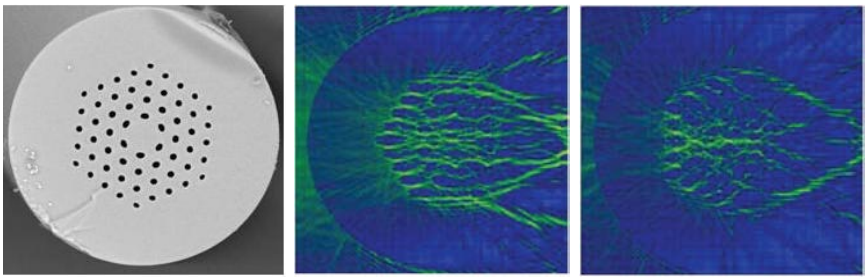

(a) (b) (c)

Figure 3.9: 193 nm light (TE) focussed and scattered within the 4-ring PCF shown in (a) illuminated under an angle of (b) 0° and (c) 90° orientations. [20]

We will see in section 5.3.1 that the PCFs studied in this Master thesis use Ge-doping and are therefore compatible with conventional UV-inscription methods.

3.3 Highly birefringent fibers

Birefringence is a waveguide or material property related with the anisotropy of the refractive index. A light ray entering a birefringent waveguide or material is decomposed into two orthonally polarized modes and both modes will see a different refractive index resulting in a different phase velocity (Fig. 3.10).

There are several birefringent crystals in nature, e.g. lithiumniobate ($LiNbO_3$), calcite ($CaCO_3$) and sapphire (Al_2O_3), but there are also several ways to make an optically isotropic material anisotropic. For example, by applying an electric field one can force the molecules to line up asymmetrically (Pockels effects), but anisotropy can also be induced by applying

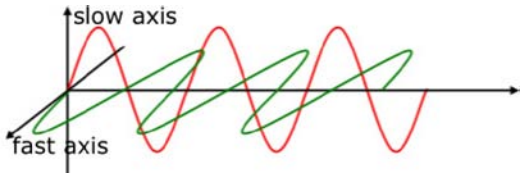

Figure 3.10: When light enters a birefringent material or fiber, it will decompose into two orthogonally polarized modes, along the fast and slow axis of the material. The phase velocity $v = c/n_{\text{eff}}$ of both modes is different.

mechanical stress on the material, via the stress-optic effect.
Since there are different types of birefringence, there are several ways to make a fiber birefringent ('highly birefringent fiber' or 'HiBi fiber'). The modal birefringence B_{modal} of a fiber is a combination of the effects listed below.

- Material birefringence B_{material}:

  - Thermal stresses can occur in the fiber after fabrication, and these stresses can result in birefringence (stress-optic effect). By introducing stress-applying parts (SAP) in the fiber, i.e. materials that have a different thermal expansion coefficient than the fiber, one can increase the amount of thermal stress and thus the level of birefringence. Examples of stress induced HiBi fibers are bow-tie or panda fibers (Fig. 3.11).

  - By applying stress directly to the fiber, one can also change the birefringence of the fiber, again because of the stress optic effect. This will later on be the basis of our sensor concept.

  In (3.3) equations are stated for the change of the anisotropic refractive index with the stress-optic effect, with C_1 and C_2 the stress optic coefficients of the fiber material, σ_1, σ_2 and σ_3 the principal components of the applied stress (direction '1'and '2' perpendicular to fiber axis, direction '3' along fiber axis) and the stress induced birefringence $B_{\text{material}}=n_1\text{-}n_2=(C_1\text{-}C_2)(\sigma_1\text{-}\sigma_2)$.

$$n_1 = n + C_1\sigma_1 + C_2(\sigma_2 + \sigma_3) \tag{3.3a}$$

$$n_2 = n + C_1\sigma_2 + C_2(\sigma_1 + \sigma_3) \tag{3.3b}$$

$$n_3 = n + C_1\sigma_3 + C_2(\sigma_1 + \sigma_2) \tag{3.3c}$$

- Waveguide birefringence $B_{\text{waveguide}}$:

  - By making the cladding asymmetric in the region around the core, the two guided modes will also see a different refractive index. This can be done in standard fibers (elliptical clad fiber), but also in high index guiding PCFs where the microstructure can be made asymmetrical by enlarging selected holes (Fig. 3.7), by removing air-holes,

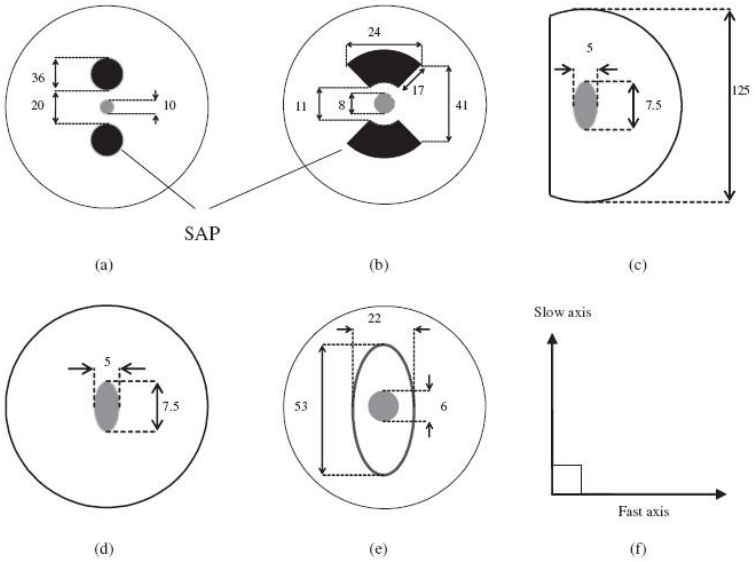

Figure 3.11: HiBi fiber cross-sectional geometry: (a) Panda and TruePhase fibers, (b) bow-tie fiber, (c) D cladding and elliptical core fiber, (d) elliptical core fiber, (e) elliptical cladding fiber and (f) polarization axes configuration. [21]

by having large airholes in one direction and small airholes in the other, ... Every symmetry lower than two-fold symmetry in the microstructure will result in waveguide birefringence B.

- By making the core asymmetrical the two modes in the core will see a different refractive index as well. An asymmetric core can be intentional e.g. an elliptical core fiber (Fig. 3.11), but can also be induced by the fabrication. As was explained in section 3.2.2, it is difficult to maintain exact geometries in PCFs during the fiber drawing. By making the microstructure of a PCF highly asymmetric, it is very likely that the core will also become asymmetrical, resulting in an increase of $B_{\text{waveguide}}$.

Both B_{material} and $B_{\text{waveguide}}$ will contribute to the overall modal birefringence in an optical fiber ('Highly birefringent fiber' or 'HiBi fiber'). The modal birefringence B_{modal}=n_{slow}-n_{fast} with n_{fast} and n_{slow} the effective refractive indices of the two fundamental modes propagating the fiber. It is the difference in phase velocity $v = \text{c}/n_{\text{eff}}$ and corresponding phase difference, that makes birefringent fibers so interesting for sensing applications. For example, they can be used as polarimetric sensor where the phase difference between the two modes measured at the end of the fiber can tell you someting about temperature changes over the whole length of the fiber.

HiBi fibers can also be used in combination with an FBG that will reflect light in both modes and thus two Bragg wavelengths (λ_{fast} and λ_{slow}) will be visible in the

reflection spectrum. Their separation $\Delta\lambda$=λ_{slow}-λ_{fast} will depend on the total birefringence B_{modal}=B_{material}+$B_{\text{waveguide}}$ of the fiber, and λ_{fast} and λ_{slow} are given by equations (3.4). Thus, if the modal birefringence B_{modal} of the fiber changes, due to stress for example, both Bragg wavelengths will change.

$$\lambda_{\text{fast}} = 2\left(n_{\text{eff}} - \frac{B_{\text{modal}}}{2}\right)\Lambda \tag{3.4a}$$

$$\lambda_{\text{slow}} = 2\left(n_{\text{eff}} + \frac{B_{\text{modal}}}{2}\right)\Lambda \tag{3.4b}$$

$$\Delta\lambda = \lambda_{\text{slow}} - \lambda_{\text{fast}} = 2\Lambda B_{\text{modal}} \tag{3.4c}$$

This mechanism will form the basis of our sensor concept, which will be explained in more detail in the next chapter.

Chapter 4

Sensor concept

4.1 Temperature and strain sensitivity of an FBG in a HiBi fiber

The Bragg condition states that $\lambda_B{=}2n_{\text{eff}}\Lambda$, with both n_{eff} and Λ dependent on temperature T and strain ε or even other perturbations. This implies that an FBG can be used as a temperature and/or strain sensor, as they both will cause a shift $\delta\lambda_B$ of the Bragg wavelength as given by equation (4.1).

$$\delta\lambda_{\text{B}} = 2\left(n_{\text{eff}}\frac{\partial\Lambda}{\partial\varepsilon} + \Lambda\frac{\partial n_{\text{eff}}}{\partial\varepsilon}\right)\delta\varepsilon + 2\left(n_{\text{eff}}\frac{\partial\Lambda}{\partial T} + \Lambda\frac{\partial n_{\text{eff}}}{\partial T}\right)\delta T \tag{4.1}$$

If an FBG is inscribed in a highly birefringent fiber, two Bragg wavelengths ($\lambda_{\text{fast}}{=}2n_{\text{fast}}\Lambda$ and $\lambda_{\text{slow}}{=}2n_{\text{slow}}\Lambda$) will be reflected by the grating, and both these wavelengths are dependent on strain and temperature. This implies that the peakseparation $\Delta\lambda{=}\lambda_{\text{slow}}{-}\lambda_{\text{fast}}$ also depends on strain and temperature, and that it can be considered to measure strain or temperature. The advantage of using $\Delta\lambda$ as sensor read-out is that this is a differential measurement where the information is contained in a difference between two values. This means that no reference wavelength is needed, there are no problems regarding drift on the read-out and the sensor does not need to be connected or monitored continuously.
Another possible advantage of using $\Delta\lambda$ as measurement signal is that it can be made (almost completely) independent of temperature changes by correctly choosing the fiber type, microstructure design and material. Strain sensors that are not affected by temperature changes have a distinct advantage as they need no temperature compensating system. This could lower the cost of a fiber sensor system, which is one of the current reasons for the limited acceptance of these sensors in industry, as explained in section 2.1.3.

In the next sections equation (4.1) will be studied in more detail in order to find the requirements for such a temperature insensitive strain sensor.

4.1.1 Response to temperature

The sensitivity of the Bragg wavelength to temperature can be found if there is no strain applied (ε_i=0). Equation (4.1) then becomes

$$\delta\lambda_{\mathrm{B}} = 2\left(n_{\mathrm{eff}}\frac{\partial\Lambda}{\partial T} + \Lambda\frac{\partial n_{\mathrm{eff}}}{\partial T}\right)\delta T \tag{4.2a}$$

$$= \lambda_{\mathrm{B}}\left(\frac{1}{\Lambda}\frac{\partial\Lambda}{\partial T} + \frac{1}{n_{\mathrm{eff}}}\frac{\partial n_{\mathrm{eff}}}{\partial T}\right)\delta T \tag{4.2b}$$

$$= \lambda_{\mathrm{B}}\left(\alpha_{\mathrm{f}} + \alpha_{\mathrm{n}}\right)\delta T \tag{4.2c}$$

There are two dominant effects influencing the Bragg wavelength when the temperature T varies. First of all, an increase in temperature causes a thermal expansion of the fiber, and thus a change in grating period Λ. The thermal expansion coefficient is given by $\alpha_{\mathrm{f}} = \frac{1}{\Lambda}\frac{\partial\Lambda}{\partial T}$ and is approximately 0.55×10^{-6} 1/K [22] for undoped silica.
Moreover, a temperature change also induces a change in refractive index, which is the so-called thermo-optic effect. $\alpha_{\mathrm{n}} = \frac{1}{n_{\mathrm{eff}}}\frac{\partial n_{\mathrm{eff}}}{\partial T}$ is the thermo-optic coefficient and its value is dependent on the dopant type and doping concentration of the silica fiber. Values between 3.0×10^{-6} 1/K and 8.6×10^{-6} 1/K [22] for germanium-doped silica-core fibers have been reported.
Equation (4.2a) can be re-written as (4.2c), with α_{f}+α_{n} the temperature coefficient in which the thermo-optic coefficient α_{n} will have the largest influence. It follows that for $\alpha_{\mathrm{f}} = 0.55\times10^{-6}$ 1/K and $\alpha_{\mathrm{n}} = 7\times10^{-6}$ 1/K at a wavelength λ of 1550 nm, the (theoretical) sensitivity of the Bragg wavelength for temperature is about 10.85 pm/K.

4.1.2 Response to strain

When the temperature T is kept constant, the Bragg wavelength is only dependent on the strain conditions and equation (4.3) can be applied.

$$\Delta\lambda_{\mathrm{B}} = 2\left(n_{\mathrm{eff}}\frac{\partial\Lambda}{\partial\varepsilon} + \Lambda\frac{\partial n_{\mathrm{eff}}}{\partial\varepsilon}\right)\Delta\varepsilon \tag{4.3}$$

Strain ε is given by a 3×3 matrix ε_{ij} (for i, j=1,2,3), with the coordinate system as depicted in 4.1. This coordinate system will be taken as convention throughout the rest of the text. Photo-elasticity, also known as the stress-optic or strain optic effect, describes refractive index changes due to mechanical strain. The change in optical permeability tensor ($\Delta\eta_i$) depends on the strain tensor (ε_j) and the strain-optic tensor (p_{ij}), and their relation is given by equation (4.4). The strain-optic tensor $\overline{\overline{p}}$ depends on the symmetry of the material, and for an isotropic material such as silica, this tensor contains only two independent coefficients p_{11} and p_{12}. The

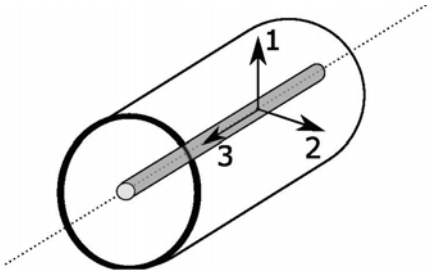

Figure 4.1: Coordinate system of an optical fiber that will be taken as convention throughout the rest of the text.

tensor itself is given by equation (4.5).
The values of the strain optic coefficients are dependent on the type of material, the doping concentration and the wavelength at which they are determined. Typical values for undoped bulk silica, measured at 630 nm, are p_{11}=0.121 and p_{12}=0.270 [22].

$$\eta_i = \eta_i^{(0)} + \Delta\eta_i \text{ with } \Delta\eta_i = \Delta\left(\frac{1}{n^2}\right)_i = p_{ij}\varepsilon_j \quad i,j = 1,2,...,6 \tag{4.4}$$

$$\overline{\overline{p}} = \begin{bmatrix} p_{11} & p_{12} & p_{12} & 0 & 0 & 0 \\ p_{12} & p_{11} & p_{12} & 0 & 0 & 0 \\ p_{12} & p_{12} & p_{11} & 0 & 0 & 0 \\ 0 & 0 & 0 & \frac{1}{2}(p_{11}-p_{12}) & 0 & 0 \\ 0 & 0 & 0 & 0 & \frac{1}{2}(p_{11}-p_{12}) & 0 \\ 0 & 0 & 0 & 0 & 0 & \frac{1}{2}(p_{11}-p_{12}) \end{bmatrix} \tag{4.5}$$

Strains normal to all surfaces of the fiber (ε_1, ε_2 and $\varepsilon_3 \neq 0$) will result in a change in refractive index along the axes as depicted in Fig. 4.1, with the principal axes corresponding to the slow and fast axis of a HiBi fiber. This change in refractive index will be translated into a shift of the Bragg wavelength(s) when an FBG is inscribed in the fiber.
Shear deformations ε_4, ε_5 and ε_6 have no effect on the first two impermeability values, p_{11} and p_{12}, and consequently also not on the refractive indices of the fiber, they cannot be measured with an optical fiber.

For small variations of the refractive index, equation (4.4) becomes equation (4.6).

$$d\left(\frac{1}{n^2}\right)_i = \frac{-2}{n_i^3}dn_i \Rightarrow \frac{-2}{n_i^3}dn_i = p_{ij}\varepsilon_j \Rightarrow dn_i = \frac{-1}{2}n_i^3 p_{ij}\varepsilon_j \tag{4.6}$$

If (4.5) and (4.6) are combined, one finds (4.7)

$$dn_1 = \frac{-n_1^3}{2}\left(p_{11}\varepsilon_1 + p_{12}\varepsilon_2 + p_{12}\varepsilon_3\right) \tag{4.7a}$$

$$dn_2 = \frac{-n_2^3}{2}\left(p_{12}\varepsilon_1 + p_{11}\varepsilon_2 + p_{12}\varepsilon_3\right) \tag{4.7b}$$

$$dn_3 = \frac{-n_3^3}{2}\left(p_{12}\varepsilon_1 + p_{12}\varepsilon_2 + p_{11}\varepsilon_3\right) \tag{4.7c}$$

From the Bragg condition one then finds (4.8), assuming that the only change in period of the grating is an increase dependent on the amount of axial strain, $\Lambda = \Lambda_0(1+\varepsilon)$.

$$\lambda_B = 2n_{eff}\Lambda \Rightarrow \frac{d\lambda_B}{\varepsilon} = 2\frac{dn_{eff}}{\varepsilon}\Lambda + 2\frac{d\Lambda}{\varepsilon}n_{eff} \tag{4.8a}$$

$$\Rightarrow \frac{d\lambda_B}{\varepsilon} = 2\frac{dn_{eff}}{\varepsilon}\Lambda + 2\Lambda n_{eff} \tag{4.8b}$$

$$\Rightarrow \frac{d\lambda_B}{\varepsilon} = \lambda_B\left(1 + \frac{1}{n_{eff}}\frac{dn_{eff}}{\varepsilon}\right) \tag{4.8c}$$

From equation (4.7) and (4.8) the equations can be derived to find the change in Bragg wavelength when a strain is applied (4.9):

$$\boxed{\frac{\delta\lambda_{\mathrm{B},1}}{\lambda_{B,1}} = \varepsilon_3 - \frac{1}{2}n_{\mathrm{eff},1}^2\left[p_{11}\varepsilon_1 + p_{12}\left(\varepsilon_2 + \varepsilon_3\right)\right]} \tag{4.9a}$$

$$\boxed{\frac{\delta\lambda_{\mathrm{B},2}}{\lambda_{B,2}} = \varepsilon_3 - \frac{1}{2}n_{\mathrm{eff},2}^2\left[p_{11}\varepsilon_2 + p_{12}\left(\varepsilon_1 + \varepsilon_3\right)\right]} \tag{4.9b}$$

In Fig. 4.2 different types of strain fields are shown and each of them will have a specific influence on the Bragg wavelength(s) of an FBG. Consequently, by studying the behaviour of the Bragg peak(s), the corresponding strain field could possibly be derived. The Bragg peak behaviour of a (HiBi) fiber under axial or transverse line loading will be discussed in more detail below.

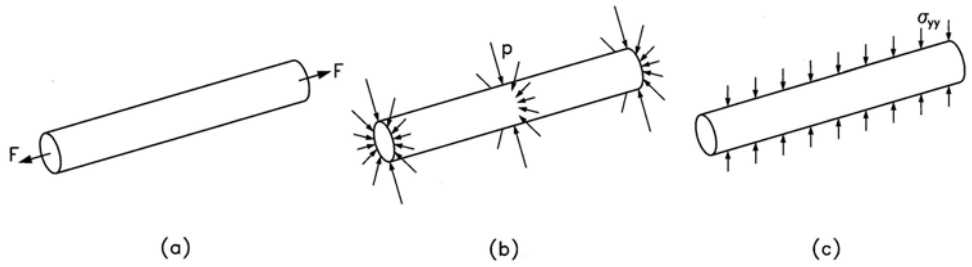

Figure 4.2: Schematic representation of different types of strain on a fiber: (a) axial strain, (b) hydrostatic pressure and (c) transverse line load. [8]

Axial strain

In the specific case that only axial stress is applied on the free standing fiber, the transverse strains ε_1 and ε_2 are a fraction of the axial strain ε_3 (4.10):

$$\varepsilon_1 = \varepsilon_2 = -\nu\varepsilon_3 = -\nu\varepsilon \tag{4.10}$$

Equations (4.9) become equation (4.11):

$$\frac{\delta\lambda_{\mathrm{B},1}}{\lambda_{\mathrm{B},1}} = \varepsilon - \frac{1}{2}n_{\mathrm{eff},1}^2\left[\nu\varepsilon\left(p_{11}+p_{12}\right)+p_{12}\varepsilon\right] \tag{4.11a}$$

$$\frac{\delta\lambda_{\mathrm{B},2}}{\lambda_{\mathrm{B},2}} = \varepsilon - \frac{1}{2}n_{\mathrm{eff},2}^2\left[\nu\varepsilon\left(p_{11}+p_{12}\right)+p_{12}\varepsilon\right] \tag{4.11b}$$

For the change in peak separation between the two Bragg wavelengths, one finds equation (4.12). From this follows that for a uniaxial fiber ($n_{\mathrm{eff},1}$=$n_{\mathrm{eff},2}$) the peak separation does not change when only axial stress is applied to the fiber. However, this is not necessarily the case for a HiBi fiber for which $n_{\mathrm{eff},1=\mathrm{fast}} \neq n_{\mathrm{eff},2=\mathrm{slow}}$.

$$\frac{\delta\lambda_{\mathrm{B},2}}{\lambda_{\mathrm{B},2}} - \frac{\delta\lambda_{\mathrm{B},1}}{\lambda_{\mathrm{B},1}} = -\frac{1}{2}\left[\nu\varepsilon\left(p_{11}+p_{12}\right)+p_{12}\varepsilon\right]\left(n_{\mathrm{eff},2}^2 - n_{\mathrm{eff},1}^2\right) \tag{4.12}$$

Transverse strain

In the specific case that the fiber is only transversely loaded, a plane strain (ε_3=0) situation is created. Equation (4.9) becomes (4.13), and from these it is clear that $\lambda_{\mathrm{B},1}$ and $\lambda_{\mathrm{B},2}$ behave differently when a transverse line load is applied, for both a non-HiBi fiber and a HiBi fiber. One can thus expect a clear change in Bragg peak separation when a transverse line load is applied to the fiber.

$$\frac{\delta\lambda_{\mathrm{B},1}}{\lambda_{\mathrm{B},1}} = -\frac{1}{2}n_{\mathrm{eff},1}^2\left[p_{11}\varepsilon_1 + p_{12}\varepsilon_2\right] \tag{4.13a}$$

$$\frac{\delta\lambda_{\mathrm{B},2}}{\lambda_{\mathrm{B},2}} = -\frac{1}{2}n_{\mathrm{eff},2}^2\left[p_{11}\varepsilon_2 + p_{12}\varepsilon_1\right] \tag{4.13b}$$

4.2 Envisioned sensor concept

In general, the goal is to achieve a sensor that is insensitive to temperature, but has a high transverse strain sensitivity. Temperature insensitivity can (possibly) be obtained by using a HiBi PCF. The birefringence leads to two Bragg wavelengths λ_{fast} and λ_{slow} and their separation $\Delta\lambda$ is the measured signal, making it a differential sensor. Photonic crystal fibers have the advantage that they have only small and slightly doped parts resulting in very small (temperature sensitive) thermal stresses. The microstructure of the PCF can be adapted such

that the fiber has a very high transverse strain sensitivity, thus that the peak separation is heavily dependent on transverse strain.

This concept is shown in Fig. 4.3. Under influence of temperature (or axial strain) both Bragg peaks shift in the same way leading to no change in peak separation, while the Bragg peaks shift in opposite direction due to transverse strains resulting in an increase or decrease in peak separation.

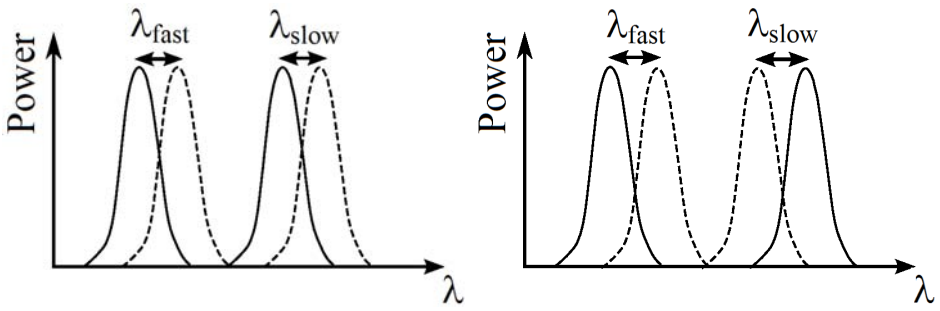

Figure 4.3: Effect on the Bragg wavelengths of an FBG in a HiBi fiber due to (a) axial strain or temperature changes and (b) transverse strain.

The second step is to exploit the high transverse line load sensitivity of the bare fiber sensor in an embedded sensor. There are several applications where embedded optical fiber sensors with an increased transverse line load sensitivity have a significant added-value, as was discussed in section 2.2.

4.3 Thesis objectives

The combination of an FBG inscribed in a HiBi PCF allows multi-parameter sensing and by careful design of the microstructure the fiber can be made very sensitive to one parameter while nearly insensitive to others. The sensor of interest in this work is designed to have a low temperature sensitivity and at the same time a high transverse strain and hydrostatic pressure sensitivity. This sensor could be used for all kinds of applications, but one of the main goals is to embed this fiber in different types of materials to create a smart material with a high transverse strain sensitivity.

In this Master thesis the sensitivity of a HiBi PCF that was specially designed to have a high transverse strain sensitivity is determined for the bare fiber, but also when it is embedded in two very different materials, i.e. polymers and composite materials. The objectives are discussed in the next section.

4.3.1 Sensitivity of the FBG sensor

State of the art

There are not many references that investigate the combination of an FBG with a HiBi PCF for transverse strain sensing purposes. Some results regarding fibers with a low temperature sensitivity and high hydrostatic pressure sensitivity, which usually corresponds to a high transverse strain sensitivity, have been reported before ([23], [24], [25]). In reference [26] a PCF is presented with two large airholes on each side of the core with a grating inscribed that should withstand high temperatures. The reported hydrostatic pressure sensitivity is on the order of 1 pm/bar, but shows a significant temperature dependence. At room temperature a sensitivity of 1.27 pm/bar is achieved, but this value is not stable and becomes about 1.4 pm/bar or 1.7 pm/bar at a temperature of 199 °C or 858 °C respectively.
An overview of the transverse line load sensitivity of different types of thermal stress-induced birefringent fibers is given in [21]. The highest line load sensitivity was obtained for an elliptical clad fiber with a maximum sensitivity of λ_{slow} of 230 pm/(N/mm) and corresponding sensitivity of $\Delta\lambda$ of about 210 pm/(N/mm). However, the temperature sensitivity of this type of HiBi fiber is also quite high, with a value of 14.5 pm/°C for λ_{slow} and 15.6 pm/°C for λ_{fast}.
The transverse line load sensitvity of a twin-hole fiber was investigated in [27], and the sensitivity of the peak separation was found to be about 212 pm/(N/mm). Values regarding the temperature sensitivity were not reported.
The line load sensitivity of another type of microstructured HiBi fiber was determined in [28], a transverse strain sensitivity of $\Delta\lambda$ of about 100 pm/(N/mm) was found. Thanks to the design of the fiber, the temperature sensitivity of the peak separation could be neglected.

Objectives

In my work, several types of HiBi (microstructured) fibers will be investigated. I will start with fabricating the sensors by inscribing gratings in the fibers and determining their temperature and strain sensitivity. This is done via experiments and FEM simulations in order to achieve a better understanding of Bragg grating sensors inscribed in HiBi fibers.
The goal is to have a differential sensor for which the peak separation $\Delta\lambda = \lambda_{\text{slow}} - \lambda_{\text{fast}}$ is (nearly) insensitive to temperature changes and at the same time has a high transverse line load or hydrostatic pressure sensitivity. The envisioned hydrostatic pressure sensitivity of $\Delta\lambda$ lies between –1 pm/bar to –1.7 pm/bar and this should correspond to a transverse line load sensitivity of $\Delta\lambda$ of around 200 pm/(N/mm).

4.3.2 FBG sensors embedded in a composite material

State of the art

Embedded FBG sensors fabricated in standard single mode fiber in various composite materials with different lay-ups, were reported in [29]. They showed that depending on the orientation of the optical fiber with respect to the reinforcement fibers, non-uniform residual strains will cause a shift of the Bragg wavelength. More specifically, it was shown that a quasi-isotropic layup of glass fibre/epoxy only caused a shift in Bragg wavelengths, while an angle-ply layup resulted in such high residual strains that the embedded fiber becomes birefringent.
Values regarding FBG sensors fabricated in a bow-tie fiber and a microstructured fiber embedded in a carbon fiber/epoxy composite with a unidirectional layup, were reported in [30]. Testing of both samples showed that their sensitivity of $\Delta\lambda$ is nearly zero for axial strain, while the transverse strain sensitivity of the peak separation was -0.022 pm/$\mu\varepsilon$ for the bow-tie embedded sample and -0.014 pm/$\mu\varepsilon$ for the embedded PCF. The temperature sensitivity differed significantly for both samples; the sensitivity of $\Delta\lambda$ was -0.42 pm/°C and 0.026 pm/°C for the embedded bow-tie fiber and PCF, respectively.

Objectives

In this Master thesis, I will investigate the possibilities of embedding an FBG sensor in a PCF with enhanced transverse line load sensitivity and a highly asymmetric microstructure, in a carbon fiber/epoxy composite. The fiber will be embedded under a welll defined orientation to optimize transverse sensitivity, and this orientation will be checked at the end with a destructive test. The first test that I will perform on these samples is a thermal sensitivity test to see whether the temperature insensitivity of the bare fiber is maintained when embedded in a composite. I expect that the axial strain sensitivity of the FBG sensor will not change dramatically when embedded, but it will be determined for completeness. Since a composite has a very high stiffness, I assume that transverse loading of a composite will result in transverse loading of the embedded sensor and thus that the high transverse line load sensitivity of the bare fiber sensor will result in a high transverse strain sensitivity of the embedded fiber sensor.

The research regarding the composites was made in cooperation with the department of Materials Science and Engineering of the university of Ghent.

4.3.3 FBG sensors embedded in a flexible polymer

State of the art

FBG sensors embedded in flexible polymer skins are a research topic that is still in its early stages and therefore good references are hard to find. Embedded FBG sensors in a fexible thin PDMS sheet for pressure sensing were reported in [31]. However, their sensing principle was not related to the strain-optic effect, but to the decrease in optical power reflected by the Bragg grating when the fiber is bended. They obtained a sensitivity of 10 % optical power loss per 10 kPa pressure and a spatial resolution of 1 cm^2.

Objectives

I will embed FBG sensors fabricated in HiBi PCFs with enhanced transverse line load sensitivity in different polymers (PDMS, MMA, ORMOCER, ...) with varying mechanical properties to determine the influence of these properties on the sensitivity of the FBG sensor. As the elastic modulus of the embedding material is quite different from the optical fiber, a transverse strain on the material will be seen by the sensor as a hydrostatic pressure rather than as a pure transverse line load. Via experimental characterizations and FEM simulations the sensitivity of the sensor will be determined for materials with varying parameters. I will also look at the influence of the polymer thickness and the sensitivity at a certain distance from the FBG sensor.

Chapter 5

Fabrication and characterization of an FBG sensor

5.1 Outline and objectives

In section 5.2, four different types of highly birefringent fibers will be described and their properties such as birefringence (material, waveguide and modal) will be discussed. Some fibers already had fiber Bragg gratings inscribed, while in two types of fibers, they had to be inscribed during this work. The fabrication and evaluation of these gratings is discussed in section 5.3.1.
The sensitivity of the fabricated FBG sensors are characterized via FEM analyses and experiments. The goal of these sensors is to use them for multi-axial strain field sensing. This implies that the sensitivity of the gratings for different types of strain needs to be known. As was discussed in section 4.1.2, this sensitivity can be determined by applying pure axial stress and a pure transverse line load to the fiber. However, as the characteristics of a grating also depend on temperature, the sensitivity to temperature has to be determined, in order to know how important it is to control temperature during strain measurements.
The sensitivity of a sensor can be determined by (linear) fitting the response of the Bragg peak wavelength λ_{fast} and λ_{slow} and the Bragg peak separation $\Delta\lambda$, resulting in a value with unit pm/°C , pm/$\mu\varepsilon$, ... The goal is to have a high sensitivity of the Bragg peak separation $\Delta\lambda$ for transverse line loading, while $\Delta\lambda$ is more or less constant for temperature and axial strain. A sensor with these specifications can be used for differential, temperature insensitive strain monitoring.

5.2 Fibers under test

In section 3.3 the different possibilities to obtain a highly birefringent fiber were discussed. Four different types of HiBi fiber will be tested, three types of PCF (Type 1, 2 and 3) with

a highly asymmetric microstructure and a bow-tie fiber in which birefringence is induced by thermal stress.
I will explain the important differences between the tested fibers in the following sections. It is important to understand the types of birefringence present in a fiber as the eventual sensitivity of an FBG sensor fabricated in the fiber will be highly dependent on the level of $B_{material}$ and $B_{waveguide}$. $B_{material}$ and B_{modal}=$B_{material}$+$B_{waveguide}$ can be simulated with FEM analyses and more details about these simulation procedures can be found in Appendix A.

5.2.1 Bow-tie fiber

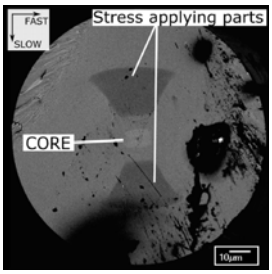

Figure 5.1: SEM image of a bow-tie fiber.

A bow-tie fiber (Fig. 5.1) is birefringent because of the presence of stress-applying parts (SAP) that have a different thermal expansion coefficient than the silica cladding. During fabrication of the fiber thermal stresses will be induced due to the different thermal expansion coefficients, resulting in stress-induced birefringence.
Since a bow-tie fiber is birefringent mainly because of thermal stresses, B_{modal} will be determined mostly by B_{material}. With FEM analyses, both B_{material} and B_{modal} are simulated. The simulation parameters are given in Table 5.1 and the geometrical model used for the simulation is shown in Fig. 5.2(a).

Table 5.1: Geometrical and material parameters for the simulation of a fabricated bow-tie fiber with stress-optic coefficients C_1 = -6.9E-13 m^2/N and C_2 = -41.9E-13 m^2/N. [32]

	Core	Cladding	SAP
n	1.4558	1.4478	1.4418
E (GPa)	69.5	78	78
ν	0.165	0.186	0.186
α (1/K)	2.215E-6	0.54E-6	1.45E-6
T_{ref} (°C)	1030	1100	1100

The fabrication induced birefringence B_{material}=n_2-n_1=(C_1-C_2)(σ_2-σ_1) (with 1 and 2 along

the fast and slow axis respectively) in a bow-tie fiber is shown in Fig. 5.2(b) and a close-up of the core is shown in Fig. 5.2(c). The simulated B_{material} for a bow-tie fiber is about 3×10^{-4} in the core and it is clear from these plots that this birefringence is caused by an asymmetric distribution of the stresses σ_1 and σ_2 in and around the core. In Table 5.2 an overview is given for the average stresses in the circular core.

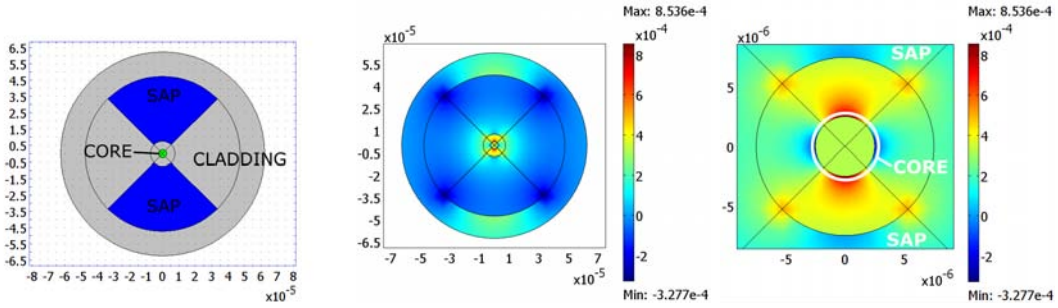

(a) (b) (c)

Figure 5.2: Simulation of a bow-tie fiber: (a) Geometrical model. (b) Material birefringence B_{material} = n_2-n_1 and close-up of the core region (c).

Table 5.2: Simulation of a bow-tie fiber: Numerical results of the fabrication induced stesses in a bow-tie fiber. Values are obtained by averaging over the circular core.

σ_1 (MPa)	14.23
σ_2 (MPa)	106.40
σ_2-σ_1 (MPa)	92.18
B_{material}	3×10^{-4}

The mode profiles of the two fundamental modes with refractive indices n_{fast} and n_{slow} are shown in Fig. 5.3(a) and (b). The obtained values are $n_{\text{fast}} = 1.4489$ and $n_{\text{slow}} = 1.4492$, and the corresponding modal birefringence B_{modal}=n_{slow}-n_{fast} is about 3×10^{-4}.
By comparing B_{material} and B_{modal}, the waveguide birefringence $B_{\text{waveguide}}$=B_{modal}-B_{material} can be found. From the simulated results it is immediately clear that $B_{\text{waveguide}}$ is (nearly) zero for bow-tie fibers and that it is birefringent mostly because of thermal induced stresses.

5.2.2 HiBi PCFs

The most common way to make a PCF birefringent is by making the microstructure of the cladding asymmetric or by making the solid core itself asymmetric, and thus introduce waveguide birefringence. There are numerous ways to design an asymmetric microstructure

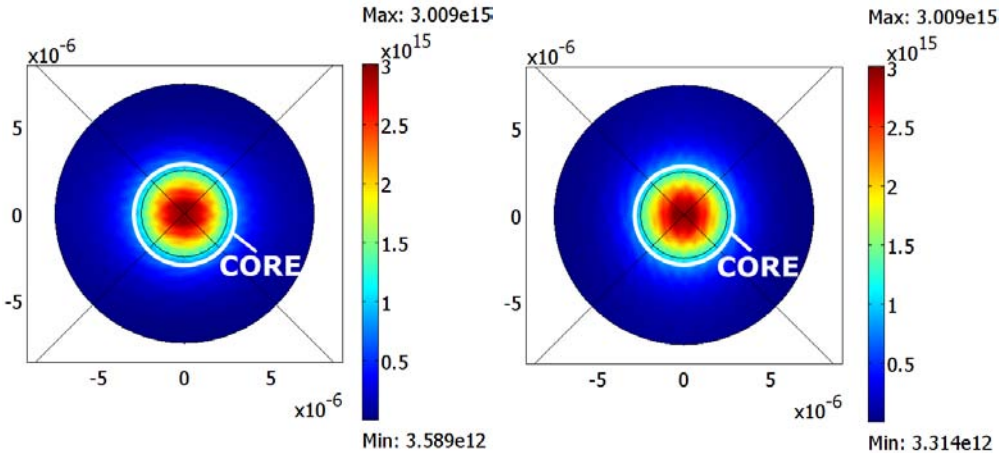

(a) (b)

Figure 5.3: Modal profile of the fundamental modes with refractive indices n_{fast} (a) and n_{slow} (b) guided in the core of a bow-tie fiber.

and an asymmetric core is often the result of deformations caused by fabrication as was explained in section 3.2.2.
Three different types of HiBi PCF are tested and the SEM images of their cross section are shown in Fig. 5.4. Type 1 is an example of a PCF with only a few holes and they are placed in a very asymmetrical way around the core. Type 2 and Type 3 are HiBi PCFs that are specially designed to have a high transverse mechanical sensitivity. Both types are based on a triangular lattice microstructure with some holes enlarged or missing.

Type 1 PCF (Fig. 5.4(a) and (b)) is designed by VUB and WRUT (Wroclaw University of Technology, Poland) and has a birefringence B_{modal} of about 2×10^{-3} according to [33].

Type 2 PCF is designed by WRUT and is meant to have a high mechanical sensitivity. As can be seen from the SEM image in Fig. 5.4(c) and (d), due to the highly asymmetric microstructure the core itself has become asymmetric and this will contribute to the total birefringence B_{modal} of the PCF. The core itself is not only asymmetric, it is also weakly enclosed by airholes along the slow axis resulting in a low air-filling fraction d/Λ (section 3.2.1). This implies that higher order modes will escape the core very easily along this direction, ensuring single mode behaviour but also (possible) high bending losses. A particular feature of PCF Type 2 is that it has a hexagonal outercladding, what could simplify orientation of the fiber in applications where orientation is important. Fabrication of a PCF with hexagonal outercladding is not much more difficult than a PCF with circular outercladding, as the preform can be made by stacking rods and tubes in a hexagonal pattern.

Type 3 PCF is designed by VUB and is, as Type 2, designed to have a high transverse

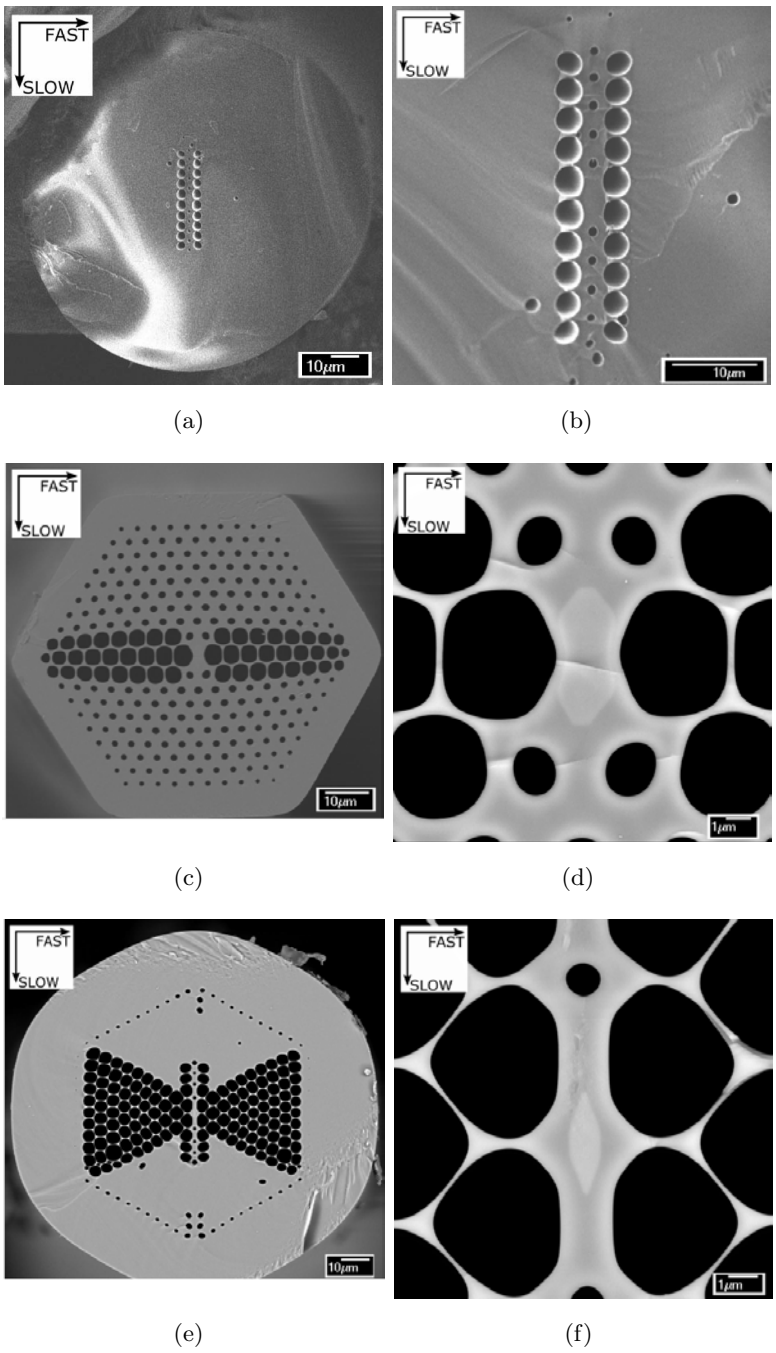

Figure 5.4: SEM images of the cross section of the different types of tested HiBi PCFs: (a) - (b): Type 1, (c) - (d): Type 2, (e) - (f): Type 3, with a cladding diameter of respectively 125 μm, 80 μm and 129 μm.

mechanical sensitivity. This is again achieved by making the microstructure highly asymmetric which also resulted in an asymmetric shaped core (Fig. 5.4(a) and 5.4(b)). The guided modes in this type of PCF are better confined by airholes (large d/Λ), resulting in low bending losses. However, the tight confinement also indicates that higher order modes can be trapped in the core region and the design has to be tuned such that only the fundamental modes are guided in the core. This implies that fabrication has to be well controlled as the slightest deviation from the design can cause the fiber to become multimode.
From the SEM images it is also clear that maintaining exact circular airholes or a circular outercladding, becomes increasingly difficult for more complex microstructures. The outer diameter of this type of fiber is about 125 μm.

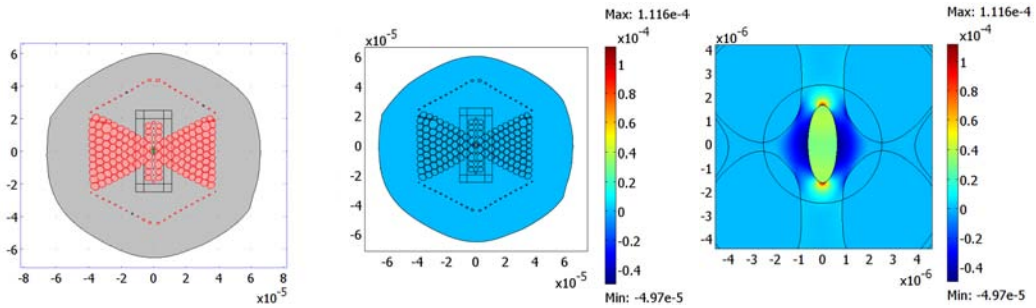

(a) (b) (c)

Figure 5.5: Simulation of a Type 3 PCF: (a) Geometrical model. (b) Material birefringence $B_{\text{material}} = n_2 - n_1$ and close-up of the core region (c).

A FEM analysis was performed on the cross section of a Type 3 PCF to determine the fabrication induced stresses. The geometrical model is shown in Fig. 5.5(a) and the material parameters are listed in Table 5.3. The material birefringence of the bare fiber without any external forces applied, is plotted in Fig. 5.5(b) with a close-up of the core region in Fig. 5.5(c) and Table 5.4 lists the average stresses in the core with $B_{\text{material}} = 3 \times 10^{-5}$.

The mode profiles of the two fundamental modes with refractive indices $n_{\text{fast}} = 1.4168$ and $n_{\text{slow}} = 1.4188$ are shown in Fig. 5.6(a) and 5.6(b). Since the total birefringence $B_{\text{modal}} = 2 \times 10^{-3}$ of the fiber is much larger than B_{material}, this fiber will be mainly birefringent because of the specific microstructure and asymmetrically shaped core. This will be translated in a low temperature sensitivity as will be shown in section 5.4.1.
In Fig. 5.6(c) and 5.6(d) the logarithmic energy distribution of the fundamental modes are shown and from these plots it is immediately clear that the energy of the fundamental modes is distributed asymmetrically, which corresponds to the high level of waveguide birefringence.

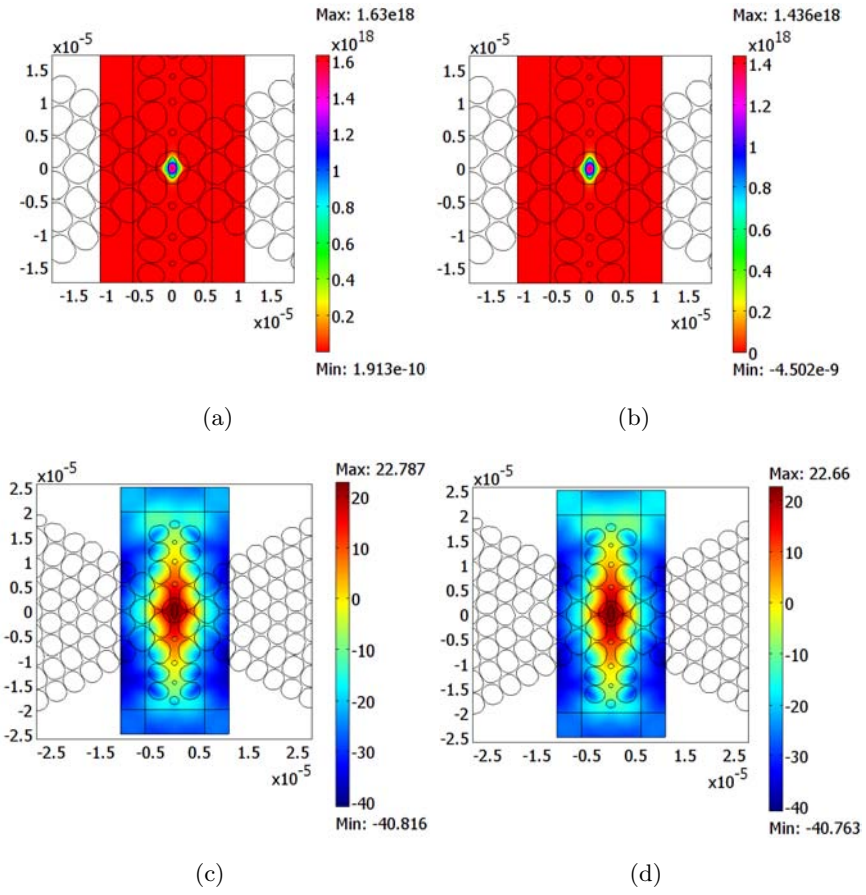

Figure 5.6: Modal profile of the fundamental modes guided in the elliptical core of a Type 3 PCF with refractive index (a) n_{fast} and (b) n_{slow}, and the logarithmic energy distribution plots for both fundamental modes with refractive index (c) n_{fast} and (d) n_{slow}.

	Core	Cladding
radius (μm)	∼0.6-1.7	∼64.5
n	1.4481	1.4440
E (GPa)	73.31	75.11
ν	0.1626	0.165
α (1/K)	8.81E-7	5.31E-7
T (°C)	1070	1100

Table 5.3: Geometrical and material parameters for the simulation of a fabricated Type 3 PCF, with C_1 = 6.9E-13 1/Pa and C_2 = 41.9E-13 1/Pa. [34]

Table 5.4: Numerical results of a FEM analysis of the fabrication induced stresses in a Type 3 PCF. Values are obtained by averaging over the elliptical core region.

σ_1 (MPa)	3.14
σ_2 (MPa)	12.88
σ_2-σ_1 (MPa)	9.74
$B_{material}$	3×10^{-5}

5.3 Fabrication and evaluation of fiber Bragg gratings

5.3.1 Fiber Bragg grating inscription

Grating inscription in PCF Type 2 and Type 3 was performed at the cleanroom facilities of the Univeristy of Mons, where they have a scanned phase mask interferometric setup for the inscription of Type I gratings (Fig. 5.7).

The PCFs were first prepared by splicing both ends to single mode fiber to seal off the airholes of the PCF and prevent outgassing of hydrogen after hydrogenation. The samples were hydrogenated for 48 hours, at a temperature of 200°C and pressure of 200 atm. Afterwards, the samples were stored for a week in a fridge at -40°C. Storing the samples at low temperatures is only necessary when the gratings cannot be inscribed immediately after hydrogenation as low temperatures 'freeze' the effects of hydrogenation.

Once the samples were prepared they could be placed in the interferometric setup (Fig. 5.7 and Fig. 5.8). The sample was spliced to a connector cable, such that the growth of a grating could be monitored with an optical spectrum analyzer (OSA). As the OSA had no built-in source, an external amplified spontaneous emission (ASE) source and directional coupler were used. The fiber was placed behind the phase mask (Λ_{PM}=1095.08 nm) and was clamped in two fiber holders, such that the fiber was tightly fixed.

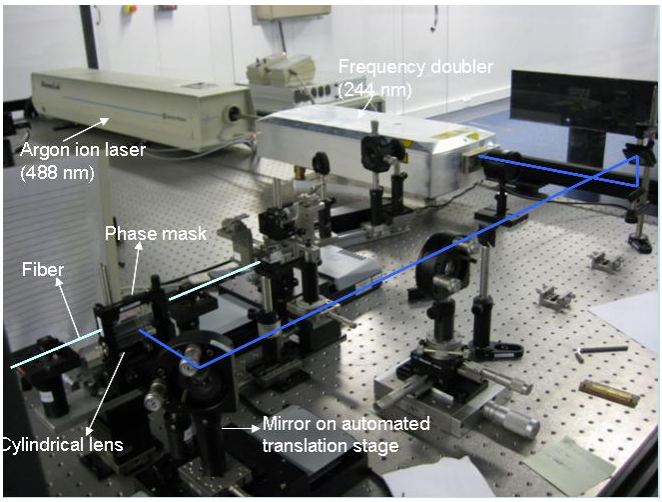

Figure 5.7: Scanning phase mask interferometric setup at University of Mons.

A frequency doubled Argon ion laser was used as UV source (244 nm) and the power of the UV beam could be measured at the exit of the frequency doubler by placing a power meter directly in the path of the beam.

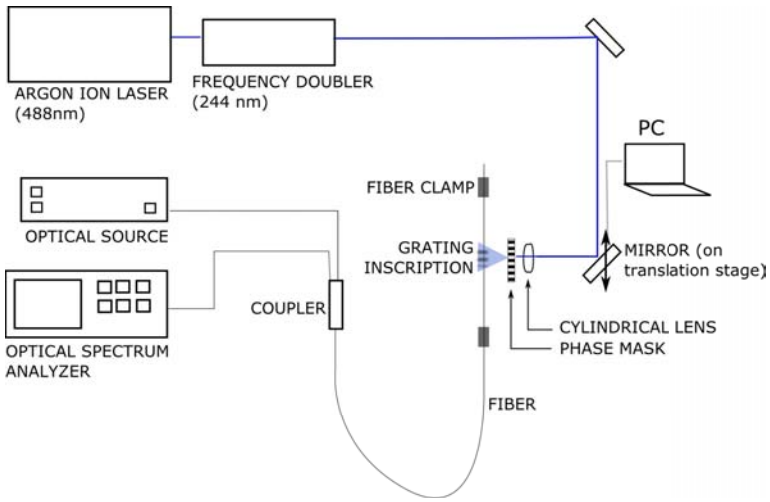

Figure 5.8: Scheme of scanning phase mask interferometric setup at University of Mons.

Actual grating inscription was done when the UV beam hit the fiber. By translating the UV beam over the length of the fiber during inscription, the length and thus reflectivity of the grating could be increased.
There were in total 4 gratings inscribed in Type 2 PCFs, and 7 gratings in Type 3 PCFs. The inscription power was different per sample, varying between 18 mW and 52.7 mW, and the final length of the inscribed gratings varied between 5 mm and 8 mm, depending on the inscription power. These values correspond to those for grating inscription in standard single

mode fibers.
After grating inscription the samples were annealed to remove the remaining hydrogen. This was done by storing the samples for 16h at a temperature of 80°C.

Examples of the resulting spectra of the gratings can be seen in Fig. 5.11 (Type 2 PCF) and Fig. 5.12 (Type 3 PCF).

5.3.2 Evaluation of the inscribed FBGs

The provided bow-tie fibers already had uniform FBGs inscribed in them. This was done with a Talbot interferometric setup with the period of the grating Λ_{FBG}=530 nm and one of the spectra is shown in Fig. 5.9.

The modal birefringence $B_{\mathrm{modal,exp}}=\Delta\lambda/(2\Lambda_{\mathrm{FBG}})$ of the fiber can be calculated from the reflected Bragg peak wavelengths λ_{fast} and λ_{slow} with $\Delta\lambda=\lambda_{\mathrm{slow}}$- λ_{fast}=0.380 nm, and is about 4×10^{-4} for this type of HiBi fiber. This value is comparable with the simulated value $B_{\mathrm{modal,sim}}= 3 \times 10^{-4}$ found in section 5.2.1. There is a strong peak overlap as the peak separation is rather small compared to the spectral width of the peaks and this could make peak determination more difficult.

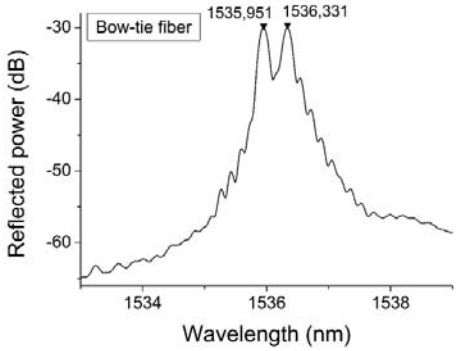

Figure 5.9: Reflection spectrum of an FBG inscribed in a bow-tie fiber. The Bragg peaks wavelengths are λ_{fast} = 1535.951 nm and λ_{slow} = 1536.331 nm.

The provided Type 1 PCFs had also gratings inscribed in them already. This grating inscription was done using a Talbot interferometric setup which made it possible to inscribe an array of gratings with varying period Λ_{FBG}, and Bragg wavelength λ_{B}, by rotating the beam combining mirrors (section 3.1.2). The spectrum of a sample with an array of 7 gratings inscribed, is shown in Fig. 5.10 together with the Bragg wavelengths for grating Gr1.
The birefringence $B_{\mathrm{modal,exp}}$ of this type of fiber is about 2×10^{-3} which corresponds to the value reported by [33]. The modal birefringence of a Type 1 PCF is much larger than that of a bow-tie fiber, which results in a larger peak separation and simplified detection of both

peaks.

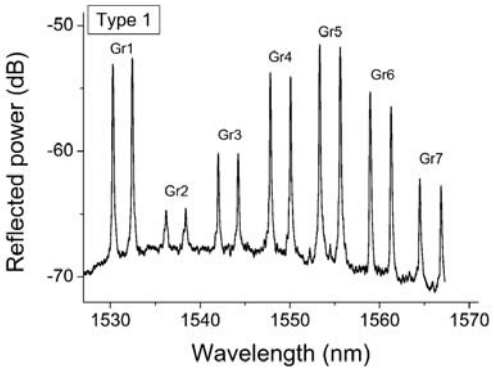

Figure 5.10: Reflection spectrum of a wavelength multiplexed array of 7 FBGs inscribed in a Type 1 PCF. The Bragg peaks wavelengths for grating Gr1 with $\Lambda_{\mathrm{FBG}} = 530$ nm are $\lambda_{\mathrm{fast}} = 1530.278$ nm and $\lambda_{\mathrm{slow}} = 1532.443$ nm.

Gratings are inscribed in a Type 2 PCF with the scanning phase mask technique ($\Lambda_{\mathrm{FBG}} = 547.54$ nm) as described in detail in section 5.3.1. The spectrum of a fabricated sample is shown in Fig. 5.11 together with the Bragg peak wavelengths. This type of PCF has a modal birefringence $B_{\mathrm{modal,exp}}$ of about 1×10^{-3}, which is slightly smaller than for a Type 1 PCF but still large enough for reliable peak detection.

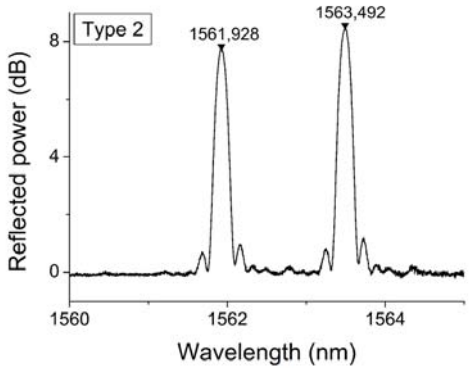

Figure 5.11: Reflection spectrum of an FBG inscribed in a Type 2 PCF. The Bragg peaks wavelengths are $\lambda_{\mathrm{fast}} = 1561.928$ nm and $\lambda_{\mathrm{slow}} = 1563.492$ nm.

Gratings also had to be inscribed in Type 3 PCFs, and this was done with the scanned phase mask technique ($\Lambda_{\mathrm{FBG}} = 547.54$ nm) discussed in section 5.3.1. A spectrum of one of the samples is shown in Fig. 5.12 together with the corresponding Bragg peak wavelengths. The modal birefringence $\mathrm{B}_{modal,exp}$ of this type of fiber is about 2×10^{-3} and is the same as $B_{\mathrm{modal,sim}}$ that was simulated in section 5.2.2.

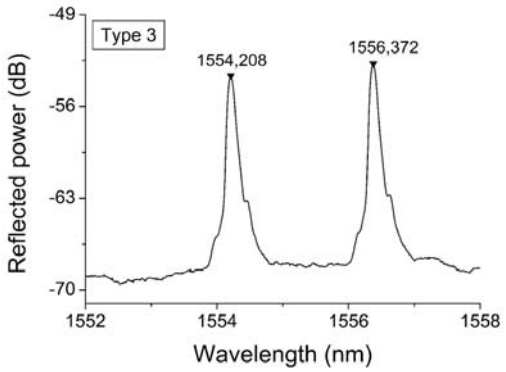

Figure 5.12: Reflection spectrum of an FBG inscribed in a Type 3 PCF. The Bragg peaks wavelengths are $\lambda_{\text{fast}} = 1554.208$ nm and $\lambda_{\text{slow}} = 1556.372$ nm.

5.4 FBG sensor calibration

5.4.1 Temperature calibration

A first step in characterizing the sensitivity of the fabricated fiber Bragg grating sensors, is determining their sensitivity to temperature since we want a temperature insensitive sensor. In section 4.1.1 the theoretical aspects of the temperature sensitvity of an FBG sensor were explained. There are two dominant temperature effects: the thermal expansion (α_f) of a fiber and the thermo-optic effect (α_n).

In this work, the temperature sensitivity of a Type 3 PCF is determined via experiments and the results are compared with earlier reported values for a bow-tie fiber and a Type 1 PCF. The tested Type 3 PCF had an array of four gratings inscribed and in this way the temperature test was actually performed four times.

The experimental setup is shown in Fig. 5.13. The fiber is connected via a directional coupler to an amplified spontaneous emission (ASE) source and an optical spectrum analyzer (OSA) that has a peak detection accuracy of 10 pm. The unstrained grating is placed in an oven of which the temperature can be controlled manually. Although the oven has a built-in read-out, a thermocouple with a more accurate read-out (accuracy of 1 °C) is fixed beside the gratings to determine the temperature.

Once the temperature in the oven is stabilized the Bragg wavelengths are determined. The measured temperature range is from 38.4°C to 86.4°C and the corresponding change in Bragg peak wavelengths (λ_{fast} and λ_{slow}) and Bragg peak separation $\Delta\lambda$ of the second grating (Gr2) are shown in Fig. 5.14(a) and 5.14(b).

The sensitivity (in pm/°C) is found by a linear fit of these graphs (Table 5.5). From Fig. 5.14(b) it is clear that a linear fit of the change in Bragg peak separation is of very little

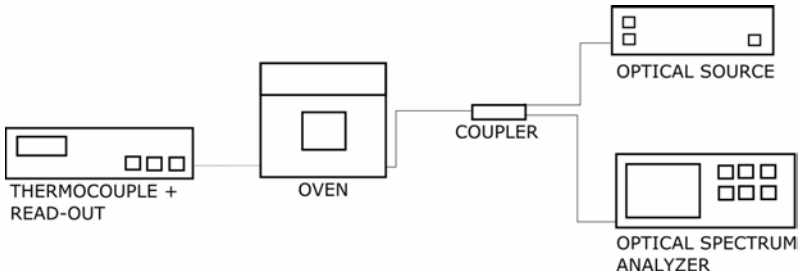

Figure 5.13: Setup to measure the temperature sensitivity of an FBG sensor.

relevance, and this was also the case for the other gratings.
There is some spread on the sensitivities of the Bragg wavelengths of the different gratings. However, the relative standard deviation is 0.02 % for both the fast axis and slow axis, which indicates that the obtained averaged results are reliable. The temperature sensitivity of the Bragg peaks in a Type 3 PCF is thus about 9.09 pm/°C and 9.02 pm/°C for the modes polarized along respectively the fast and slow axis, and the peak separation is insensitive to temperature.

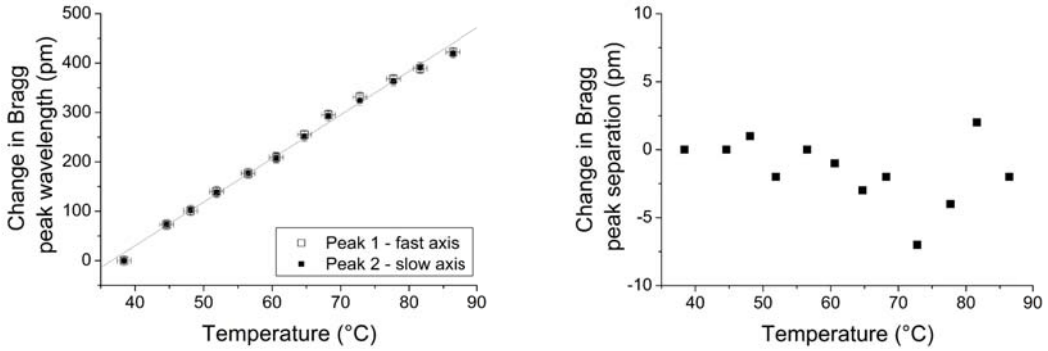

(a) (b)

Figure 5.14: Temperature sensitivity of the second grating of an array of four inscribed in a Type 3 PCF. Nominal shift of (a) the Bragg peak wavelengths and (b) the Bragg peak separation. The line in (a) is a linear fit with a sensitivity given in Table 5.5.

The obtained sensitivity of the Bragg peaks is lower than the theoretical sensitivity of an FBG in a standard (silica) single mode fiber that was calculated in section 4.1.1. This because of the smaller doped regions that result in a lower thermo-optic effect. This was also shown in section 5.2.2 where the thermal stresses were calculated with a FEM analysis.

In Table 5.6 the temperature sensitivity of a Type 3 PCF is compared with that of earlier reported values for a bow-tie fiber and Type 1 PCF. A Type 3 PCF has the lowest sensitivity

Table 5.5: Temperature sensitivity of the array of FBG sensors inscribed in a Type 3 PCF.

[pm/°C]	Gr1	Gr2	Gr3	Gr4	Average	Standard deviation
peak 1 - fast axis	9.15	8.83	9.09	9.26	9.09	0.18
peak 2 - slow axis	9.07	8.78	9.02	9.20	9.02	0.18
peak separation	-0.08	-0.06	-0.08	-0.06	-0.07	0.01

of the Bragg peaks, and also its peak separation is least affected by temperature changes. The bow-tie fiber has the highest temperature sensitivity of $\Delta\lambda$ and this is a direct result of the large amount of thermal stresses present in a bow-tie fiber.

Table 5.6: Temperature sensitivity of FBG sensors fabricated in different types of HiBi fibers.

[pm/°C]	Bow Tie [22]	Type 1 [35]	Type 2	Type 3
peak 1 - fast axis	10.55	10.27	/	9.09
peak 2 - slow axis	10.18	10.15	/	9.02
peak separation	-0.37	-0.12	/	-0.07

5.4.2 Axial strain calibration

The goal is to use FBG sensors fabricated in a HiBi PCF for multi-axial strain sensing. In order to know the potential of the sensors, they have to be calibrated for different types of strain. Pure axial strain is one of them. In section 4.1.2 the theory of the axial sensitvity of an FBG was explained: the sensitivity of the Bragg wavelengths and the Bragg peak separation to pure axial stress is given by the equations (5.1), with p_{11} and p_{12} the strain-optic coefficients and $n_{\text{eff},1}$ and $n_{\text{eff},2}$ the refractive indices along the principal axis.

$$\frac{\delta\lambda_{\text{B},1}}{\lambda_{\text{B},1}} = \varepsilon - \frac{1}{2}n_{\text{eff},1}^2\left[\nu\varepsilon\left(p_{11}+p_{12}\right)+p_{12}\varepsilon\right] \tag{5.1a}$$

$$\frac{\delta\lambda_{\text{B},2}}{\lambda_{\text{B},2}} = \varepsilon - \frac{1}{2}n_{\text{eff},2}^2\left[\nu\varepsilon\left(p_{11}+p_{12}\right)+p_{12}\varepsilon\right] \tag{5.1b}$$

$$\frac{\delta\lambda_{\text{B},2}}{\lambda_{\text{B},2}} - \frac{\delta\lambda_{\text{B},1}}{\lambda_{\text{B},1}} = -\frac{1}{2}\left[\nu\varepsilon\left(p_{11}+p_{12}\right)+p_{12}\varepsilon\right]\left(n_{\text{eff},2}^2 - n_{\text{eff},1}^2\right) \tag{5.1c}$$

The sensitivity to axial strain can be determined by elongating the fiber and grating, and monitoring the corresponding change in Bragg peak wavelengths and Bragg peak separation. By linear fitting this change, a sensitivity in pm/$\mu\varepsilon$ is obtained.
Although axial strain experiments are not performed in this work, for completeness earlier reported values are listed in Table 5.7. In Fig. 5.15 the nominal shift of the Bragg peak wavelength and Bragg peak separation for a type 3 PCF are shown.

Table 5.7: Axial strain sensitivity of FBG sensors fabricated in different types of HiBi fibers.

[pm/$\mu\epsilon$]	Bow Tie [22]	Type 1	Type 2 [35]	Type 3 [35]
peak 1 - fast axis	1.22	/	1.14	1.18
peak 2 - slow axis	1.23	/	1.14	1.18
peak separation	0.01	/	0.00	0.00

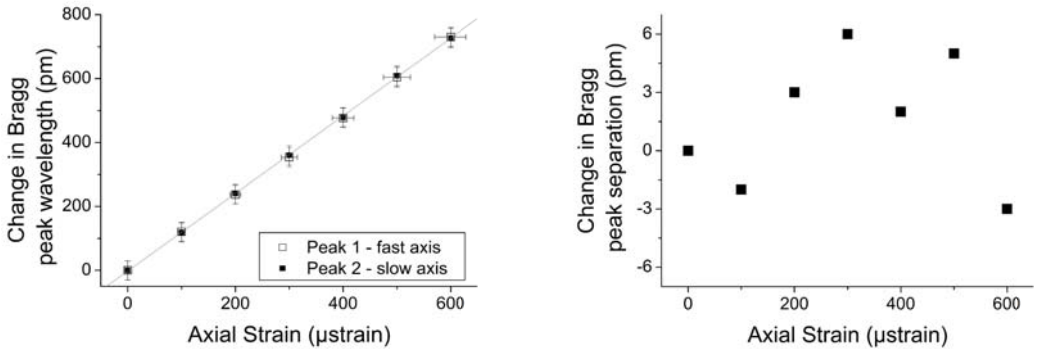

(a) (b)

Figure 5.15: Pure axial strain sensitivity of an FBG inscribed in a Type 3 PCF. Nominal shift of (a) the Bragg peak wavelengths and (b) the Bragg peak separation. The line in (a) is a linear fit with a sensitivity given in Table 5.7. [35]

From Table 5.7 it is clear that for all three types of HiBi fiber λ_{fast} and λ_{slow} have about the same sensitivity for axial strain. The Bragg peaks have a sensitivity of about 1.2 pm/$\mu\varepsilon$ and the peak separation is insensitve to axial strain. According to equation 5.1c this implies that for these HiBi fibers $n_{\text{eff},1} \simeq n_{\text{eff},2}$.

5.4.3 Hydrostatic pressure calibration

Although the specific case of sensitivity to hydrostatic pressure was not discussed in section 4.1.2, it is a very good indication for the transverse line load sensitivity. Moreover, there are also certain applications were a sensor for hydrostatic pressure can be interesting, for example to monitor pressure in oil wells or pipelines.

The hydrostatic pressure sensitivity of and FBG sensor fabricated in a bow-tie fiber and a Type 3 PCF is determined via 2D FEM analyses (the details regarding the numerical simulation procedure can be found in Appendix A). The geometrical model and material parameters of section 5.2 are used and the simulated pressure range is from 0 - 200 bar. The corresponding change in refractive index n_{fast} and n_{slow} of the two fundamental modes is monitored and their change corresponds to the sensitivity of the modal birefringence to hydrostatic pressure. By applying the Bragg condition $\lambda_{\text{B}} = 2n\Lambda$ and assuming an FBG period $\Lambda_{\text{FBG}} = 530$ nm, a sensitivity for hydrostatic pressure (in pm/bar) of the Bragg wavelengths can be calculated. The results for a bow-tie fiber and a Type 3 PCF are listed in Table 5.8 and in Fig. 5.16(a) and 5.16(b) the response of the Bragg peaks and peak separation of an FBG sensor fabricated in a Type 3 PCF are shown.

Table 5.8: Hydrostatic pressure sensitivity of FBG sensors fabricated in different types of HiBi fibers. Experimental values are reported in [35].

[pm/bar]	Bow Tie		Type 1		Type 2		Type 3	
	2D Sim	Exp	2D Sim	Exp	2D Sim	Exp	2D Sim	Exp
peak 1 - fast axis	0.64	-0.27	/	-0.44	/	0.94	2.25	0.99
peak 2 - slow axis	0.72	-0.21	/	-0.49	/	-0.22	0.78	-0.48
peak separation	0.08	0.06	/	-0.05	/	-1.16	-1.47	-1.47

The results from the simulation in Table 5.8 show that there is a distinct difference in the sensitivity for a bow-tie fiber and for a Type 3 PCF. The sensitivity of the mode polarized along the slow axis is more or less the same for both fibers ($\sim$ 0.75 pm/bar), but the mode polarized along the fast axis behave in a very different way. For the FBG sensor fabricated in a bow-tie fiber, the sensitivity of the mode polarized along the slow axis is the highest which results in the Bragg peaks moving away from each other when the hydrostatic pressure is increased, and this with 0.08 pm/bar. On the other hand, for a Type 3 PCF the

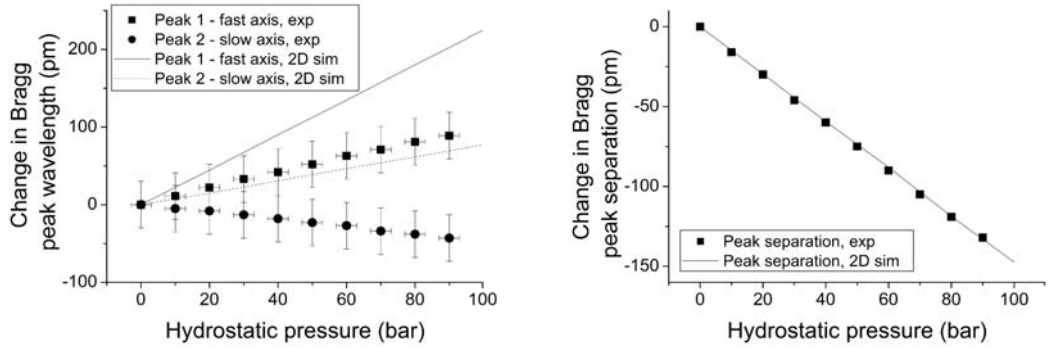

(a) (b)

Figure 5.16: Hydrostatic pressure sensitivity of an FBG inscribed in a Type 3 PCF. Nominal shift of (a) the Bragg peak wavelengths and (b) the Bragg peak separation, obtained via simulations (lines) and experiments (patterns) reported in [35].

mode polarized along the fast axis is the most sensitive, resulting in a decrease of $\Delta\lambda$ when hydrostatic pressure increases. Moreover, the sensitivity of the peak separation is much larger for a Type 3 PCF than for a bow-tie fiber, which should result in a higher transverse line load sensitvity. Whether this is indeed the case will be investigated in section 5.4.4.

The hydrostatic pressure sensitivity for FBG sensors fabricated in different types of HiBi fibers were experimentally determined in [35] and the results are summarized in Table 5.8. The sensors created in a Type 2 and Type 3 PCF both have a very high pressure sensitivity for the Bragg peak wavelengths and the Type 3 PCF has the highest sensitivity for the Bragg peak separation. The corresponding plots of the Bragg peak behaviour of the Type 3 PCF are shown in Fig. 5.16.
In [35] it was also shown that the pressure sensitivity of a Type 2 and Type 3 PCF is independent of temperature and this was done by performing the hydrostatic pressure test at different temperatures. This implies that the transverse strain sensitivity of these fibers will likely be independent of temperature.

If the simulated results are compared with the experimental results, one can see that while the sensitivity of the Bragg peaks are very different, the sensitivity of the Bragg peak separation is nearly (bow-tie fiber) or exactly (PCF Type 3) the same.
This could be the result from axial strain that is not taken into account in the 2D FEM analyses, while it does play a significant role in the experiments. Since axial strain has the same influence on both Bragg peaks, the Bragg peak separation will not be affected by the 2D approximation.
Another reason could be that the stress-optic coefficients C_1 and C_2 chosen for the FEM

analyses do not correspond to the values of the fabricated PCF, but that the difference $C_1 - C_2$ does. This would result in a miscalculation in the sensitivity of the Bragg peaks, but not in the Bragg peak separation.

5.4.4 Transverse line load calibration

A transverse line load calibration is another part of determining the potential of an FBG sensor for multi-axial strain sensing. In section 4.1.2 equations (5.2) were derived for the change in Bragg peak wavelength when a HiBi fiber is transversally loaded, assuming that transverse strain field is dependent on ε_1 and ε_2, and not on ε_3.

$$\frac{\delta\lambda_{\mathrm{B},1}}{\lambda_{\mathrm{B},1}} = -\frac{1}{2}n_{\mathrm{eff},1}^2\left[p_{11}\varepsilon_1 + p_{12}\varepsilon_2\right] \tag{5.2a}$$

$$\frac{\delta\lambda_{\mathrm{B},2}}{\lambda_{\mathrm{B},2}} = -\frac{1}{2}n_{\mathrm{eff},2}^2\left[p_{11}\varepsilon_2 + p_{12}\varepsilon_1\right] \tag{5.2b}$$

A transverse line load can be applied to a fiber by compressing it between two plates (resulting in $\varepsilon_3 = 0$). When the plates and the fiber are brought into contact, the contact can be described by a line force (or point force if only the cross section is considered).
If the elastic moduli of the core and cladding of a fiber are comparable, the stresses in the core (σ_x and σ_y) resulting from the transverse loading, can be approximated by the equations (5.3) used to describe the stresses in a dielectric rod with radius r when an external force f_{y} is applied [36]. From these equations it is clear that a (uniaxial) fiber will become birefringent by applying a transverse external load, as σ_x and σ_y behave different.

$$\sigma_{\mathrm{x}} \cong f_{\mathrm{y}}/\left(\pi r\right) \tag{5.3a}$$

$$\sigma_{\mathrm{y}} \cong -3f_{\mathrm{y}}/\left(\pi r\right) \tag{5.3b}$$

Bow-tie fiber

A 2D simulation is performed to determine the transverse line load sensitivity of a bow-tie fiber with a geometry as shown in Fig. 5.2(a) and simulation parameters as listed in Table 5.1.
A line force of maximum 2 N/mm is applied to the fiber under different angles and for each rotation angle the change in refractive index of the fundamental modes n_{fast} and n_{slow} is monitored. These values can be calculated to Bragg wavelengths by assuming that a uniform grating with $\Lambda_{\mathrm{FBG}} = 530$ nm, and consequently a sensitivity in pm/(N/mm)) is found. In Fig. 5.17 the transverse line load sensitivity of the Bragg peaks and peak separation of a bow-tie fiber is shown when loaded under different angles.

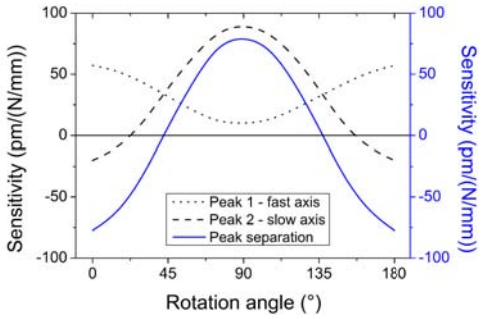

Figure 5.17: Simulated transverse line load sensitivity of an FBG sensor fabricated in a bow-tie fiber with a diameter of 125 μm, when loaded under different rotation angles.

The sensitivity versus rotation angles shows a sine-like trend with a maximum positive sensitivity of the Bragg peak separation of 81.1 pm/(N/mm) when loaded along the fast axis, and a sensitivity of -77.4 pm/(N/mm) when a force is applied along the slow axis.

Type 3 PCF

A 2D FEM analysis is performed to determine the transverse line load sensitivity of an FBG sensor fabricated in a Type 3 PCF for loading under different orientations. This was done by applying a line force of maximum 2 N/mm on the geometry shown in Fig. 5.5(a) with material parameters as listed in Table 5.4. In Fig. 5.18 the result is shown of the simulated transverse line load sensitivity of a Type 3 PCF when loaded under different rotation angles. This graph clearly shows a sine-like trend with high sensitivities of the Bragg peak separation when a force is applied along 90° which is the fast axis (235.3 pm/(N/mm)), or when the fiber is loaded along 0° which corresponds to the slow axis (-324.9 pm/(N/mm)).

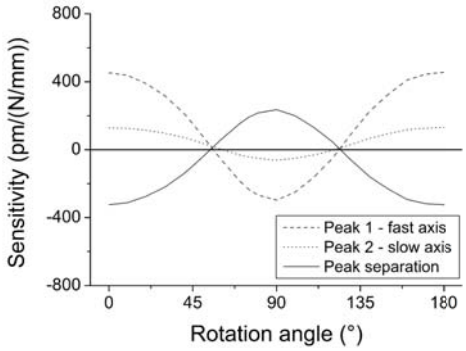

Figure 5.18: Simulated transverse line load sensitivity of an FBG sensor fabricated in a Type 3 PCF when loaded under different rotation angles.

In Fig. 5.19 the material birefringence B_{material} is shown for transverse loading under 0°

and 90°. From these plots it is clear that for loading under 90° the material birefringence increases, while it decreases when a force is applied along 0°.
These colour plots also clearly show that the large side-microstructures 'guide' the applied force along the core, as they were intended to do.

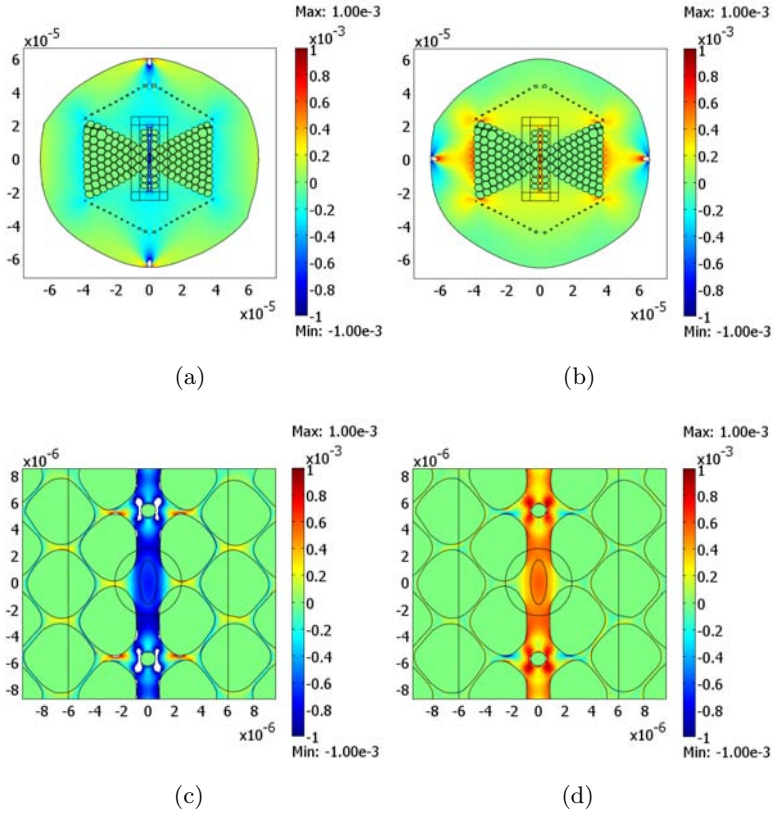

Figure 5.19: Simulated material birefringence B_{material} = n_2-n_1 when a transverse line load of 2N/mm is applied along the slow axis (a and c) or along the fast axis (b and d).

The FEM simulations also showed that the waveguide birefringence $B_{\text{waveguide}}$=B_{modal}-B_{material} of the Type 3 PCF barely changes under transverse loading. It is thus the contribution of the material birefringence to the modal birefringence that will cause the Bragg peak separation to increase or decrease under transverse loading.

The transverse line load sensitivity of a sensor fabricated in a Type 3 PCF is also determined experimentally with the test setup as shown in Fig. 5.20. With this setup, the experiment is performed on two fibers at the same time, and their results are averaged to cancel out inhomogeneous loading. Both fibers are clamped by two rotation stages (accuracy 1°) to determine the transverse strain sensitivity for different fiber orientations.
The gratings are placed on a glass plate with on top a steel plate that transfers a load from a

test bench via a ball-joint to the fibers. The actual applied load is determined by a load cell with an accuracy of 0.25 %.
The fibers are connected via two directional couplers to an unpolarized optical source and a commercial FBG scan (FOS&S FBG-scan 608 interrogator) with a peak detection accuracy of 30 pm and resolution of 1 pm (Fig. 5.21).

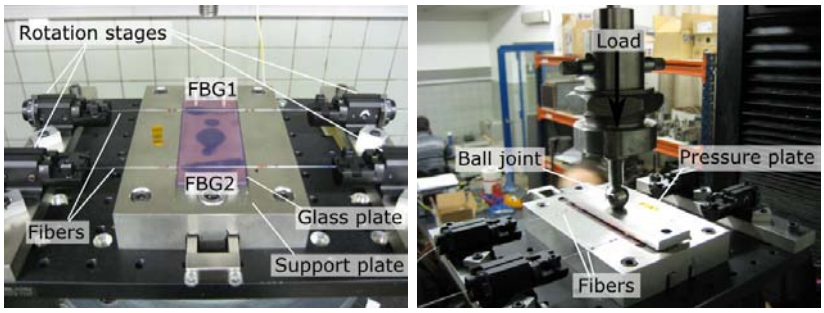

(a) (b)

Figure 5.20: Setup to determine the transverse line load sensitivity of two fibers of the same type, at the same time. (a) shows the two fibers clamped in rotation stages with their FBG sensor positioned on top of the glass plate. (b) shows the mechanical load and ball joint that apply a load to the aluminum plate and the fibers.

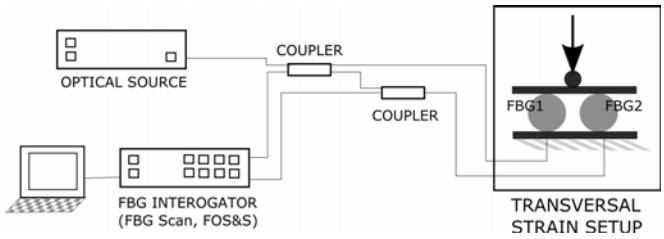

Figure 5.21: Overview of the test setup to determine the transverse line load sensitivity of FBG sensors fabricated in two Type 3 PCFs.

Since the microstructure of the PCF is highly assymmetric, one cannot assume that the resulting strain in the core is the same for both fibers when they are randomly oriented. To improve accuracy, the transverse strain experiment should be performed in two steps: an orientation procedure to rotate both fibers over the same angle, and a calibration procedure to determine the sensitivity of the two fibers (Fig. 5.22).

In the orientation step, a continuous increasing (and decreasing) load of maximum 0.2 N/mm is applied to both fibers for different orientation angles (every 10°) over a total rotation of 180°. This results in two plots, one for each fiber, showing the sensitivity of the Bragg peaks for each rotation angle. The relative mis-orientation of the two fibers can be found by

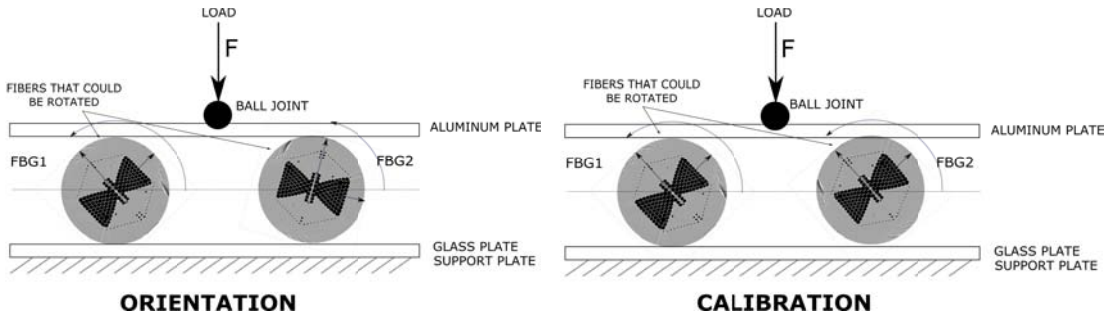

(a) (b)

Figure 5.22: The transverse line loading experiment consists out of two steps: (a) an orientation procedure to orient both fibers in the same way and (b) a calibration step to determing the sensitivity of both fiber under different orientations.

comparing the trends of these graphs. Both fibers are oriented such as to align their trends and by doing so, the same strain will be applied to their cores.

Once both fibers are oriented in the same manner, the calibration step can be performed. The two fibers are again loaded under different angles (every 15° over a total rotation of 360°) and plots are made of the transverse strain sensitivity versus orientation. These plots are shown in Fig. 5.23.

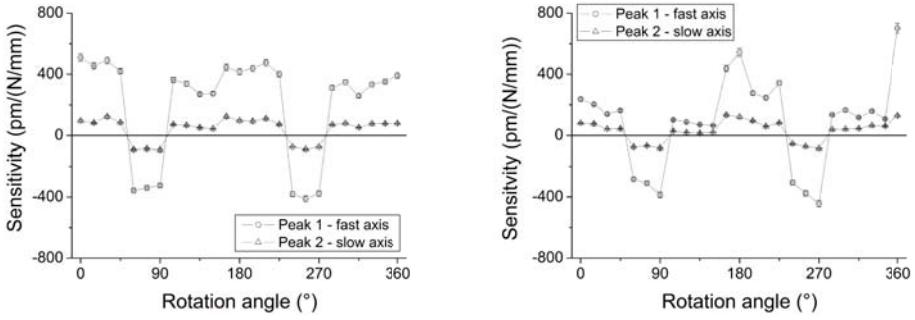

(a) (b)

Figure 5.23: Transverse line load sensitivity of FBG sensors fabricated in two Type 3 PCFs ((a) FBG1 and (b) FBG2) for a load applied under different angles.

To avoid inhomogeneous loading because of non-parallel plates, the results of both fibers are averaged (Fig. 5.24). The resulting average has a maximum sensitivity for the Bragg peak separation when loaded under 180°. By comparing the SEM crosssection of the Type 3 PCF (Fig. 5.4(e)) with the pattern in Fig. 5.24, one can assume that the orientation of 0° or 180°

corresponds to a load applied along the slow axis.

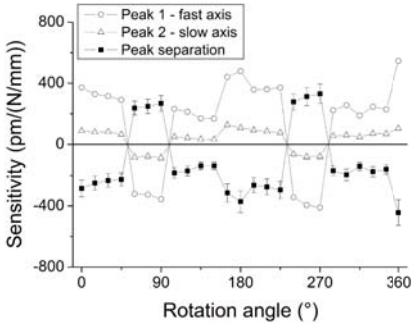

Figure 5.24: Averaged transverse line load sensitivity of a sensor fabricated in a Type 3 PCF.

Fig. 5.24 also shows some 'plateaus' where the sensitivity is constant over a range of angles. These can be the intended result from a specific microstructure, but since this was not the case for the simulated results, it is not likely. It could also be attributed to the flattened outercladding of the PCF structure. Initially, when the pressure plates and the fiber make contact the fiber will stay in the correct orientation, but as soon as some extra load is applied the fiber may rotate and slip onto the flat side. This effect was not taken into account in the simulation, as these was performed with an ideal line force.

In Fig. 5.25 and Table 5.9 the results for the Bragg peak separation from the experiment are compared with those of the simulation. Apart from the plateaus in the experimental results, the values are more or less comparable. This indicates that the simulated line force on the cross section is a relatively good approximation to the actual experiment with pressure plates.

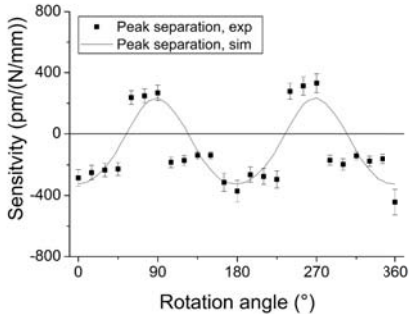

Figure 5.25: Comparison of the transverse line load sensitivity of the Bragg peak separation obtained with experiments (patterns) or simulations (solid line).

Table 5.9: Comparison of simulated and experimental results of the transverse line load sensitivity when a sensor fabricated in a Type 3 PCF is loaded along the fast axis (90°) or the slow axis (0°).

[pm/(N/mm)]	90°		0° or 180°	
	experimental	simulation	experimental	simulation
peak 1 - fast axis	-354.8	-296.8	480.1	456.3
peak 2 - slow axis	-87.0	-61.5	108.5	131.4
peak separation	268.0	235.3	-371.6	-324.9

5.5 Conclusion

Four different types of HiBi fibers were tested: Three different types of PCF that have a highly asymmetric microstructure and a bow-tie fiber that is birefringent because of the presence of thermal stresses. With FEM analyses it was shown that the material birefringence of a bow-fiber is much larger than for a Type 3 PCF (3×10^{-4} versus 3×10^{-5}). The modal birefringence of the bow-tie fiber was also about 3×10^{-4} which indicates that birefringence is due to thermal stresses. For a Type 3 PCF, the modal birefringence is much larger and about 2×10^{-3}. The (temperature insensitive) waveguide birefringence will therefore be the most dominant contribution to the birefringence of a Type 3 PCF.

Fiber Bragg grating inscription in Ge-doped Type 2 and Type 3 PCFs was done using the scanning phase mask technique. The reflection spectra of the FBGs showed that the HiBi PCFs have indeed a much larger peak separation ($\sim$ 2 nm) than a bow-tie fiber ($\sim$ 0.4 nm). If an external influence causes a decrease of the peak separation, correct peak detection can become difficult for a bow-tie fiber as the peaks will strongly overlap resulting in peak deformations.

The FBG sensor calibration started with a themal test performed on an FBG fabricated in a Type 3 PCF. The temperature sensitivity of the modes polarized along the fast and slow axes was about 9.09 pm/°C and 9.02 pm/°C, respectively. The peak separation was nearly insensitive to temperature variations, which indicates that a Type 3 PCF could be used as a differential, temperature insensitive sensor.

An axial strain calibration was not performed in this Master thesis, but earlier reported values show that FBGs fabricated in a Type 2 and Type 3 PCF have more or less the same sensitivity to axial strain. The Bragg peaks shift with about 1.2 pm/$\mu\varepsilon$ which is a normal value for silica fibers, and there is no change in Bragg peak separation under influence of axial strain.

Another performed calibration was that for hydrostatic pressure, as this can give a very good indication regarding the transverse line load sensitivity.

FEM simulations showed that the Bragg peaks of a Type 3 PCF shift to longer wavelengths when pressure is applied, while the overall peak separation decreases with -1.47 pm/bar.
In earlier reported results of the experimental calibration of hydrostatic pressure, the exact same sensitivity of the Bragg peak separation was found. This was however not the case for the behaviour of the Bragg peaks themselves. This difference could be the result from axial strains that are not taken into account in the performed 2D FEM analyses. Another possibility is that the used values of the stress-optic coefficients C_1 and C_2 slightly differ from the real values, but that their difference C_1-C_2 does correspond to that of the actual fiber.
According to the earlier reported experimental results, both Type 2 and Type 3 PCF have a high hydrostatic pressure sensitivity, and this sensitivity is independent of temperature. This is a clear indication that both types of fibers will have a high transverse line load sensitivity with a Bragg peak separation that is independent of temperature.

The final calibration test was a transverse line load test. Simulations showed that there is a (sine-like) dependence of sensitivity on the direction along which the load is applied to the fiber. A simulation of a bow-tie fiber resulted in a maximum sensitivivty of the peak separation of 81 pm/(N/mm)), while earlier reports obtained a maximum sensitivity of 160 pm/(N/mm)). This difference is likely due to the geometrical model from the simulation that does not correspond to the bow-tie fiber they tested experimentally. Simulations on a Type 3 PCF showed a maximum transverse line load sensitivity of the peak separation of -325 pm/(N/mm), which is a significant improvement compared to the bow-tie fiber.
An experimental transverse line load calibration was also performed on an FBG sensor fabricated in a Type 3 PCF. The combination of a test setup in which force was applied with two pressure plates and the flattened (hexagonal-like) cladding of the PCF, resulted in 'plateaus' in the sensitivity plots. These are likely to result from the fiber rotating or slipping onto a flat side when load is applied. The maximum sensitivity of the peak separation was -372 pm/(N/mm) which is even higher than the value obtained with simulations.

The overall conclusion from this chapter is that an FBG sensor fabricated in a Type 3 PCF can be used as a differential sensor that is insensitive to temperature and has a very high transverse line load sensitivity.

Chapter 6

Optical fiber sensors embedded in carbon fiber reinforced polymers

6.1 Outline and objectives

In the previous chapter, FBG sensors fabricated in different types of HiBi fibers were calibrated for temperature, axial strain, hydrostatic pressure and transverse line load. This showed that a Type 2 and Type 3 PCF had a very high transverse line load sensitivity, and moreover, this sensitivity is independent of temperature. Since a composite has a very high stiffness, one could assume that transverse loading of a composite will result in transverse loading of the embedded fiber. Type 2 and Type 3 PCFs therefore could make a good candidate for structural health monitoring of fiber reinforced polymers, in which the monitoring of transverse strains is of crucial importance.

In this chapter I will look at the possibilities of embedding a Type 3 PCF in a composite material and embedding this fiber under a certain orientation. The fabrication is evaluated by looking at the reflection spectrum and by a destructive test that is done when all other tests are finished. The first test performed on the fabricated sample is a temperature test to compare the temperature sensitivity of the bare fiber and the embedded fiber.
Both the axial and transverse strain sensitivity of the embedded FBG sensors will be determined via extensive testing. These results will indicate whether the improved transverse line load sensitivity of the bare fiber allows to provide a high transverse strain sensitivity of an FBG sensor embedded in a composite material.

6.2 Fabrication of composite laminates with embedded optical fiber Bragg sensors

6.2.1 Autoclave technique

The composite samples used to test the strain and temperature sensitivity are made from prepreg material and fabricated with an autoclave process. Prepreg is a type of composite material in which the reinforcement fibers are already placed in a partially cured matrix; in this work a uni-directional carbon fiber reinforced epoxy matrix is used (M55j/M18). Epoxy is a thermosetting polymer and will cure ('polymerize') when heated. To prohibit curing of the epoxy matrix, the prepreg is stored in a freezer at -18° before actual fabrication of the laminate. Prepreg comes on a large roll (Fig. 6.1), with reinforcement fibers along the length of the roll. Layers can be cut with different dimensions and orientation of the reinforcement fibers, and a laminate can be formed by stacking these in a particular way.

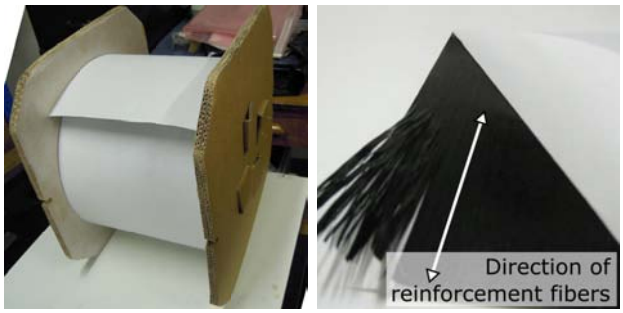

(a) (b)

Figure 6.1: (a) The prepreg material is wrapped on a roll. The layer is covered with a protective film on each side. (b) The orientation of the reinforcement fibers is unidirectional, as is illustrated by tearing the fibers apart (merely done for illustrating purposes).

The laminate can be cured in an autoclave process, which will polymerize the epoxy matrix when the temperature is increased. In Fig. 6.2 the different elements of the autoclave or curing cycle is shown. An autoclave is used to control the pressure to ensure good adhesion between the different layers of the laminate, while a plate with heating elements is used to increase the temperature. The laminate is placed on this heating plate together with several layers of release film to facilitate removal of the sample afterwards and an absorbing layer to remove excessive epoxy. The complete lay-up is put in a vacuum bag to remove air bubbles that can be trapped in between different layers of prepreg. The setup is placed in the autoclave and the curing cycle can start.

The curing cycle will determine the eventual quality and properties of the laminate. It is

(a) (b) (c) (d)

Figure 6.2: (a) Heating plate that goes into the autoclave. (b) Composite sample is placed on the heating plate, inside a vacuum bag. (c) Eveything is placed in the autoclave and undergoes a curing cycle. (d) The end result is a cured composite sample.

therefore important to control the pressure, vacuum and temperature with high precision, as shown in Fig. 6.3.

One layer of prepreg material will have a final layer thickness of 0.1 mm after curing. The relation between induced strains ε and resulting stresses σ is given by equation (6.1) with the coordinate system as depicted in Fig. 6.4. The material properties of a layer after curing are listed in Table 6.1. The material properties of the complete laminate are heavily dependent on the stacking orientations of the reinforcement fibers in the different layers and these properties could be determined by performing a number of tests on the resulting composite samples.

$$\begin{bmatrix} \sigma_{1'1'} \\ \sigma_{2'2'} \\ \sigma_{3'3'} \\ \sigma_{2'3'} \\ \sigma_{3'1'} \\ \sigma_{1'2'} \end{bmatrix} = \begin{bmatrix} \frac{1}{E_{1'}} & \frac{-\nu_{1'2'}}{E_{1'}} & \frac{-\nu_{1'3'}}{E_{1'}} & 0 & 0 & 0 \\ \frac{-\nu_{2'1'}}{E_{2'}} & \frac{1}{E_{2'}} & \frac{-\nu_{2'3'}}{E_{2'}} & 0 & 0 & 0 \\ \frac{-\nu_{3'1'}}{E_{3'}} & \frac{-\nu_{3'2'}}{E_{3'}} & \frac{1}{E_{3'}} & 0 & 0 & 0 \\ 0 & 0 & 0 & \frac{1}{G_{2'3'}} & 0 & 0 \\ 0 & 0 & 0 & 0 & \frac{1}{G_{3'1'}} & 0 \\ 0 & 0 & 0 & 0 & 0 & \frac{1}{G_{1'2'}} \end{bmatrix} \begin{bmatrix} \varepsilon_{11} \\ \varepsilon_{22} \\ \varepsilon_{33} \\ 2\varepsilon_{23} \\ 2\varepsilon_{31} \\ 2\varepsilon_{12} \end{bmatrix} \tag{6.1}$$

Table 6.1: Elastic material properties for the M55J/M18 carbon/epoxy material (after curing). [22]

$E_{1'1'}$ [GPa]	$E_{2'2'}$=$E_{3'3'}$ [GPa]	$G_{1'2'}$=$G_{1'3'}$ [GPa]	$G_{2'3'}$ [GPa]	$\nu_{1'2'}$=$\nu_{1'3'}$ [-]	$\nu_{2'3'}$=$\nu_{3'2'}$ [-]	$\nu_{2'1'}$=$\nu_{3'1'}$ [-]
300.0	6.3	4.3	2.3	0.320	0.380	0.002

6.2.2 Fabrication of laminates with embedded optical fiber sensors

The autoclave technique described above can be used to embed optical fibers sensors in composites. The samples made for this work have a $[0_2, 90_2]_{2S}$ lay-up, forming a so-called

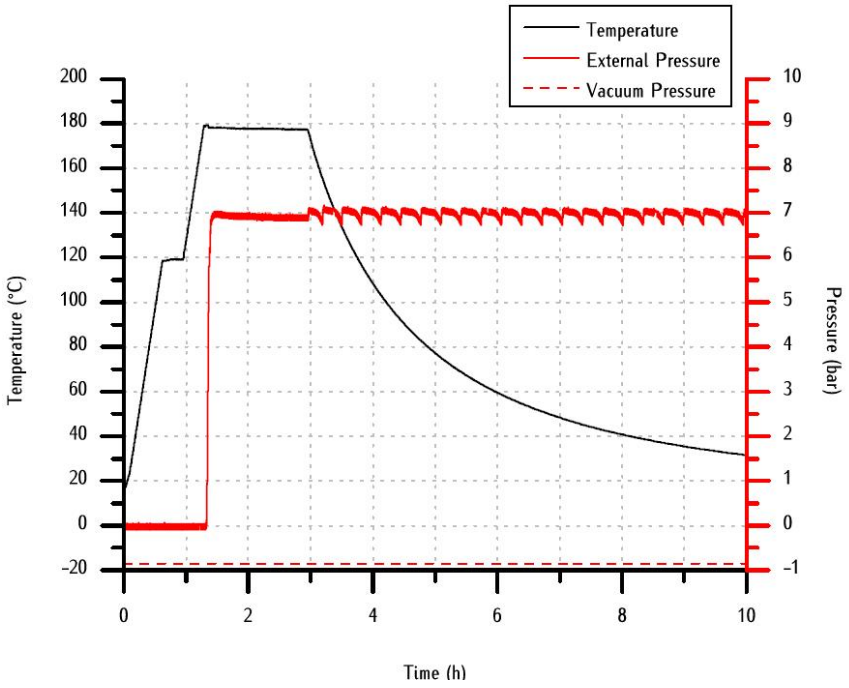

Figure 6.3: The curing cycle used to produce the M55J/M18 carbon/epoxy samples.

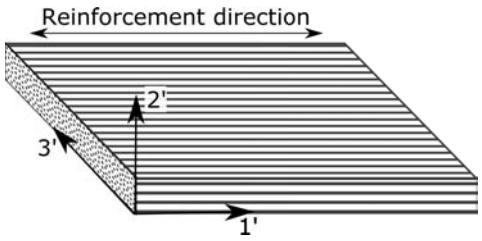

Figure 6.4: The local orthogonal coordinate system used for a single composite layer.

cross-ply laminate. This notation can be understood as: the number 0 and 90 correspond to the angle of reinforcing fibers with the length of the sample (and thus with the optical fiber); the subscript 2 indicates the number of consecutive layers; the subscript 2s denotes a symmetrical (two-fold) lay-up with respect to the mid-plane. This results in a 16-layer laminate with the optical fiber placed in between layers 8 and 9 (Fig. 6.5). As the optical fiber is placed in between layers with the reinforcement fibers oriented in the same direction, a minimal amount of disruption of the composite can be expected.
The strength and stiffness of a cross-ply laminate will be much higher in-plane (along the reinforcement fibers) than perpendicular to the laminate, and such a laminate can thus be considered as an orthotropic material.

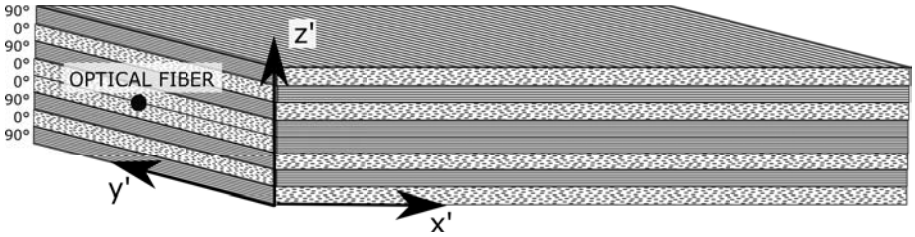

Figure 6.5: Schematic representation of the $[0_2,90_2]_{2s}$ stacking, with an optical fiber embedded in the centre. Also shown is the global orthogonal coordinate system of a fabricated sample. The optical fiber is directed along the x'-axis.

Although the embedding of optical fiber sensors in fiber reinforced polymers has been done plenty of times before, it is still a fragile process. Because of the large difference in stiffness between the flexible, though brittle optical fiber and the very stiff FRP sample, special attention has to go to the point where the optical fiber exits the FRP sample. In the fabricated samples, epoxy tape is placed at the exit to protect the optical fiber as much as possible, but the risk of breaking the optical fiber at this point during manufacturing or testing is remains high.

6.2.3 Orientation control of an embedded optical fiber sensor

A type 3 PCF is embedded in the composite samples, and as the transverse sensitivity of these fibers is highly dependent on the orientation of the fiber, the orientation of the fibers has to be determined and the desired orientation has to be indicated before embedding it.
Two methods were used to determine the orientation of the fiber. As the transverse sensitivity can be determined with the setup discussed in section 5.4.4, the orientation with highest sensitivity can be indicated with small tabs (prepreg or epoxy), as shown in Fig. 6.6(a). Another possibility is to look at the microstructure at both end-facets of the PCF with a microscope (Fig. 6.6(b) and **??**), and align both ends to the most sensitive direction (slow axis).

Both orientation methods have their advantages and disadvantages. The method that uses the transverse line load set-up is time-consuming, but determines the orientation precisely at the position of the grating. Checking the orientation of the PCF with the microscope is a fast method, but optical connections ('pig-tails') have to be removed, and as only the end facets are oriented, mis-orientation at the position of the grating is still possible.
Both methods were used, and the results will be compared in section 6.3.2.

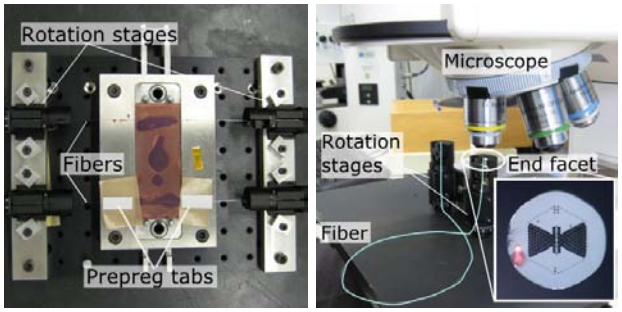

(a) (b)

Figure 6.6: The orientation of an optical fiber can be done using (a) a setup to measure the transverse strain sensitivity along different orientations, or (b) a microscope to visualize the microstructure of the PCF, as shown in the inset

Once the orientation of the fibers is known, the fiber has to be fixed on the prepreg layers to maintain this orientation. This can be done with prepreg tabs or epoxy tabs (Fig.6.7(a) and 6.7(b), respectively). It is important that these tabs do not disturb the final laminate too much, as this would lead to a redistribution of the stresses close to the grating.
There are in total 5 samples fabricated, and two of them are shown in Fig. 6.8. Their dimensions are about 25 cm x 2 cm x 1.6 mm, with the FBG located in the middle of the sample.

6.3 Evaluation of fabrication

6.3.1 Comparison of the FBG reflection spectra before and after embedding

An easy way to determine whether FBGs in the optical fibers have survived the embedding proces and curing cycle, is by looking at their reflection spectrum. Only two of the five fibers appeared to have survived the process, and their spectra before and after embedding are shown in Fig. 6.9.

Comparing the spectra before and after embedding can tell something about the residual

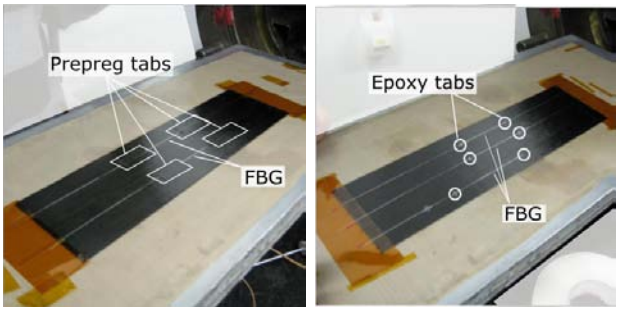

(a) (b)

Figure 6.7: The orientation of an optical fiber can be fixed by using (a) prepreg tabs or (b) epoxy tabs.

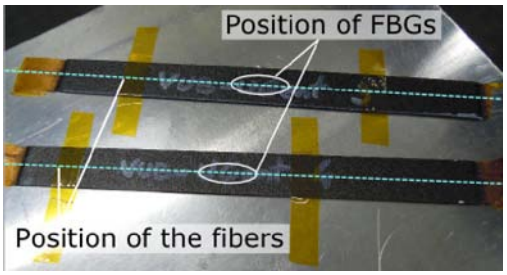

Figure 6.8: Multiple fibers can be embedded in the same CFRP sample. The fabricated sample (as shown in Fig. 6.2(d)) can be cut to several smaller samples, shown here.

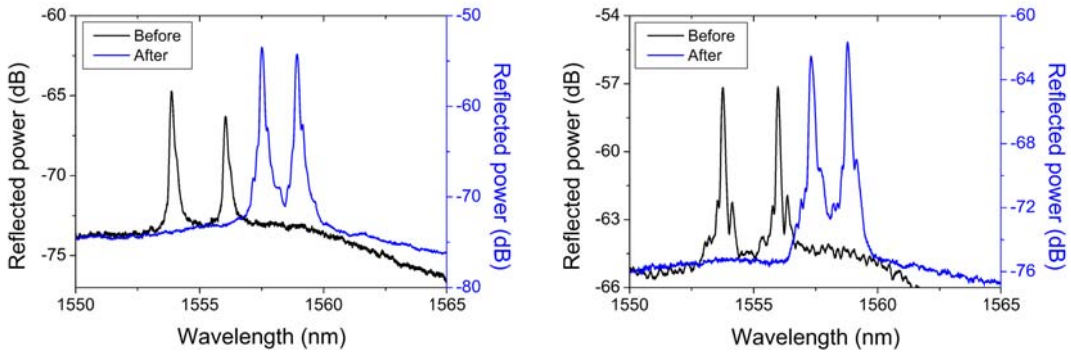

(a) (b)

Figure 6.9: Comparison of the spectra before and after embedding the fiber in a composite sample, (a) Sample 1 and (b) Sample 2. As the optical connections were re-made after embedding, the powerlevels cannot be compared.

strains in the sample and consequently strain acting on the fiber which result in Bragg peak wavelength shifts. In Table 6.2 the values of the Bragg peak wavelengths before and after embedding are listed, together with the corresponding wavelength shift.

Table 6.2: Comparison of the Bragg peak wavelengths in the reflection spectra before and after embedding.

[nm]	Sample 1			Sample 2		
	Before	After	Shift	Before	After	Shift
peak 1 - fast axis	1553.87	1557.50	3.63	1553.76	1557.31	3.55
peak 2 - slow axis	1556.05	1558.93	2.88	1555.98	1558.79	2.81
peak separation	2.18	1.43	-0.75	2.22	1.48	-0.74

The peak wavelength shifts for both samples are comparable, which indicates that the shifts are the result from a consistent build-up of internal strains and not just coincidal.
By embedding the FBG sensors, both Bragg peak wavelengths shift to longer wavelengths. There are several possible contributions to this. An expansion of the laminate in the x'-direction due to the curing of the epoxy, results in an axial straining of the fiber and thus in a positive wavelength shift.
Another possibility is a transverse strain that is the largest along the slow axis of the PCF. In section 5.4.4 it was shown that a transverse loading of the PCF along the slow axis results in a positive shift of the Bragg peak wavelengths. This transverse strain could be induced by a shrinkage in the z' direction of the laminate due to curing of the epoxy.
Another notable change in the reflection spectra before and after embedding, is the decrease of the Bragg peak separation. This is the result of radial and transverse strains acting upon the fiber, but their individual effect is difficult to determine.

6.3.2 Verification of the fiber orientation

The two samples for which a reflection spectrum was detected, were used for extensive testing. Afterwards, these and two other fabricated samples, were cut at the grating itself and at a position before and after the grating to determine the exact orientation of the embedded fiber. In Fig 6.10 the cross-section at the grating of sample 1 and 2 are shown. The intention was to embed these fibers with the slow axis perpendicular to the surface of the sample.

In Table 6.3 a summary is given of the misalignement for the two tested samples and two samples that showed no signal. It is clear that the orientation of the fibers in the tested samples (Sample 1 and 2) is relatively well maintained. The numerical simulation for the transverse line load sensitivity of the bare PCF (section 5.4.4) indicates that a misalignement of 4° corresponds to a decrease in sensitivity of about 2 %. The orientation of the samples

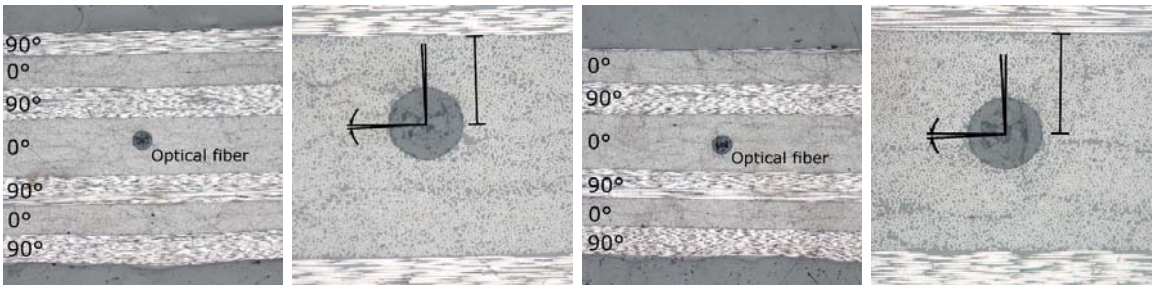

(a) (b) (c) (d)

Figure 6.10: Cross sections of the samples were made to determine the orientation at the position of the grating, (a) Sample 1, (c) Sample 2. In (b) and (d) a close-up is shown, together with the misalignement and embedding depth. The top 90 ° layer in Sample 2 (c) broke off during the preparation of the samples for the images of the cross sections. However, this layer was present as in Sample 1 (a).

that could not be tested (Sample 0a and 0b) has a maximum misalignement of almost 12°, which would correspond to a decrease in transverse sensitivity of the bare fiber of about 7 %.

The embedding depth of the fiber in the 0° layer in the middle of the laminate is also listed in Table 6.3 and it is measured with respect to the 90° as indicated in Fig. 6.10(b) and 6.10(d). As the center 0° layer consists out of 4 layers, its total thickness after fabrication is 400 μm and the embedding depth would be 200 μm in the ideal case. The height of the fiber embedded in Sample 1 differs significantly from the center of the laminate.

Table 6.3: Results for the fabricated composite samples with embedded optical fiber sensors.

	orientation method	Misalignement (°)	Embedding depth μm
sample 1	Microscope	3.70	155
sample 2	Microscope	3.73	181
sample 0a	Strain setup	3.38	211
sample 0b	Strain setup	11.84	208

The evaluation of the fabricated samples by taking cross-sections is a destructive test which is unfavourable as in some cases it is important to evaluate the embedded sensor before actual deployment. In the future it could be possible to visualize the fiber and perhaps even the microstructure while embedded in the composite structure, with advanced visualization techniques such as micro CT scanning or high resolution 3D X-ray micro tomography.
Another solution would be to minimize possible mis-orientations. This could be done by making the cladding of the fiber flat on one side, such that the fiber will automatically rotate

on this side during embedding. A D-clad fiber is an example of a fiber where the cladding is structured with the potential to facilitate its orientation.

6.4 Temperature sensitivity

The goal is to determine the internal strain field of structures with embedded FBGs sensors. In section 5.4.1, it was shown that the Bragg peak separation was (almost) independent of the temperature. This is not necessarily the case for an embedded sensor as thermal strain of the composite structure can transfer strains on the sensor.
For this reason the characterization of the embedded fiber started with a temperature test ('Test 1'). After the axial and transverse strain test, another temperature test ('Test 2') was performed to verify the first results.

Test 1: The first test was performed by placing the samples inside the autoclave that was used only for heating. Its temperature was set at 100°C and the change in Bragg peak wavelengths was monitored with a commercial FBG interrogator (FOS&S FBG-scan 608 interrogator) during heating and cooling down of the sample. The accuracy of the peak detection is 30 pm, while the temperature could be set with an accuracy of 1°C.
Fig. 6.11(a) shows the temperature during the test, that took almost 18 hours. It started with a (controlled) temperature increase of ∼2.2°C/min, followed by an unforced cooling down period of over 17 hours. During cooling down, the temperature in the autoclave can be considered constant in comparison with the measurement speed of the interrogator.

Test 2: The second temperature test was performed using a 'standard' oven, of which the temperature control was less accurate (±5°C). The samples were placed in the oven and the temperature was set at 100°C. Initially, the temperature increased at a rate of ∼4.6°C/min and the unforced cooling down period took almost 10 hours. The temperature cycle is shown in Fig. 6.11(b)

In Fig. 6.12 the resulting change in Bragg peak wavelength and separation is shown, for sample 1 from Test 2. These plots are fitted linearly to obtain a sensitivity in pm/°C. A summary of these sensitivities is given in Table 6.4.

The average sensitivity of the modes polarized along the fast and polarized along the slow, is respectively 3.92 pm/°C and 8.35 pm/°C . The different sensitivity of both modes is a combined effect from the intrinsic thermo-optic effects of the optical fiber, and the thermal strain (axial and transverse) in the composite sample. The release of residual strains (axial and (asymmetric) transverse) of the composite sample, will cause both axes to see a different strain. In section 6.3.1 it was already shown by comparing the spectra before and after

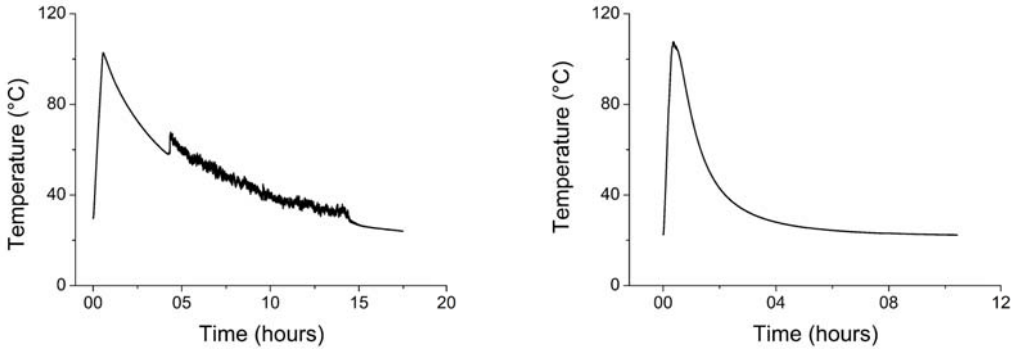

(a) (b)

Figure 6.11: Temperature cycle of (a) Test 1 and (b) Test 2.

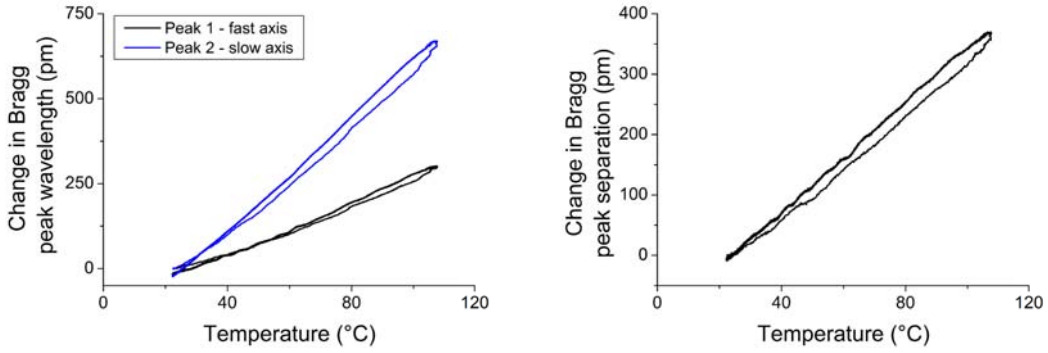

(a) (b)

Figure 6.12: Temperature sensitivity of Sample 1 in Test 2. (a) Bragg peak wavelength response and (b) Response of the Bragg peak separation.

Table 6.4: Temperature sensitivity of FBG sensors fabricated in a Type 3 PCF, embedded in a cross-ply laminate.

	Sample 1 [pm/°C]		Sample 2 [pm/°C]	
	Test 1	Test 2	Test 1	Test 2
peak 1 - fast axis	4.25	3.63	4.22	3.59
peak 2 - slow axis	8.65	8.07	8.68	7.98
peak separation	4.40	4.43	4.46	4.39

embedding, that large amounts of residual strain are presented in the fabricated $[0_2, 90_2]_{2s}$ composite samples. When the samples are cooled down, the residual strains will re-appear.

The decoupling of the thermal strains and the intrinsic thermal effects is not straight forwards. The embedded fibers 'sees' a three dimensional strain and temperature effects of the composite, and intrinsic thermal effects of the optical fiber. Extra tests and numerical simulations should be performed to know the thermal strain effects in the fabricated samples and have an idea of the residual strains.

From these results, it is clear that although the Bragg peak separation for the bare fiber has (almost) zero temperature sensitivity, this is certainly not the case for the embedded fiber. Therefore, another temperature compensating system will have to be used if strain measurements are performed. A common used compensating systems is that of co-embedding a second grating in the same laminate that sees the same temperature but is free from strains. This is achieved by embedding the second grating in a capillary. However, as the dimensions of such a capillary are much larger than the reinforcement fibers, it will heavily disturb the structure of the composite, which is again unfavourable.

6.5 Axial strain sensitivity

The first strain test performed on the samples is an axial strain test. In order to be able to clamp the sample, aluminum tabs were glued at the ends of the sample (Fig. 6.13(a)). These tabs were gripped by the clamps of a mechanical testing machine, and the sample was monotonically loaded in tension (Fig. 6.13(b)).
A reference grating with a well-known axial strain sensitivity (1.2 pm/$\mu\varepsilon$) was glued on the surface of the sample at the position of the grating. The Bragg peak response of this reference grating was used to determine the exact axial strain at the position of the grating.

The test was repeated three times for each sample. The maximum strain was 1000 $\mu\varepsilon$, and the displacement rate was 0.05 mm/min. In Fig. 6.14 the Bragg peak behaviour and peak separation for increasing axial strain is shown for sample 1, during the first test. By linear fitting these plots, an axial strain sensitivity in pm/$\mu\varepsilon$ is obtained. In Table 6.5 the sensitivity of both samples from the three tests are listed.

In section 5.4.2 the axial strain sensitivity of the bare PCF was found to be 1.18 pm/$\mu\varepsilon$ for both Bragg peaks. The obtained sensitivities for an embedded fiber are about the same and range from 1.19 pm/$\mu\varepsilon$ to 1.24 pm/$\mu\varepsilon$, and there is almost no change in Bragg peak separation due to axial strain. For sample 1 a sensitivity of the Bragg peak separation of -0.02 pm/$\mu\varepsilon$ that was consistent for all three tests was found. This small sensitivity can be due to the off-center position of the fiber in the middle 0° layer as was discussed in section

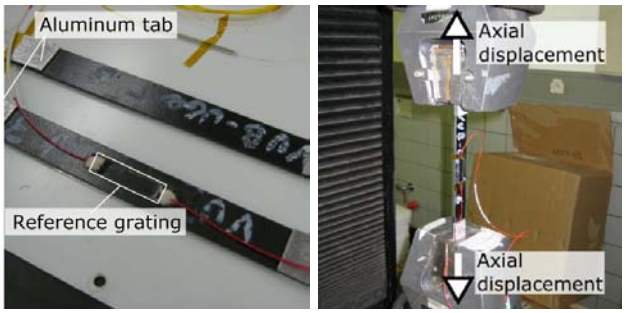

(a) (b)

Figure 6.13: (a) For the axial strain test, aluminum tabs and a reference grating had to be glued onto the sample. (b) The sample was clamped by the grips of a mechanical testing machine.

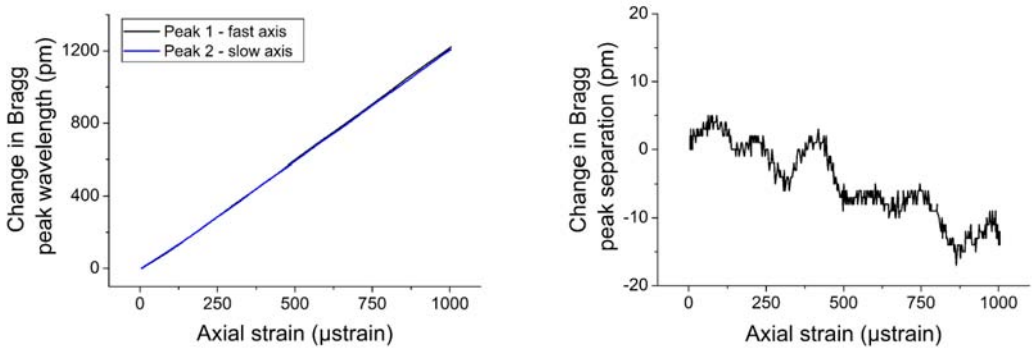

(a) (b)

Figure 6.14: Axial strain sensitivity of Sample 1 in Test 1. (a) Bragg peak wavelength response and (b) Response of the Bragg peak separation.

Table 6.5: Axial strain sensitivity of FBG sensors fabricated in a Type 3 PCF, embedded in a cross-ply laminate.

	Sample 1 [pm/$\mu\epsilon$]			Sample 2 [pm/$\mu\epsilon$]		
	T1	T2	T3	T1	T2	T3
displacement (mm/min)	0.05	0.05	0.05	0.1	0.05	0.05
peak 1 - fast axis	1.24	1.26	1.26	1.19	1.19	1.20
peak 2 - slow axis	1.22	1.24	1.24	1.19	1.19	1.19
peak separation	-0.02	-0.02	-0.02	0.00	0.00	0.00

6.3.2. It is possible that during the axial strain tests, also some bending strain was put on the sample because of the misalignements of the grips of the mechanical testing machine.

6.6 Transverse strain sensitivity

The second type of strain test performed on the samples is a transverse strain test. As discussed in Table 6.1, composite samples feature a very high elastic modulus ($\sim$ 300 GPa) in the direction of the reinforcement fibers, while the elastic modulus in the out-of-plane direction is determined by the epoxy, resulting in a much lower elastic modulus ($\sim$ 6.3 GPa). Strain in the out-of-plane direction can thus pose a threath to the structural integrity of the composite. Monitoring the transverse strain in composite structures is therefore crucial.

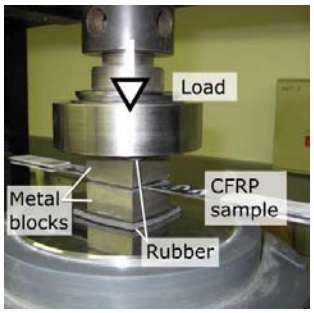

Figure 6.15: For the transverse strain test, metal blocks were glued on each side of the sample, and rubbers were placed between the blocks and compression plates of a mechanical testing machine.

The transverse strain test was performed by compressing the sample in the z' direction (as depicted in Fig. 6.5) by two plates with a mechanical testing machine. To achieve homogeneous loading of the sample, two metal blocks were glued on both sides on the sample. Then pieces of rubber were placed between these blocks and the plates of the testing machine. The applied load was determined using a load cell, and an increasing load of maximum 20 kN was applied, corresponding to a pressure of $\sim$25 MPa. The response of the Bragg peak wavelengths is shown in Fig. 6.16 (results from testing sample 2). By linear fitting these plots a sensitivity for transverse strain in pm/MPa is obtained. In Table 6.6 the sensitivity of both samples is summarized.
The test was performed three times per sample (referred to as T1, T2, T3), and the orientation of the sample with respect to the compression plates was altered to ensure that the compression plates were parallel and load was distributed evenly.

When Table 6.6 is compared with the values obtained for the transverse strain sensitivity of the bare fiber, a similar trend is found. That is, both Bragg peak wavelengths increase with transverse loading, but the overall peak separation decreases. To obtain sensitivities

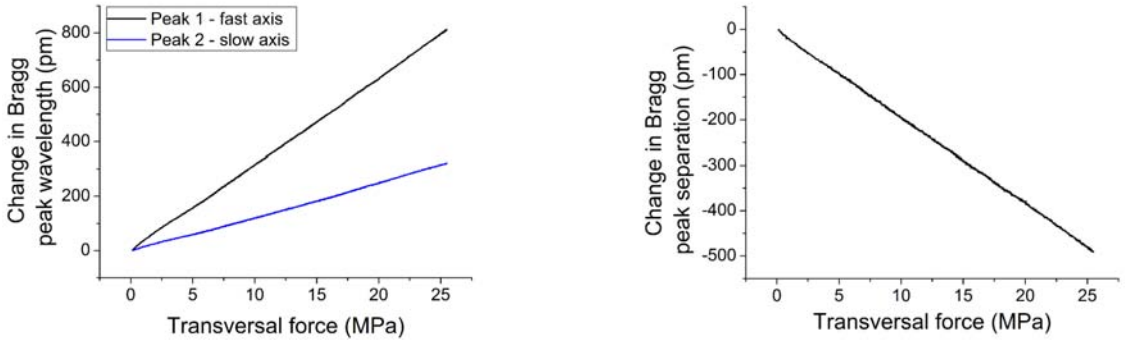

Figure 6.16: Transverse strain sensitivity of Sample 2, Test 1. (a) Bragg peak wavelength response and (b) Response of the Bragg peak separation.

Table 6.6: Transverse strain sensitivity of FBG sensors fabricated in a Type 3 PCF, embedded in a cross-ply laminate.

	Sample 1 [pm/MPa]			Sample 2 [pm/MPa]		
	T1	T2	T3	T1	T2	T3
peak 1 - fast axis	49.81	49.07	48.04	31.70	31.06	30.43
peak 2 - slow axis	19.05	18.80	18.30	12.65	12.61	12.15
peak separation	-30.76	-30.27	-29.74	-19.04	-18.44	-18.29

in pm/$\mu\varepsilon$, the elastic modulus of the composite sample along the z'-axis should be known. Because of the particular stacking used ($[0_2, 90_2]_{2s}$) it is not straight forward to determine this value. Extra tests should be performed to know the exact value. However, a rough estimate would be, as there are no reinforcement fibers along the z'-axis, that the elastic modulus equals that of the epoxy, which is about 6 GPa. If this is taken into account, the values of Table 6.6 (in pm/MPa) correspond to the sensitivities (in pm/$\mu\varepsilon$) in Table 6.7.

Table 6.7: FBG sensitivities versus transverse strain of the composite material if $E_{z'}$=$E_{2'2'}$=6.3GPa

	Sample 1 [pm/$\mu\epsilon$]			Sample 2 [pm/$\mu\epsilon$]		
	T1	T2	T3	T1	T2	T3
peak 1 - fast axis	0.31	0.31	0.30	0.20	0.20	0.19
peak 2 - slow axis	0.12	0.12	0.12	0.08	0.08	0.08
peak separation	-0.19	-0.19	-0.19	-0.12	-0.12	-0.12

There are no earlier reported values about HiBi fibers embedded in a cross-ply laminate and therefor it is difficult to make a founded comparison. However, in reference [30] bow-tie fibers and Type 1 PCFs were embedded between the second and third layer of a 16-layer unidirectional carbon fiber/epoxy laminate and a transverse strain test was performed with the same setup as shown in Fig. 6.15. Their results are compared with the average value of the embedded Type 3 PCFs in Table 6.8.
The Type 3 PCF has a transverse strain sensitivity of the Bragg peak separation that is an order of magnitude higher than an embedded bow-tie fiber, and even higher than an embedded Type 1 PCF. This clearly shows that the enhanced transverse strain sensitivity of a bare Type 3 PCF results in a significant increase in transverse strain sensitivity of an embedded fiber.

Table 6.8: Transversal strain sensitivities of different types of HiBi fiber embedded in carbon fiber/epoxy laminates. It should be noted that the lay-up and testing method was different for the bow-tie fiber and Type 1 PCF.

[pm/$\mu\varepsilon$]	Type 3 PCF	Bow-tie fiber [30]	Type 1 PCF [30]
peak 1 - fast axis	0.25	0.060	0.040
peak 2 - slow axis	0.10	0.075	0.053
peak separation	-0.16	-0.016	-0.012

6.7 Conclusion

Type 3 PCFs were succesfully embedded in carbon fiber/epoxy laminates with a cross-ply layup. The orientation of the optical fiber was taken into account and the fast axis was

embedded parallel to the laminate surface.
A comparison was made of the reflection spectra before and after embedding, and this showed that large amounts of residual strains were present in the fabricated cross-ply laminates. This caused the Bragg peaks to shift to longer wavelengths while the overall peak separation decreased. This behaviour is a combination of several strains, such as axial, radial and transverse strain. To determine the exact amounts of each strain, extra tests and FEM simulations should be performed.
However, the sensor was still perfectly useable because the peak separation was still large enough and the peaks had not deformed.

Since the residual strains are an indication of the curing state of the laminate, the shift in Bragg peak wavelengths and peak separation can be used to monitor curing during fabrication of the composite samples.

With a destructive test that was performed after all other tests were performed, cross-sections of the samples were made to determine the orientation of the fiber and the embedding depth. This showed that the fiber orientation was maintained during embedding.

The thermal calibration showed that the Bragg peaks shift to longer wavelengths when the samples are heated, with the increase of the slow axis twice as high as the increase of the fast axis. This resulted in a sensitivity of 4.4 pm/°C of the Bragg peak separation, while this was nearly zero for the bare fiber. This is likely the result of the residual strains that are released during heating and restored during cooling.
The temperature sensitivity of the embedded fiber is a combination of temperature effects and multi-axial strain effects. Extra tests and simulations should be performed to know the exact contributions.

The axial strain calibration showed an axial strain sensitivity comparable with that of the bare PCF, and both Bragg peaks have a sensitivity of about 1.2 pm/$\mu\varepsilon$ while the peak separation is insensitive to axial strain.

The final test was a transverse strain calibration and this was done by glueing metal blocks to the sample and compressing the sample via loading of these blocks. The average sensitivity of the peak separation was found to be about -26 pm/MPa, but there was a small difference between the two tested samples. This is the result from the off-center positioning of the optical fiber in one of the samples, which resulted in a slightly higher sensitivity.
Since the elastic modulus in the direction of applied load is determined by the epoxy, the values in pm/MPa can be calculated to values in pm/$\mu\varepsilon$. The average sensitivity of the peak separation is then -0.16 pm/$\mu\varepsilon$.
Earlier reported values of a bow-tie fiber and Type 1 PCF embedded in a carbon fiber/epoxy laminate with unidirectional layup showed a transverse strain sensitivity that was an order of

magnitude smaller than the sensor reported here, which is a breakthrough for FRP materials.

The overall conclusion of this chapter is that the enhanced transverse strain sensitivity of a Type 3 PCF has a distinct added value when embedding the fiber in composite materials for structural health monitoring.

Chapter 7

Optical fiber sensors embedded in polymers

7.1 Outline and objectives

As mentioned in chapter 2, the combination of smart materials and fiber optic sensors opens the door to many new applications such as optical skin. This is a (flexible) polymer sheet with FBG sensors embedded and that can be used for tactile sensing. This sheet can be wrapped around or attached to irregular and moving objects to monitor pressure distributions.
Optical skins are still a very young research domain and therefore the focus of my work goes to investigating the possibility of embedding an FBG sensor in different types of polymer and with different fiber configurations. Moreover, I will investigate the transverse load sensitivity of an embedded sensor for polymers with varying material properties. Since the elastic modulus of (flexible) polymers is much smaller than that of a silica fiber, one could assume that a transverse loading of the polymer is seen as hydrostatic pressure by the embedded sensor. Therefore, FBG sensors fabricated in Type 2 or Type 3 PCFs are suited to embed in optical skins as they have a high hydrostatic pressure sensitivity and transverse line load sensitivity.

In section 7.2 2D simulations are performed on a bow-tie fiber and a Type 3 PCF embedded in a polymer tube. The influence of the elastic modulus and Poisson ratio are investigated. This is done by applying a transverse line load to the sample along different angles.
In the experimental work, FBG sensors fabricated in bow-tie fibers and embedded in polymer tubes are tested on their transverse line load sensitivity. Types of polymers with a different flexibility are investigated. Bow-tie fibers are used as their respons to transverse loading is already well-known, such that different results of multiple samples can be linked to the polymer itself and not the fiber.

In section 7.3 experiments are performed on 'optical skins'. FBG sensors fabricated in Type

2 and Type 3 PCFs are embedded in different types of polymers, with different fiber lay-out and different sample dimensions.
A setup is built to determine the response of the embedded FBG sensor when a load is applied at different positions of the skin. The sensitivity will depend on the skin thickness, embedding depth of the fiber and the sensitivity at a certain distance from the fiber.

7.2 Fibers embedded in a polymer tube

7.2.1 FEM simulations

Typical values for PMMA are an elastic modulus E of 1.8 - 3.1 GPa and a Poisson ration ν of 0.35 - 0.4, but the properties of a cured polymer are heavily dependent on the fabrication method. Therefore, numerical simulations are made to have an idea of the influence of E and ν on the sensitivity of the Bragg peak wavelengths.

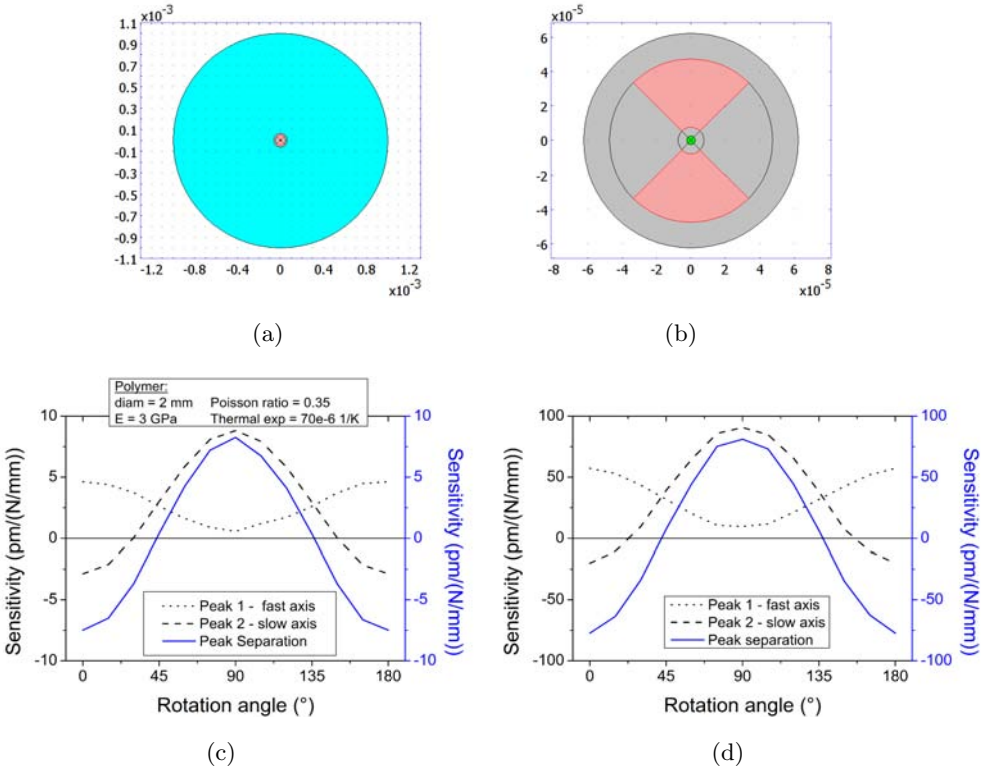

Figure 7.1: Geometrical model (a) and transverse line load sensitivity (c) of an FBG sensor fabricated in a bow-tie fiber and embedded in a polymer tube with a diameter of 2 mm, $E = 3$ GPa, $\nu = 0.35$ and $\alpha =$ 70E-6 $1/K$. For comparison, in (b) and (d) the geometrical model and sensitivity of a free standing bow-tie fiber with a diameter of 125 μm are shown.

Simulations were performed on a bow-tie fiber with a geometrical model as discussed in section 5.2.1 and embedded in a polymer tube with a diameter of 2 mm, elastic modulus E of 3 GPa and Poisson ration ν of 0.35. A line force of maximum 10 N/mm was applied on the cross section along different directions. In Fig. 7.1(a) the geometrical modal is shown, and the resulting plot of transverse line load sensitivity versus rotation angle is shown in Fig. 7.1(c). In Fig. 7.1(b) the geometrical model a bare bow-tie fiber is shown, with in Fig. 7.1(d) the transverse line load sensitivity of a bare bow-tie fiber, as was calculated in section 5.4.4.

The peak separation in Fig. 7.1(c) has a minimum sensitivity of -7.5 pm/(N/mm) when a load is applied along the slow axis and a maximum sensitivity of 8.3 pm/(N/mm) when applied along the fast axis. When comparing this with the values of a free standing bow-tie fiber in Fig. 7.1(d), it is clear that the overall sensitivity of an embedded bow-tie fiber is almost an order of magnitude lower. This is because the complete cross section over which the applied load is distributed, is larger for the embedded fiber (diameter $\sim$ 2 mm) than for the bare fiber (diameter $\sim$ 125 μm).

Another simulation was performed to determine the change in sensitivity when the elastic modulus of the polymer tube is varied. A transverse strain was applied along the fast axis of an embedded bow-tie fiber, which corresponds to the direction where the peak separation is the most sensitive. The elastic modulus of the polymer was varied between 0.3 GPa and 12 GPa. The resulting plot (Fig. 7.2) shows that the sensitivity of the Bragg peak separation decreases with increasing elastic modulus.
This indicated that a more rigid polymer tube will protect the fiber from external forces, while a more flexible polymer transfers the external load onto the embedded fiber.

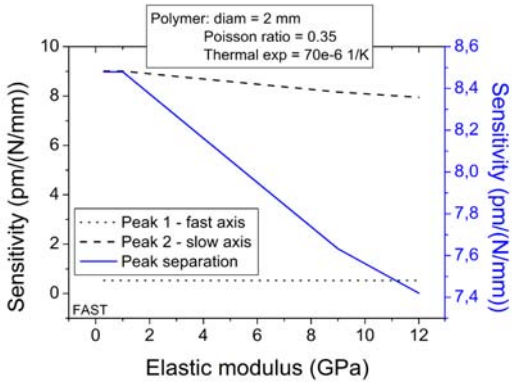

Figure 7.2: Influence of the elastic modulus E of the polymer tube on the sensitivity of the Bragg peak separation of an FBG sensor fabricated in a bow-tie fiber, when a transverse line load is applied along the fast-axis.

The same types of simulations were performed on a Type 3 PCF with a model as explained in

section 5.2.2, and that was embedded in a polymer tube. The influence of the elastic modulus and the Poisson ratio of the polymer on the sensitivity is determined when the embedded PCF is transversally loaded along the slow axis. The results are shown in Fig. 7.3(a) and 7.3(b).

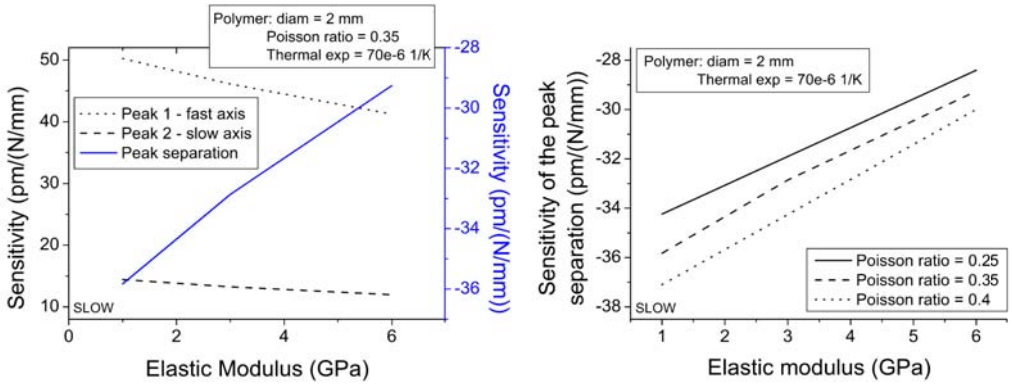

(a) (b)

Figure 7.3: Influence of (a) the elastic modulus and (b) the Poisson ratio of the polymer tube on the sensitivity of the Bragg peak separation of an FBG sensor fabricated in a Type 3 PCF, when a transverse line load is applied along the slow axis.

From Fig. 7.3(a) it is again clear that the sensitivity of the peak separation decreases (the absolute value decreases) with increasing elastic modulus, which corresponds to the results from the simulation on an embedded bow-tie fiber (Fig. 7.2).
Typical values for the Poisson ratio ν of PMMA are 0.35 - 0.4, and in Fig. 7.3(b) the influence of the elastic modulus of the polymer on the sensitivity of the Bragg peak separation is given for different Poisson ratios (0.25 - 0.4). It is clear that the magnitude of the sensitivity decreases for decreasing Poisson ratio.
Fig. 7.4 shows that the sensitivity of the fiber also decreases with increasing elastic modulus when the load is applied along the fast axis.

7.2.2 Experiments

The characterization of FBG sensors fabricated in bow-tie fibers and embedded in polymer tubes is also done via experiments. The fabrication of the tested samples was not a part of this Master thesis, but the basic principles are discussed to situate the subject.

Material development and fabrication of fibers embedded in polymer tubes

The choice of polymer for the development of flexible substrates was based on the ability to adjust the mechanical properties of the material, as well as their chemical resemblance

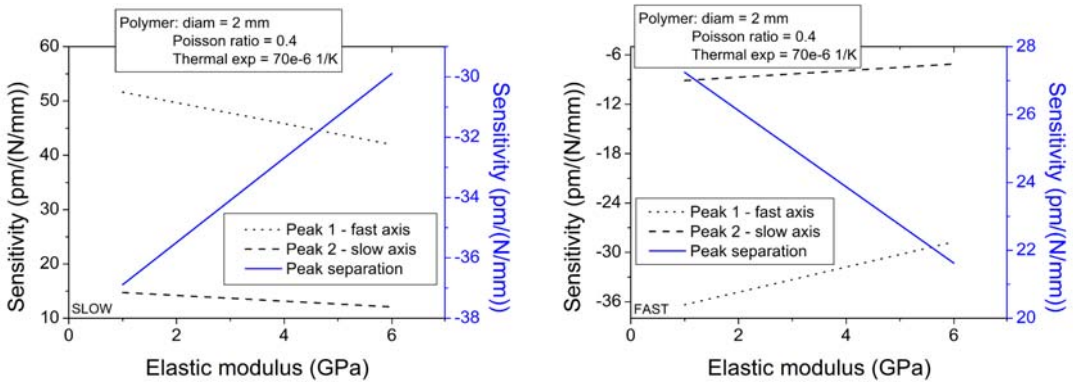

Figure 7.4: Sensitivity of the peak separation of a FBG sensor fabricated in a Type 3 PCF and embedded in a polymer tube (diameter = 2 mm, $\nu = 0.4$ and α = 70E-6 $1/K$), when a transverse line load is applied along (a) the slow axis and (b) the fast axis.

with fiber coatings (polymethacrylate based material). The biocompatibility was also a requirement, as this allows the use of the optical skin for medical purposes. The selected monomers are MMA, BuMA and EHMA, and different mixtures of MMA/BuMA and MMA/EHMA are used to adapt the flexibility of the material. The flexibility of a polymer is difficult to determine as this is heavily dependent on the fabrication process and these could be determined with elaborate testing of the mechanical properties of the polymer. However, a far simpler method to estimate the flexibility of a polymer is by looking at the glass transition temperature (T_g), that decreases with increasing flexibility. In Table 7.1 an overview is given of T_g for different compositions. Also shown is the temperature up untill which the material is stable (decomposition temperature, T_{decomp}).

Table 7.1: Glass transition temperature and decomposition temperature of different MMA-based compositions. [37]

	MMA/BuMA				MMA/EHMA		
	composition (mol%)	T_g (°C)	T_{decomp} (°C)		composition (mol%)	T_g (°C)	T_{decomp} (°C)
MX1	80/20	96	228	MX4	80/20	51	222
MX2	50/50	66	231	MX5	50/50	29	230
MX3	20/80	51	—	MX6	20/80	-4	229

The production process of the polymer and fabrication of the polymer tubes are both very elaborate techniques, and as it was not done in the framework of this thesis, their details will

not be discussed, but are explained in [37]. Polymerization occurs under influence of UV-light and a glass mould is used to produce fiber embedded polymer tubes (Fig. 7.5(a)). An optical fiber can be placed in the center of the mould, and a fiber embedded in a polymer tube is shown in Fig. 7.5(b).

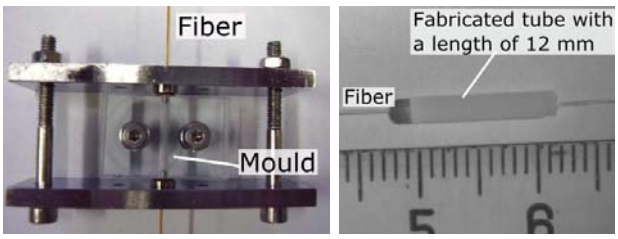

(a) (b)

Figure 7.5: (a) UV-transparant mould for the fabrication of fiber embedded polymer tubes. (b) Example of a fiber embedded in a polymer tube with a length of 12 mm. [37]

Experimental setup for transverse line load tests

A possible setup to measure the transverse line load sensitivity is shown in Fig. 7.6. The fiber is clamped in between two rotation stages that can be controlled manually. This is done in order to keep axial strain on the fiber constant and to determine the sensitivity along different orientations of the fiber. The sensor embedded in a polymer tube is placed in between two steel pressure plates and weights can be manually added on top.
The fiber itself is connected with a directional coupler to an ASE source and OSA for Bragg peak detection (accuracy of 10 pm, resolution of 1 pm).

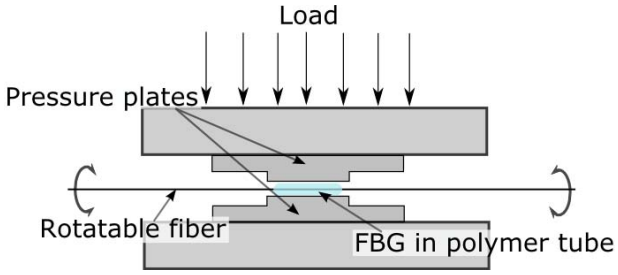

Figure 7.6: Setup to determine the transverse line load sensitivity of a FBG sensor embedded in a polymer tube along different angles. Weights are added manually on top of the pressure plate.

Three polymer tubes are tested; a PMMA sample with an unknown glass transition temperature, a MMA/BuMA 50/50 sample (T_g=66°C) and a MMA/EHMA 50/50 sample (T_g=29°C), with a tube length of 12 mm, 14 mm and 16.2 mm, respectively.

PMMA

In Fig. 7.7(a), the reflection spectrum of an FBG sensor fabricated in a bow-tie fiber and embedded in a PMMA tube is shown, and there are two Bragg peaks clearly visible. The transverse loading test was performed with a maximum load of 4.25 N/mm. The sensitivity of the Bragg peaks and peak separation is determined for several orientations (every 15° over a total of 180°) and the resulting plot is shown in Fig. 7.7(b).

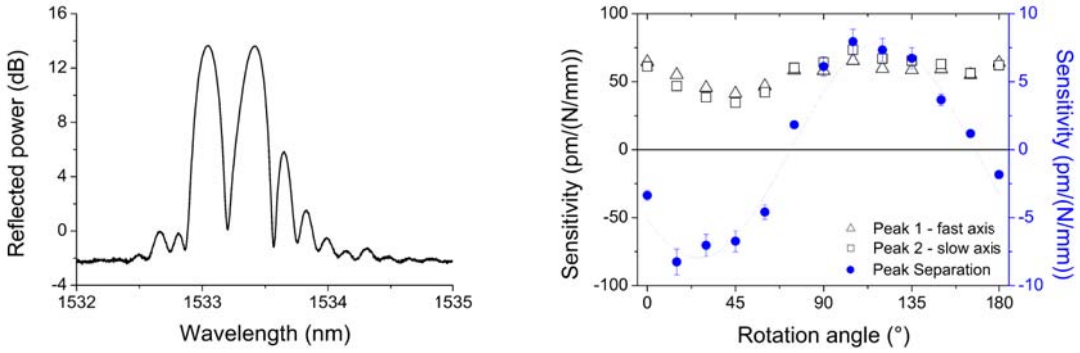

(a) (b)

Figure 7.7: FBG sensor fabricated in a bow-tie fiber and embedded in a PMMA tube: (a) Reflection spectrum and (b) Transverse line load sensitivity.

From Fig. 7.7(b) it is clear that there is an orientation dependence of the sensitivity and that the sensitivity is sine-like, as is the case for a non-embedded sensor (section 5.4.4). There seems to be an off-set of about 50 pm/(N/mm) on the sensitivity of the separate Bragg peaks, but this is not the case for the sensitivity of the Bragg peak separation. This can be an indication that the off-set is due to axial effects, as these have no result on the peak separation. A possible explanation is that by compressing the polymer, its length will increase which results in an elongation of the grating and this causes an increase of the Bragg peak wavelength leading to a positive off-set.
The peak separation has a minimum sensitivity of -8.26 pm/(N/mm) and a maximum sensitvity of 7.95 pm/(N/mm) for a line load applied along the slow and fast axis, respectively. These sensitivities are significantly lower than those obtained for a free standing FBG sensor fabricated in a bow-tie fiber. This is the result from the strain that is distributed over a larger area in an embedded fiber (diameter ∼2 mm) than in a bare fiber (diameter ∼125 μm), implying lower line loads seen by the sensor itself.
The obtained sensitivities correspond very well with the simulated sensitivities in Fig. 7.1(c) for a polymer with elastic modulus 3 GPa and a Poisson ratio of 0.35, indicating that these correspond to the material properties of the tested PMMA tube.

MMA/BuMA 50/50

The reflection spectrum of an FBG sensor fabricated in a bow-tie fiber and embedded in a composition of MMA/BuMA 50/50 is shown in Fig. 7.8(a). The spectrum is heavily deformed, being the result from unequal strains on different positions along the Bragg grating. Still, a transverse line load test was performed on the sample with a maximum load of 3.65 N/mm and the behaviour of the two peaks indicated in Fig. 7.8(a) is followed. As there is no indication that these two peaks are the Bragg peaks, the resulting sensitvities will only be an indication of the order of magnitude. The sensitivity of the embedded sensor loaded under different orientation angles, is shown in Fig. 7.8(b). Data is missing for several orientations, as the reflection spectrum was often too heavily deformed and peak determination was no longer possible.

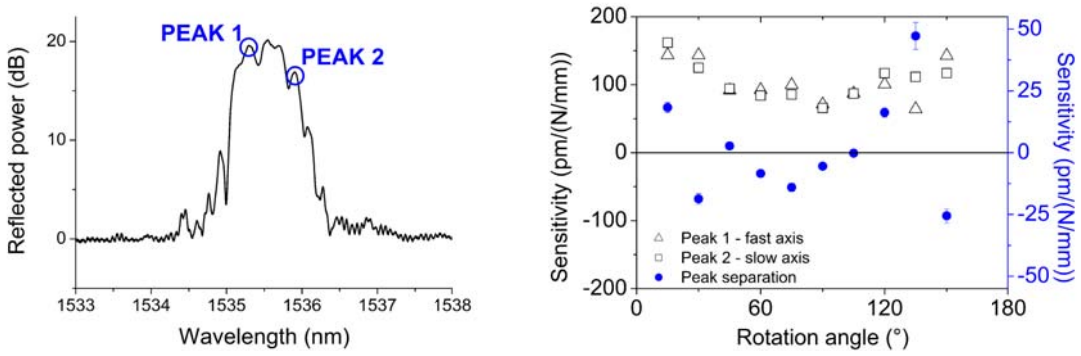

(a) (b)

Figure 7.8: Reflection spectrum of an FBG sensor fabricated in a bow-tie fiber and embedded in an MMA/BuMA 50/50 tube: (a) Reflection spectrum and (b) Transverse line load sensitivity.

The sensitvity of the separate Bragg peaks again show an offset, here about 100 pm/(N/mm). This implies that the axial effects resulting from transverse loading of a MMA/BuMA 50/50 are twice as large as for a PMMA sample. This indicates that the Poisson ratio ν of fabricated MMA/BuMA 50/50 tubes is smaller than of PMMA tubes.
The sensitivity of the Bragg peak separation shows no clear sine-like trend and outliers at 30° and 150° (and maybe 135°). If these points are not considered, the minimum sensitivity is about -14 pm/(N/mm) and the maximum sensitivity about 18 pm/(N/mm). Although these values can only be an indication of the order of magnitude, there is a slight increase in sensitivity of the peak separation compared to a sensor embedded in a PMMA tube. Since PMMA has a higher elastic modulus than MMA/BuMa 50/50, this observation corresponds to the simulations in section 7.2.1, where it was shown that the transverse line load sensitivity

is higher for a polymer with a smaller elastic modulus.

MMA/EHMA 50/50

The reflection spectrum of an FBG sensor fabricated in a bow-tie fiber and embedded in a MMA/EHMA 50/50 tube, is shown in Fig. 7.9. The spectrum clearly shows two Bragg peaks, but the tube itself was too heavily deformed and prohibited reliable testing. The tube is no longer cylindrical but rectangular, the thickness of the sample differs along the length of the tube ('tapered rectangle') and the sample is slightly bended. These deformations are likely the result of the low glass transition temperature $T_g = 29$ °C which makes the sample very soft.

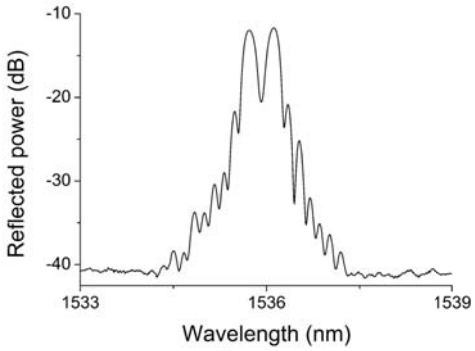

Figure 7.9: Reflection spectrum of an FBG sensor fabricated in a bow-tie fiber and embedded in an MMA/EHMA 50/50 tube.

7.3 Fibers embedded in a polymer skin

As mentioned in the the introduction in section **??**, I also investigated FBG sensors embedded in polymer skins. These results are presented here.

7.3.1 Used materials and fabrication methods

PDMS

PDMS (polydimethylsiloxane) is an organic polymer that is used for many types of applications. It is a UV or thermal curable polymer that has a viscosity that is highly dependent on the fabrication of the polymer. Since PDMS is chemically inert, biocompatibel and flexibel, it is an ideal polymer for optical skins. The PDMS used in this work is Sylgard 184 (Dow Corning).

There are different techniques to embed optical fibers in a PDMS polymer sheet. Both techniques are based on making small traces in a bottom layer of PDMS in which the fiber

can be fixed before placing another PDMS layer on top. The traces can be made by either soft lithography or laser structuring.

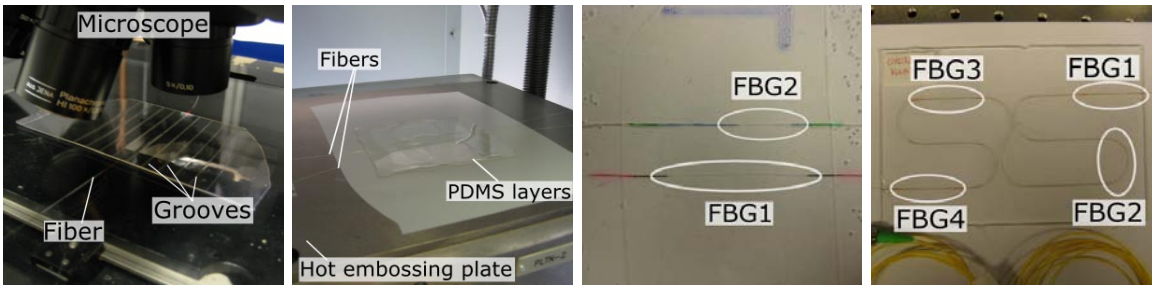

(a) (b) (c) (d)

Figure 7.10: (a) Fibers are placed in the grooves of a cured PDMS layer with the aid of a microscope. (b) Another layer of PDMS is placed on top with hot embossing. (c) A fabricated sample with two fibers embedded in the same skin along a straight line. (d) By embedding a fiber with an array of gratings in a meandered fiber layout an optical skin based on multiplexing is obtained.

In the soft lithography technique a 'stamp' with the fiber layout is imprinted in a layer of PDMS during thermal curing. The layout of the stamp is made with lithography resulting in very accurate dimensions and positioning of grooves in which the fibers can be placed. Another advantage of this technique is that the stamp can be used several times.
After imprinting the fiber layout in the PDMS layer, the optical fiber is placed inside the traces using a microscope (Fig. 7.10(a)). It is possible to take the orientation of the fiber into account during this step. A UV curable adhesive is used to fix the fibers inside the traces before moving the sample to a hot embossing setup. The PDMS layer with the fibers placed in the grooves is covered by another layer of cured PDMS with an uncured layer of PDMS placed in between to ensure adhesion and minimize the amount of air bubbles. This lay-up is then placed in a hot embossing setup to thermally cure the PDMS (Fig. 7.10(b)). The final thickness of the sample is determined by the thickness of the different PDMS layers used.

Laser ablation with a CO_2 laser can also be used to make grooves in a layer of (cured) PDMS. The advantage of this technique is that it fully automatically transfers a CAD file with the desired layout into grooves in the PDMS layer. Laser structuring is preferred over soft lithography if the fiber layout is more complex, for example in a meandered layout (Fig. 7.10(d)).
Like in the soft lithography step, the fiber is placed inside the grooves using a microscope and the layer is covered with another layer of PDMS using hot embossing.

A PDMS sample (Sample 1) was fabricated using the soft lithography technique, with a Type

2 and Type 3 PCF (Sample 1A and Sample 1B) embedded in straight grooves about 1 cm apart of each other (Fig. 7.10(c)). Both fibers are oriented with their slow axis perpendicular to the sample surface. The total sample thickness is about 1 mm with the fibers in the middle of the skin, and the dimensions of the skin are 4 cm × 6 cm.

Another PDMS sample (Sample 2) was available for testing. A Type 2 PCF is embedded in a skin with a meandered fiber layout that was fabricated using the laser structuring technique (Fig. 7.10(d)). The fiber has an array of 4 gratings inscribed and due to the total length of the fiber it was difficult to take orientation of the fiber into account. The total sample thickness is about 3 mm thick and has dimensions of 8 cm × 10 cm.

Ormocer

Ormocer is an ORganically MOdified CERamic material that is UV-curable and has a limited flexibility. It is often used for micro-optical applications and planar optical wave guiding as it has excellent optical properties. On the other hand, it can also be used for embedding optical fibers sensors to create a (limited) flexible skin.

Ormocer skin samples are produced by injecting the polymer in a UV-transparant mould, with the FBG placed in this mould, as depicted in Fig. 7.11(a). To avoid air bubbles and uneven distribution of the (liquid) polymer, air outlets are foreseen in the top lit. The injected mould is illuminated with UV light to cure the polymer and a fabricated sample is shown in Fig. 7.11(b). The final step is a hardbake procedure to ensure thermal and environmental stability of the polymer.

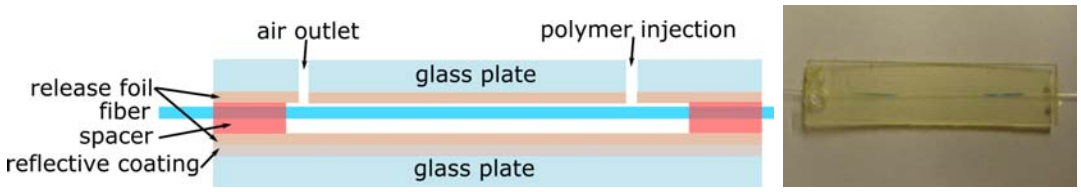

(a) (b)

Figure 7.11: (a) Cross section of the buildup of the injection mould used for the fabrication of Ormocer samples. (b) An example of an FBG sensor embedded in Ormocer

The fabricated Ormocer samples are 1 cm × 4 cm large and have a thickness of 1 mm with the fiber embedded at a depth of only 100 μm. Since there is no prestrain on the fiber during curing, nothing prevents the fiber from bending. This will result in a varying embedding depth along the length of the grating. Moreover, as the fiber is not clamped or fixed during curing, it is likely that the embedded fiber is not oriented along the intended direction. Some

of the fabricated samples also have surface irregularities or are bended over the total length. All of these flaws can make it difficult to obtain consistent results.

7.3.2 Transverse loading setup

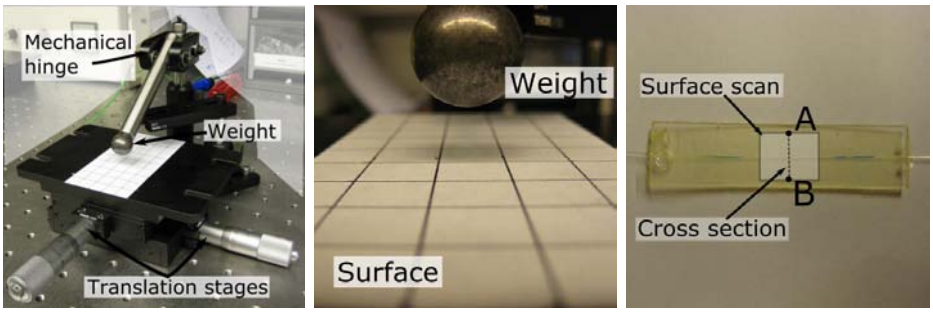

(a) (b) (c)

Figure 7.12: (a) The setup to scan the polymer skins consists out of two translation stages and a metal ball of 0.45 N (b) attached to a fully mechanical release system. (c) indicates at which positions the sensitivity is determined when a surface scan or a cross section is made.

A fully mechanical setup is built to determine the transverse load sensitivity at different positions of the optical skin (Fig. 7.12(a)). The position is determined by two translation stages with each a range of 25 mm and accuracy of 10 μm. A small metal ball attached to a hinge is used to apply a force of about 0.45 N to the skin (Fig. 7.12(b)). As this is fully mechanical, the weight is constant for all positions during testing.
The surface can be scanned to determine the transverse load sensitivity at different positions. The sensitivity is determined by monitoring the response $\delta\lambda$ of the Bragg peak wavelengths every time the weight is placed on and removed from the optical skin. A commercial FBG interrogator (FOS&S FBG-scan 608 interrogator) is used to determine the Bragg peak wavelengths with an accuracy of 30 pm and resolution of 1 pm.

7.3.3 Experimental results

PDMS samples

The reflection spectra of the two FBG sensors (Type 2 and Type 3 PCF) embedded together in the PDMS skin (Sample 1A and 1B) are shown in Fig. 7.13(a) and Fig. 7.13(b). Both spectra show that embedding has caused the peaks to slightly shift to shorter wavelengths, but that the peaks have not deformed.

Testing of Sample 1B was done by making a surface scan of the response of the Bragg peaks

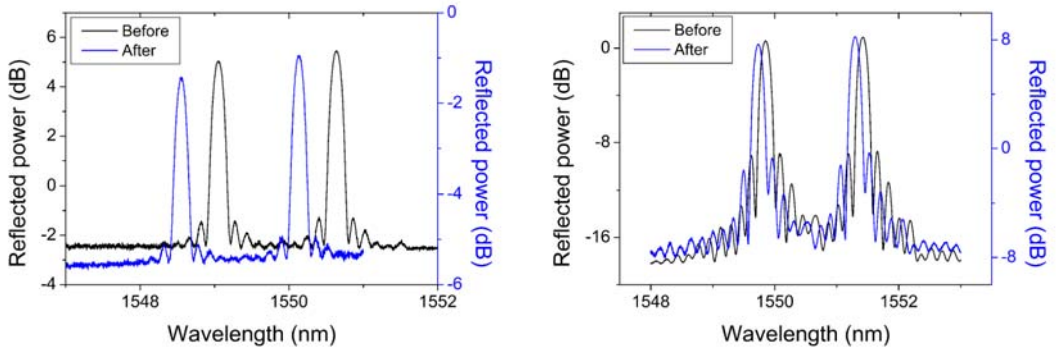

Figure 7.13: Reflection spectra of the FBG sensors embedded in a PDMS skin: (a) Sample 1A (Type 2 PCF) and (b) Sample 1B (Type 3 PCF).

when the weight is placed on several positions on the optical skin. The resulting color plots for both Bragg peaks and the peak separation is shown in Fig. 7.14. In Fig. 7.15 a more detailed cross section is shown that was made by crossing the sample at the center of the grating.

The color plots and the cross-section clearly show an increased sensitivity at the position of the grating. The maximum change in Bragg peak wavelength $\delta\lambda_{\max}$ is 33 pm for the mode polarized along the fast axis, and 31 pm for the mode polarized along the slow axis, and the $FWHM$ is for both Bragg peaks around 1.4 mm.
The color plot for the sensitivity of the Bragg peak separation also show a higher sensitvity at the position of the grating, albeit only a sensitivity of about 3 – 4 pm. At a distance of 5 mm away from the grating, this sensitivity has decreased to nearly zero.

Testing of PDMS Sample 1A (Type 2 PCF) was difficult because it seemed as if the fiber was not well placed inside the groove before curing the PDMS sample. This caused the fiber to move whenever pressure was put near the embedded fiber, resulting in other effects than pure transverse strain. Therefore, only a cross section of the sensitivity could be made at the center of the FBG where the fiber was at a stable position. The result is shown in Fig. 7.16. This skin has a maximum change in Bragg peak wavelength $\delta\lambda_{\max}$ of 94 pm, and both Bragg peaks behave in more or less the same way.

The spectrum of PDMS Sample 2 (Type 2 PCF) with an array of four gratings embedded in a meandered layout is shown in Fig 7.17. Due to bending of the fiber, the reflected power of the gratings was very low and since some gratings were positioned in a bend, their spectrum was heavily deformed. This made it difficult to detect all Bragg peaks and therefore only one

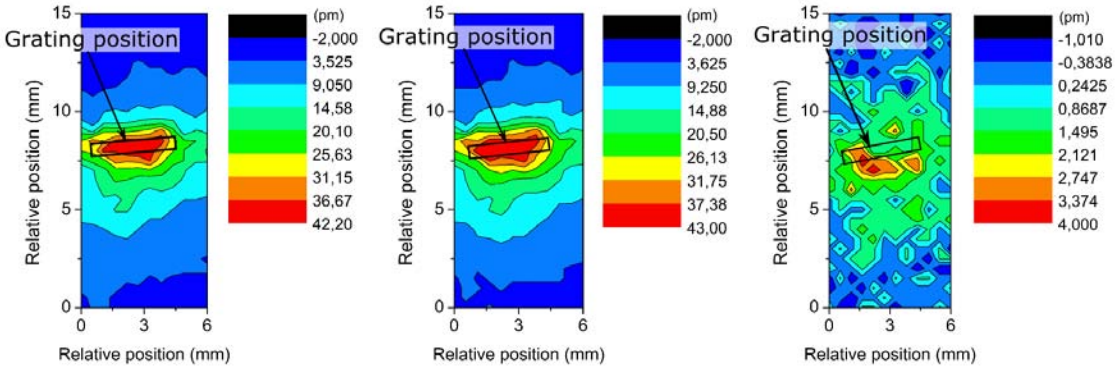

(a) (b) (c)

Figure 7.14: Color plots that show the change in Bragg peak wavelength (in pm) when a load of 0.45 N is applied at different positions of PDMS Sample 1B (Type 3 PCF): The sensitivity of the mode polarized along (a) the fast axis, (b) the slow axis and (c) the sensitivity of the Bragg peak separation.

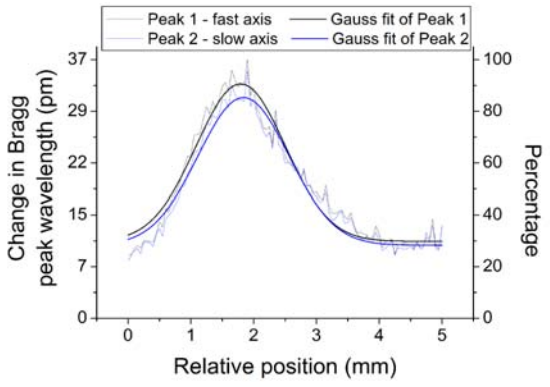

Figure 7.15: Cross section of the transverse load sensitivity at the center of the grating of PDMS Sample 1B (Type 3 PCF). Both curves are approximated by a Gaussian fit, and the obtained parameters for Peak 1 (fast axis) are $R^2 = 0.9550$, $\delta\lambda_{\max} = 33$ pm and $FWHM = 1.41$ mm. The obtained parameters for Peak 2 (slow axis) are $R^2 = 0.9581$ $\delta\lambda_{\max} = 31$ pm and $FWHM = 1.44$ mm.

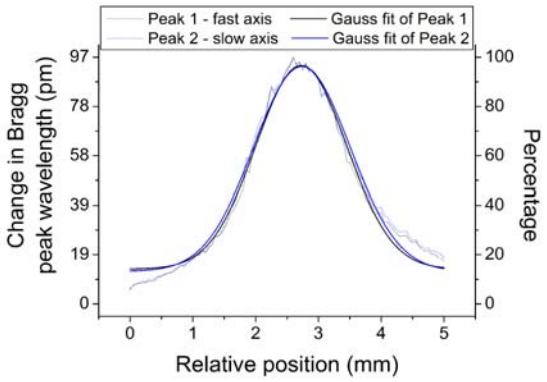

(a)

Figure 7.16: Cross section of the transverse load sensitivity at the center of the grating of PDMS Sample 1A (Type 2 PCF). Both curves are approximated by a Gaussian fit and leaded to a $FWHM_{\text{Peak1}} = 1.44$ mm and $FWHM_{\text{Peak2}} = 1.54$ mm.

grating could be tested. This Bragg peaks reflected by this grating are indicated in Fig. 7.17, and this FBG corresponds to FBG1 in Fig. 7.10(d).

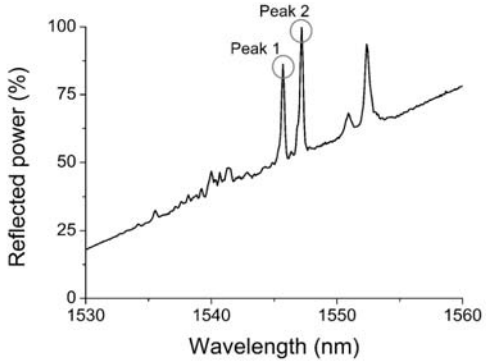

(a)

Figure 7.17: Reflection spectra of an array of FBG sensors fabricated in a Type 2 PCF and embedded in a PDMS skin with a meandered fiber layout (Sample 2).

The grating that could be used for testing PDMS Sample 2 was situated at the edges of the skin. Because of the thickness of the skin, it was bended and only made contact with the surface plate with its edges. This resulted in other effects than transverse strain when placing the load on the skin. In order to perform reliable transverse load tests, pre-strain should be placed on the skin such that it is slightly stretched ann at least flat. Since this was not possible with the transverse setup as shown in Fig. 7.12(a), no consistent or reliable results were obtained for the meandered skins.

Ormocer samples

There are in total four Ormocer samples that were be tested, two Type 2 PCF embedded samples and two Type 3 PCF embedded samples. Because some of the samples were bended, it was impossible to make a surface scan without destabilizing the sample. Therefore, only cross sections of the sensitivity could be made at the (visibly) stable position of the sample.

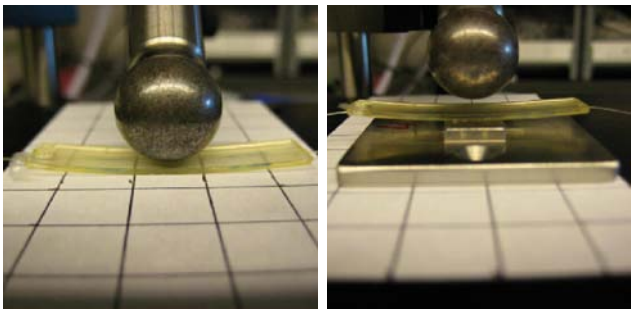

(a) (b)

Figure 7.18: (a) Transverse load setup to test the Ormocer samples. (b) Because of the bend in the Ormocer samples, tests are also performed with a small block placed under the sample to ensure stable positioning.

The samples are tested in two different ways, as shown in Fig. 7.18. The extra-block is used to ensure that force is applied on the most stable position of the sample. The position of the sample is maintained by fixing both fiber ends to the translation stage. However, in between different tests and switching between the two setups, the position of the sample changed. For this reason the cross section is made with respect to 'relative positions'.

The reflection spectra of the FBG sensors fabricated in two Type 3 PCFs and embedded in Ormocer are shown in Fig. 7.19. Both spectra show a shift of about 5 - 6 nm for the Bragg peaks to shorter wavelengths, while the peak separation remains the same. The equal shifts of the Bragg peaks indicate that the embedding results in an axial compression of the FBG.

A transverse load test is performed on both samples, with both setups as shown in Fig. 7.18. The resulting cross sections for the first sample are shown in Fig. 7.20. Both curves clearly show a Gaussian-like profile, with an enhanced sensitivity at the position of the grating. The maximum change in Bragg peak wavelength is about 74 pm for the mode polarized along the fast axis, and this was the same for both test methods. The Gaussian fits in Fig. 7.20(a) show a small difference in sensitivity between modes polarized along the fast and slow axis, with a maximum change in Bragg peak wavelength of 74 pm and 66 pm, respectively. This can be an indication that the distinct peak behaviour of the free standing sensor under transverse line loading is translated to the sensor embedded in Ormocer.

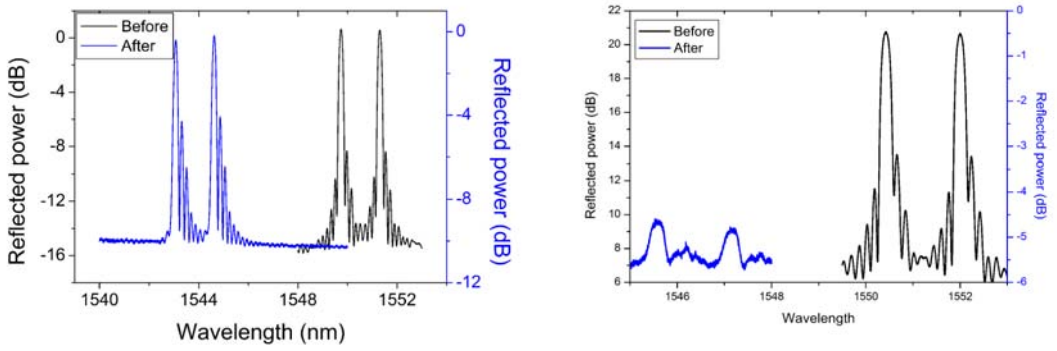

(a) (b)

Figure 7.19: Reflection spectra of an FBG sensor fabricated in a Type 3 PCF, before and after embedding in an Ormocer skin sample ((a) Sample 1 and (b) Sample 2). The spectrum of Sample 2 is of low quality due to a bad optical connection.

The $FWHM$ also shows some small difference both Bragg peaks measured with both test methods. The obtained values lie between 2.2 mm and 2.6 mm.

The cross sections corresponding to the transverse strain tests performed on the second Ormocer sample with a Type 3 PCF embedded, are shown in Fig. 7.21. Both plots show again a Gaussian like profile with an increased sensitvity at the position of the grating. In Fig. 7.21(a), the mode polarized along the slow axis has the highest change in Bragg wavelength (50 pm versus 37 pm). The $FWHM$ for the Gaussian fit, is about 2.33 mm and 2.04 for both Bragg peaks.
Fig. 7.21(b) shows the same trend, with the highest sensitivity for the mode polarized along the slow axis. The corresponding Gaussian fit has a maximum of 64 pm and a $FWHM$ of 1.93 mm. The Gaussian fit of the sensitivity of the mode polarized along the fast axis, has a maximum of 48 pm and a $FWHM$ of 2.18 mm.

The same tests are performed on two Type 2 PCFs embedded in Ormocer. The reflection spectra of the Bragg gratings before and after embedding are shown in Fig. 7.22(a) and Fig. 7.22(b). Both spectra show large deformations due to embedding. Fig. 7.22(a) shows a splitting of the peaks which can be an indication that one part of the grating sees more axial strain than the other part, and as such are two gratings present with each a different Bragg wavelength. The largest peaks are followed during testing.
The spectrum in Fig. 7.22(b) shows that much deformations that the Bragg peaks are barely recognizable and the indicated peaks are assumed to be the Bragg peaks.

The resulting cross-sections from the transverse load tests on Sample 1 (Fig. 7.22) with the

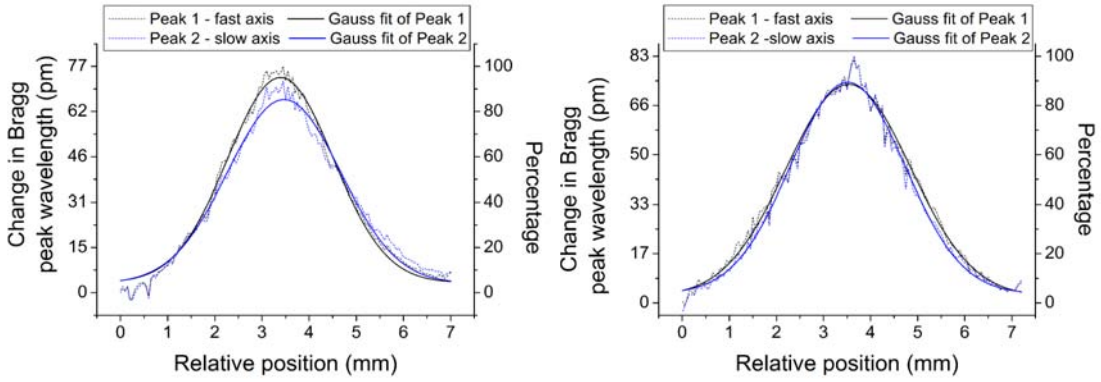

(a) (b)

Figure 7.20: Cross section of the transverse load sensitivity at the center of Sample 1 of the Type 3 PCF embedded Ormocer. skin. The curves shown in (a) are obtained with the setup as shown in Fig. 7.18(a) and a Gaussian fit leads to $FWHM_{Peak1} = 2.23$ mm and $FWHM_{Peak2} = 2.39$ mm. The curves shown in (b) are obtained with the setup as shown in Fig. 7.18(b) and a Gaussian fit leads to $FWHM_{Peak1} = 2.63$ mm and $FWHM_{Peak2} = 2.43$ mm.

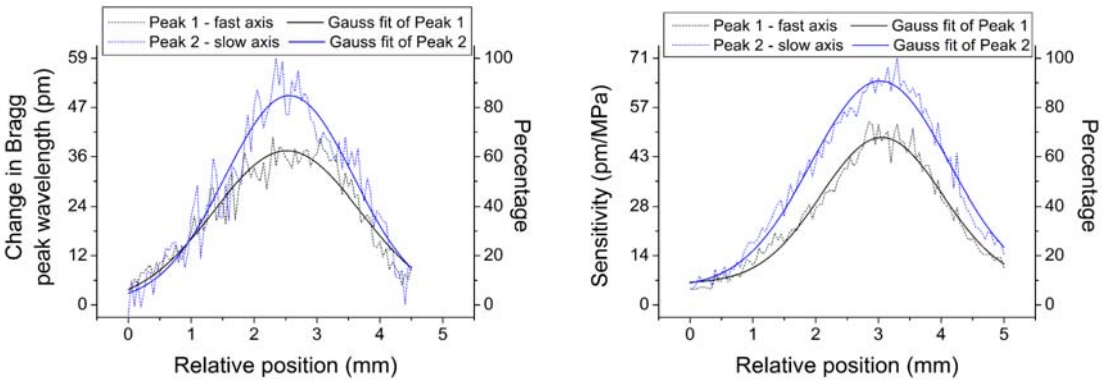

(a) (b)

Figure 7.21: Cross section of the transverse load sensitivity at the center of Sample 2 of the Type 3 PCF embedded Ormocer. skin. The curves shown in (a) are obtained with the setup as shown in Fig. 7.18(a) and a Gaussian fit leads to $FWHM_{Peak1} = 2.33$ mm and $FWHM_{Peak2} = 2.04$ mm. The curves shown in (b) are obtained with the setup as shown in Fig. 7.18(b) and a Gaussian fit leads to $FWHM_{Peak1} = 1.93$ mm and $FWHM_{Peak2} = 2.18$ mm.

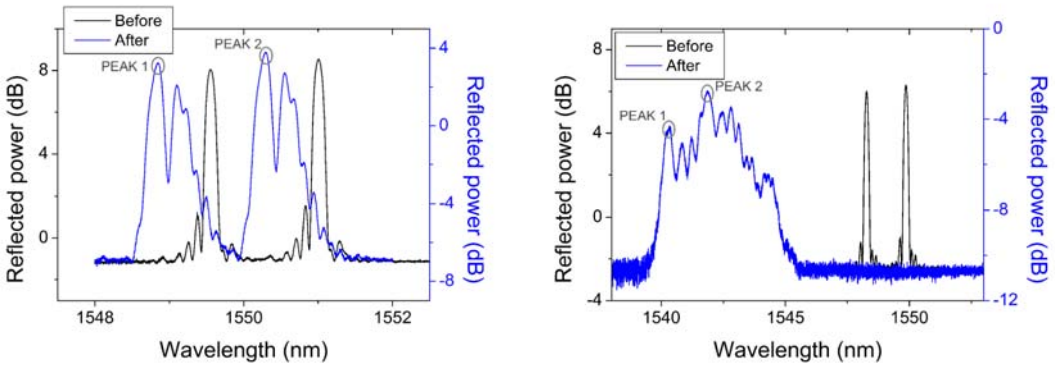

(a) (b)

Figure 7.22: Reflection spectra of an FBG sensor fabricated in a Type 2 PCF, before and after embedding in an Ormocer skin sample ((a) Sample 1 and (b) Sample 2).

setups as depicted in Fig. 7.18 are shown in Fig. 7.23. A Gaussian like profile is again obtained, which corresponds to an increased sensitivity at the position of the grating.
The Gaussian fits in Fig. 7.23(a) have a maximum change in Bragg peak wavelength of 120 pm and 117 pm for the modes polarized along the fast and slow axis, respectively. The $FWHM$ is for both fits about 2.16 mm.
Fitting the curves shown in Fig. 7.23(b) with a Gaussian distribution leads to a maximum change in Bragg peak wavelength of 128 pm and $FWHM$ of 2.17 mm for the mode polarized along the fast axis. For the mode polarized along the slow axis, the maximum change in Bragg peak wavelength is 124 pm and the $FWHM$ is 2.22 mm.

Due to too much deformation of the second sample, it was impossible to perform transverse loading tests while keeping it stable. Lowering the weight of the metal ball on the sample, caused the sample to tilt, resulting in large axial strains on the fiber. This made it impossible to link the Bragg peak behaviour to induced transverse strains.

7.4 Conclusion

Simulations of a bow-tie fiber and Type 3 PCF embedded in polymer tubes, showed that the transverse line load sensitivity decreases when a polymer with high elastic modulus is used. They also showed that the sensitivity of the sensors is about an order of magnitude when embedded. The influence of the Poisson ratio was also investigated with FEM simulations, and this showed that the sensitivity is higher for polymers with a higher Poisson ratio. This effect was however small compared to the contribution of the elastic modulus.

Experiments were performed on FBG sensors fabricated in bow-tie fibers and embedded in

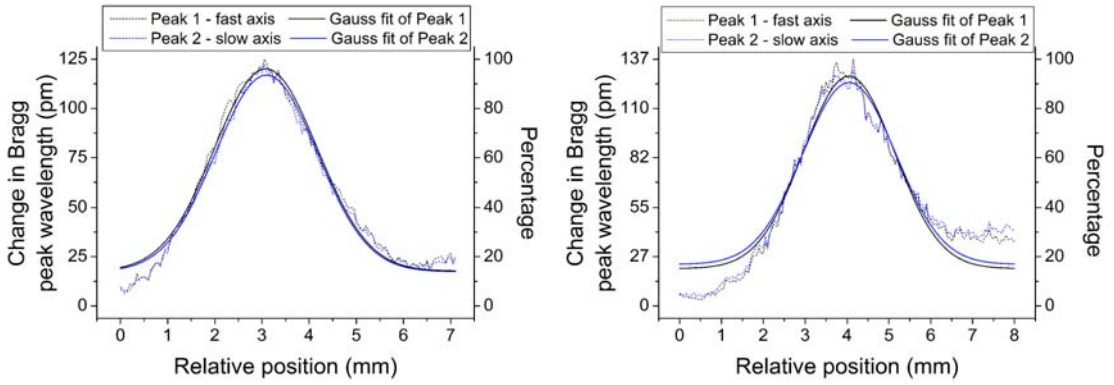

Figure 7.23: Cross section of the transverse strain sensitivity of Sample 2 of the Type 3 PCF embedded Ormocer. skin. The curves shown in (a) are obtained with the setup as shown in Fig. 7.18(a) and a Gaussian fit leads to $FWHM_{Peak1} = 2.18$ mm and $FWHM_{Peak2} = 2.15$ mm. The curves shown in (b) are obtained with the setup as shown in Fig. 7.18(b) and a Gaussian fit leads to $FWHM_{Peak1} = 2.17$ mm and $FWHM_{Peak2} = 2.22$ mm.

polymer tubes. Two types of polymers were tested: a PMMA tube and a tube made of a MMA/BuMA 50/50 composition which is more flexible than a pure PMMA tube. A third type of polymer tube (MMA/EHMA 50/50) with an even higher flexibility was also provided for testing, but the sample itself was too heavily deformed because it was that soft.
The obtained sensitivity of the peak separation of the PMMA tube was comparable with the simulated results for a polymer of elastic modulus of 3 GPa and a Poisson ratio of 0.35. It is thus likely that these are approximately the material properties of the tested PMMA sample. The maximum sensitivity of the peak separation was -8.3 pm/(N/mm) for a load applied along the fast axis.
The reflection spectrum of the MMA/BuMA 50/50 sample was heavily deformed due to uneven strains on the grating. This made it difficult to detect the Bragg peaks and the obtained sensitivities are only an indication for the order of magnitude. The maximum sensitivity of the peak separation of this sample was about 18 pm/(N/mm), which is higher than the sensitivity of the PMMA sample. This corresponds to the conclusion drawn from the simulations: FBG sensors fabricated in bow-tie fibers have a higher transverse line load sensitivity when embedded in a polymer with a low elastic modulus.

FBG sensors fabricated in Type 2 and Type 3 PCFs were also embedded in polymer skins. The tested polymers were PDMS, which is a rather soft and flexible material, and Ormocer, a more rigid polymer. Embedding FBG sensors in both types of polymer was possible, but for some of the fabricated Ormocer samples the reflection spectrum was heavily deformed

after embedding. This is likely the result of an uneven distribution of residual strains in the fabricated sample.
Two sensors fabricated in a Type 2 and Type 3 PCF, were embedded together in a PDMS sample. The maximum change in Bragg peak wavelength was 94 pm for the sensor in a Type 2 PCF, while the sensor in a Type 3 PCF resulted in a maximum change in Bragg peak wavelength of only 32 pm. This large difference in sensitivity is likely the result from different orientations along which they are embedded. For both sensors, there was no different peak behaviour for both Bragg peaks and the $FWHM$ was about 1.4 mm.
The testing of the Ormocer sample also resulted in a larger change in Bragg peak wavelength for the sensor fabricated in a Type 2 PCF than for a sensor fabricated in a Type 3 PCF (maximum 128 pm opposed to maximum 74 pm). However, for the sensors fabricated in a Type 3 PCF, there was a different behaviour for both Bragg peaks, with a maximum change in Bragg peak separation of about 16 pm. The $FWHM$ was found to be around 2.2 mm for all tested Ormocer samples.

The sensitivities found for the Ormocer and PDMS samples cannot be compared directly, because the orientation of the fiber is not known and the skins have a different sample thickness and embedding depth of the fiber. The combination of experimental testing with (3D) FEM simulations will be important to be able to draw reliable conclusions.
From the testing of the polymer skins it also became clear that the uniformity of the sample is of high importance. Flaws like surface irregularities, bending of the sample or fiber, air-bubbles and others, made it difficult to obtain consistent, and sometimes even reliable, results. Optimization of the embedding procedure is therefore also important.

Chapter 8

Accomplishments and future prospects

The focus of my Master thesis was on fiber Bragg grating sensors fabricated in highly birefringent photonic crystal fibers. The specific goal was to obtain a temperature insensitive sensor that has a high mechanical strain and hydrostatic pressure sensitivity. This sensor could be used in its bare state, but the applications of interest in this work were structural health monitoring and smart materials that rely on embedded sensors. Fiber optic sensors are beneficial to both applications because of their advantages including compact dimensions, low weight and multiplexing capabilities. But the envisioned sensors could bring even more added value. One can think of monitoring loading and damage in the transverse direction of composite materials, which up to now has been impossible to achieve with satisfactory resolution. Another application where the investigated sensors have distinct advantages is in so-called artificial optical skins. These flexible polymer foils can be wrapped around or attached to an irregular and moving object, with the intention to monitor a pressure distribution on the surface. This would be of particular interest inthe field of robotics to provide a sense of touch to humanoid or social robots, or in the field of healthcare to provide pressure monitoring and relief in prosthesis sockets.

My Master thesis tackled several challenges. First, we calibrated an FBG sensor that was specially designed to have a high mechanical strain and hydrostatic pressure sensitivity and low temperature sensitivity. Subsequently we embedded this sensor in a composite material and we characterized the fabricated samples for several mechanical loading conditions. Finally, we also embedded the sensors in polymer foils and we determined the influence of different material parameters on the sensitivity of the embedded sensor. The characterization tests we performed were experiments as well as 2D finite element analyses, and we compared the obtained results.
An overview of the conclusions is given below.

8.1 Accomplishments

8.1.1 Calibration of the bare sensor

We inscribed fiber Bragg gratings in specially designed highly birefringent photonic crystal fibers. The results from a thermal cycling test, evidenced that the fabricated sensors are highly insensitive to temperature changes. Temperature insensitivity was one of the requirements of the sensor concept that we envisioned.
Via 2D finite element analyses, we found that the sensor has a hydrostatic pressure sensitivity of -1.47 pm/bar, and this values corresponds to experimental values we obtained earlier. **A fiber Bragg grating sensor with a hydrostatic pressure sensitivity of -1.47 pm/bar has not been reported before and almost matches the industry requirements of 2 pm/bar.**
We investigated the transverse line load sensitivity of the sensor via experiments and 2D finite element analyses and found a maximum sensitivity of -372 pm/(N/mm) and -325 pm/(N/mm) for the experiments and simulations, respectively. Since the obtained sensitivities are comparable, we conclude that the model used for the 2D finite element analyses is valid to simulate the sensitivity of the real sensor. Moreover, this very high transverse line load sensitivity also implies that the sensor can be used as a temperature insensitive sensor with high mechanical strain sensitivity.

8.1.2 Embedding of the sensor in composite materials

We successfully embedded the sensors in the middle of carbon fiber/epoxy laminates with a cross-ply layup of 16 layers. The reflection spectra of the sensors after embedding showed that the Bragg peak separation had decreased due to the presence of residual strains in the fabricated laminates, but this did not interfere with the Bragg peak analyses. Additionally, we studied the cross sections of the fabricated samples to conclude that the orientation of the sensor is well maintained in the embedding procedure.
We performed a thermal test evidencing that once embedded and as expected the sensor is no longer insensitive to temperature with an average sensitivity of 4.4 pm/°C. This sensitivity stems from residual stresses inside the laminate that decrease during heating and increase again while cooling down. To meet the requirements of temperature insensitive load monitoring, the sensor could be doped such that it becomes sensitive to temperature changes in its bare form, but compensates for the differences in thermal expansion coefficients when embedded. This would allow monitoring the true strains in the laminate.
The transverse strain tests we performed resulted in a sensitivity of -0.16 pm/$\mu\varepsilon$. **This sensitivity is an order of magnitude larger than earlier reported values** for sensors fabricated in other types of highly birefirngent fibers and embedded in a carbon fiber/epoxy laminate with unidirectional layup.

The high mechanical line load sensitivity of the bare sensor is a true added value when embedded in composite materials, and the transverse strain sensitivity we obtained is a breakthrough for monitoring loading of FRP materials.

8.1.3 Embedding of the sensor in flexible polymers

We also embedded the sensors in flexible polymers. Experiments and simulations of a sensor embedded in a polymer tube showed that a higher transverse line load sensitivity is achieved when the polymer has a lower elastic modulus. Tests we performed on the sensors embedded in a polymer foil showed that there is an increased sensitivity at the position of the embedded sensor. The sensitivity of the Bragg peak separation was low compared to the sensitivity of the separate Bragg peaks, which indicates that the high transverse line load sensitivity of the bare sensor does not necessarily provide a high load sensitivity when embedded in a (flexible) polymer skin. However, the experiments showed that when the sensitivity of the Bragg peaks is considered, **the embedded sensor can be used for distributed pressure sensing.**

8.2 Future prospects and challenges

The tested photonic crystal fibers had a highly asymmetric microstructure that consisted of several large airholes which were deformed due to fabrication. The slightest deviation in the design of a single mode and bend insensitive microstructured fiber will result in multimode behaviour or high bending losses. Although the tested fibers had a very high mechanical strain sensitivity, an improvement would be a fiber with the same or higher sensitivity that is less affected by fabrication induced imperfections.
As the microstructured fibers have a transverse strain sensitivity that is dependent on angular orientation, the orientation of the highest sensitivity should be indicated in some way. An option is to make the outer cladding hexagonal to limit the angular orientations of the fiber to three possibilities. The principle of a D-clad fiber could also be applied to the photonic crystal fibers. Both options would significantly ease control of the orientation of the fibers during embedding.

When the sensor was embedded in a composite material it was no longer insensitive to temperature changes due to the presence of residual strain in the fabricated cross-ply laminate. This implies that another compensating system should be used in strain monitoring of composite samples. A commonly used method is the co-embedding of a sensor that is placed in a capillary.
Although the embedding of an optical fiber in fiber reinforced polymers did not induce significant disturbances to the structure of the composite, fibers with a smaller diameter should be considered. This will result in a more reliable monitoring of the real internal strains, and not the strains induced by the presence of the optical fiber.

One of the difficulties of embedding optical fibers in composite materials, was the combination of a very brittle fiber that had to be embedded in a rigid laminate with a harsh fabrication process. Questions may arise about the possibilities of embedding optical fibers with other techniques than the autoclave and in other configurations than small rectangular samples. These large hurdles will have to be overcome before even thinking of embedding photonic crystal fibers on a large scale in composite structures.
Besides the experimental work, 3D FEM simulations could also reveal possible improvements. The influence on the sensitivity of parameters like embedding depth and laminate layup could indicate what samples should be considered for fabrication and experimental testing.

As the research domain of optical skins is still very young, there are still many effects that have to be investigated and problems that have to be solved before a comparative study can be made of the sensitivity of different types of fibers. First of all, 3D simulations of optical skins with different material and geometrical properties should be performed.
A second step is to optimize the embedding procedure such that testing of several samples fabricated in the same manner produce consistent results. The (surface) quality of the polymer, the orientation of the fiber and the adhesion between polymer and fiber will heavily influence the sensitivity of the sensor. Once this is optimized, the spatial resolution of larger skin samples could be tested including their ability to distinguish multiple forces.
Other experiments like thermal tests, axial and bending strain tests should also be performed on several types of optical skins.

The use of microstructured polymer optical fibers could resolve several problems associated with silica fibers [38]. They have the advantage of being mechanically very flexible and their fabrication process is much more tolerant. Polymers preforms could be made with the stack-and-draw technique, but also by polymer casting, extrusion or injection moulding. The fibers are drawn at a temperature of about 150 - 200 °C and due to this low temperature, the shape of the airholes is well maintained after drawing. Much more complex microstructures are therefore possible. The fiber is also much less affected by fluctuations of fabrication parameters like temperature, which could make it possible to fabricate them at low cost in large volumes.
Polymers can be modified by including molecular components or atomic species. This would open the door to a whole new class of fiber optic sensors in which a chemical reaction between the polymer fiber and a certain molecule induces a change in material properties of the fiber.

An application in which polymer fibers could be an improvement over silica fibers, is in the domain of structural health monitoring [39]. First of all is the possible low cost fabrication of polymer fibers an important economical factor in distributed sensing systems. Moreover, as the material properties of the polymer can be tuned to the specific applications, fiber Bragg grating sensors can be made that can endure large strains. However, considerable additional

research is required on the fabrication of such microstructured fiber sensors and the inscription of Bragg gratings in these fibers, since this requires different techniques than for silica fibers. Although the domain of polymer optical fibers is still very young, it is clear that they will offer a wide range of advantages and will definitely gain importance in the coming years. Moreover, the developed sensor concept presented in this thesis can be transferred to microstructured polymer fibers.

8.3 Conclusion

During my Master thesis, we have clearly shown the potential of fiber Bragg grating sensors in their bare state and as sensing elements in smart materials. The results we obtained greatly advance on the state-of-the-art and will be taken up in international journal publications. With this I hope to have contributed to the development of fiber optic sensors and smart materials that rely on embedded optic fiber sensors.

Appendix A

Comsol Multiphysics

A.1 Finite Element Method

Several properties and sensitivties of photonic crystal fibers presented in this thesis, have been derived using Finite Element Method (FEM) analyses. FEM is a very versatile and flexible technique that can be used to solve complicated structural, thermal, semiconductor and electromagnetic problems. It is especially advantageous for electromagnetic field problems in waveguides with an arbitrarily shaped cross section composed of several materials. FEM divides the cross section of a fiber into a patchwork of triangular elements with different shape, size and refractive index. [40]

The formulation of the FEM is based on the vector wave equation or curl-curl equation, which is given by equation (A.1) for a medium described by the complex tensors of the relative dielectric permittivity $\overline{\overline{\varepsilon}}_r$ and magnetic permeability $\overline{\overline{\mu}}_r$. In this equation $\overline{h}$ is the magnetic field and $k_0 = 2\pi/\lambda$ is the wave number in vacuum. [15]

$$\overline{\bigtriangledown} \times \left(\overline{\overline{\varepsilon}}_r^{-1} \overline{\bigtriangledown} \times \overline{h} \right) - k_0^2 \overline{\overline{\mu}}_r \overline{h} = 0 \tag{A.1}$$

The magnetic field of the modal solution is expressed as $\overline{h} = \overline{H} e^{-\gamma z}$, with $\overline{H}$ the magnetic field distribution on the transverse plane and $\gamma = \alpha + j k_0 n_{eff}$ the complex propagation constant with α the attenuation and n_{eff} the refractive index. In order to make the field components continuous over the whole domain, a first degree polynomial interpolation is assumed between the field values at the cross points of the triangles. [40]
Equation (A.1) leads to equation (A.2) when the variational finite element procedure is applied. {H} is the discretized magnetic field-vector distribution of the mode, and $[A]$ and $[B]$ are sparse and symmetric matrices. [15]

$$\left([A] - \left(\frac{\gamma}{k_0} \right)^2 [B] \right) \{H\} = 0 \tag{A.2}$$

The advantage of the variational procedure is that it can automatically satisfies the boundary conditions when left free ('natural boundary condition'). To reduce the computational domain, the boundary conditions can be changed to reduce the matrix order. For instance, when the cross section of the waveguide has a plane of symmetry, advantage of that should be taken. Another example is when the vector wave equation only has to be solved in the core of a fiber, because one knows that the modes are located here. In order to enclose the computational domain without affecting the numerical solution, Perfectly Matched Layers (PML) are placed before the outer boundary. The PML are also used to calculate waveguide losses. [40], [41]

FEM analyses of photonic crystal fibers lead to knowledge regarding their propagation characteristics and field distributions. Extensive waveguide analyses can be performed by varying the material properties or fabrication parameters. Since the mechanical parameters are also taken into account, FEM can be used to analyse the sensitivity of the fiber to influences like hydrostatic pressure, axial and transverse strain. More complex structures like fibers embedded in different materials are also possible to model.
In this work, 2D FEM calculations were performed using the commerical available Comsol Multiphysics with RF and structural mechanics modules. Analyses were performed to model the material and modal birefringence of a fiber and to calculate the sensitivity of the fibers to hydrostatic pressure and transverse strain. The details regarding these simulations are discussed in more detail in the following sections.

A.2 Birefringence analyses

A plane strain analysis combined with a perpendicular hybrid-mode wave analysis was performed to study the birefringence of a fiber. The model consisted out of the cross section of the fiber with correct material properties assigned to different regions. The materials considered for fibers are isotropic, and parameters like elastic modulus, poisson ratio and thermal expansion coefficient had to be set. Thermal stresses are taken into account by setting the reference temperature for the thermal expansion coefficient, and the temperature at which the simulation is performed. This reference is taken to be 20 °C in all performed simulations, unless noted otherwise.
Optical properties like the considered wavelength, stress-optic coefficients and refractive index of the material were also some of the required parameters.
This model divided in triangular elements which is also called 'meshing'. A PML was placed around the core region, with an increased number of elements inside the PML to improve the precision. To reduce the computational domain, the domain of the optical analyses was restricted to the PML. In Fig. A.1, the different steps of a FEM analysis are shown.

The birefringence analysis started with a plane strain analyses to calculate the fabrication

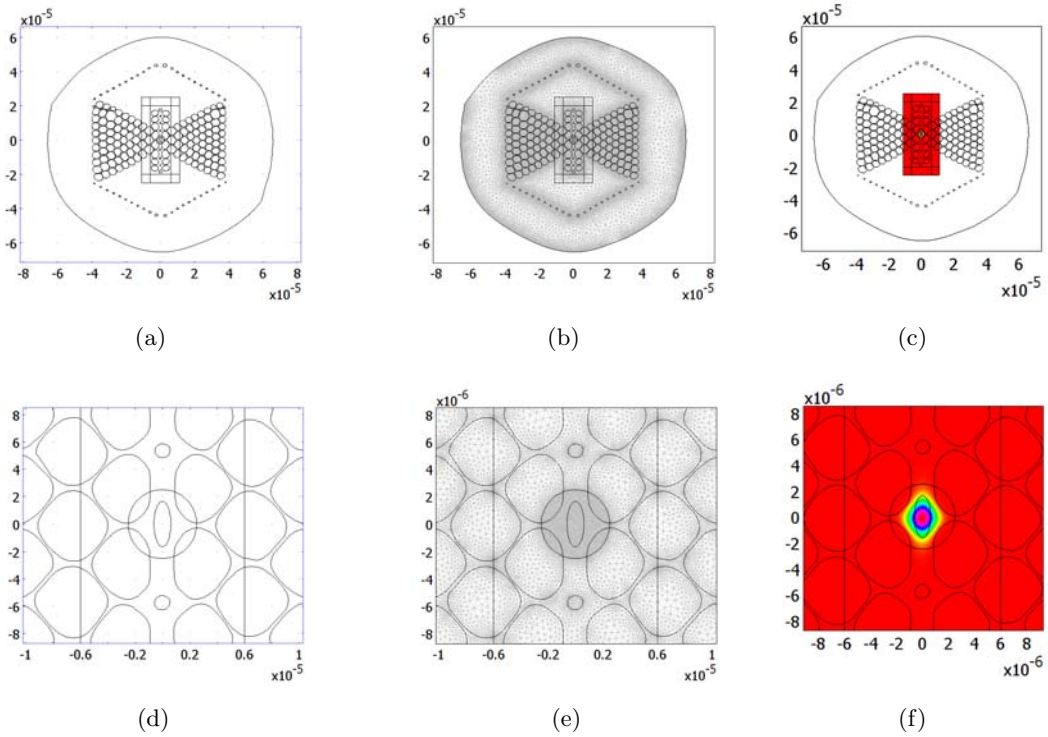

Figure A.1: Different steps of a 2D FEM analysis: (a and d) A geometrical model with the correct material parameters and a rectagular PML is built. (b and e) This model is divided in a mesh of triangular elements with varying shape and size. (c and f) After the simulations, different properties, such as the mode profile, can be plotted.

induced stresses. These thermal stresses are the result from different thermal expansion coefficients and lead to material birefringence. The next step was an optical analyses that is based on the previous calculated stresses, but also takes waveguide birefringence into account. This leads to effective refractive indices of the two fundamental modes and the corresponding modal birefringence of the fiber.

A.3 Hydrostatic pressure sensitivity

The analyses of the sensitivity of a fiber to hydrostatic pressure is much comparable to the birefringence analysis. The only difference is that during the mechanical simulations, a hydrostatic pressure is applied to the outercladding of the fiber. This pressure will change the internal stress distribution in the fiber cross section, and thus result in a change in material and modal birefringence. This can be repeated for several hydrostatic pressure, to obtain a sensitivity of the birefringence to pressure.

A.4 Transverse strain sensitvity

Like in the analyses of the pressure sensitivity, the transverse strain sensitivity of a fiber is determined by applying a force in the mechanical simulation. Transverse strain is simulated by applying a point force to the fiber, and fixing the point on the other side of the fiber in both directions (constraint in x and y direction). This load will lead to a change in the stress distribution and thus also in material and modal birefringence. The simulation can be performed for several values of the point force and for point forces applied to several orientations of the fiber. This results in a plot of transverse strain sensitvity versus orientation of the fiber.

Bibliography

[1] K. T. V. Grattan and Dr. T. Sun, "Fiber optic sensor technology: an overview", *Sensors and actuators*, vol. 82, pp. 40–61, 2000.

[2] B. Culshaw, "Optical fiber sensor technologies: Opportunities and - perhaps - pitfalls", *Journal of lightwave technology*, vol. 22, no. 1, pp. 39–50, 2004.

[3] W. Ecke, *Applications of fibre Bragg grating sensors*, IPHT Jena - tutorial, 2008.

[4] K.H. Haase, *Characterization of HBM fibre optic strain sensors for experimental stress analysis*, COST Action 299 - tutorial, 2007.

[5] B. Culshaw, "Optical fiber sensors", *Nature Photonics*, vol. 2, pp. 143–158, 2008.

[6] R. H. Habel, "COST Action 299 - Guideline for use of fibre optic sensors", pp. 1–11, 2009.

[7] G. Akhras, "Smart Materials and Smart Systems for the Future", *Optics Communications*, pp. 25 – 31, 2000.

[8] W. De Waele, *Structural monitoring of composite elements using optical fibres with Bragg-sensors*, University of Ghent, 2002.

[9] "http://www.sensorprod.com", consulted on May 14, 2010.

[10] Y. L. Park et al., "Force Sensing Robot Fingers using Embedded Fiber Bragg Grating Sensors and Shape Deposition Manufacturing", *IEEE International Conference on Robotics and Automation*, pp. 1510–1516, 2007.

[11] J. Missinne and B. Van Hoe, "Artificial skin based on flexible optical tactile sensors", *SPIE Newsroom*, pp. 1–3, 2010.

[12] R. Kashyap, *Fiber Bragg Gratings*, Academic Press, 1999.

[13] T. Erdogan, "Fiber Grating Spectra", *Journal of lightwave technology*, vol. 15, pp. 1277–1294, 1997.

[14] K.T.V. Grattan and B.T. Meggit, *Optical fiber sensor technology*, Kluwer Academic Publishers, 2000.

[15] F. Poli et al., *Photonic Crystal Fibers: Properties and Applications*, Springer, 2007.

[16] P. St.J. Russell, "Photonic-Crystal Fibers", *Journal of lightwave technology*, vol. 24, no. 12, pp. 4729–4749, 2006.

[17] J. C. Knight, "Photonic Crystal Fibres", *Nature*, vol. 424, pp. 847–851, 2003.

[18] O. Frazao et al., "Optical sensing with photonic crystal fibers", *Laser and Photonics Reviews*, vol. 2, no. 6, pp. 449–459, 2008.

[19] H.R. Sørensen et al., "Liquid filling of photonic crystal fibres for grating writing", *Optics Communications*, vol. 270, pp. 207–210, 2007.

[20] J. Canning et al., "Gratings in structured optical fibres", *Laser Chemistry*, 2008.

[21] E. Chehura et al., "Characterization of the response of fibre Bragg gratings fabricated in stress and geometrically induced high birefringence fibres to temperature and transverse load", *Smart Materials and Structures*, vol. 13, pp. 888–895, 2004.

[22] G. Luyckx, *Multi-axial strain monitoring of fibre reinforced thermosetting plastics using embedded highly birefringent optical fibre Bragg sensors*, University of Ghent, 2010.

[23] W. Urbanczyk et al., "Photonic crystal fibers: new opportunities for sensing", *Proceedings of SPIE*, vol. 6619, 2007.

[24] T. Nasilowski et al., "Temperature and pressure sensitivities of the highly birefringent photonic crystal fiber with core asymmetry", *Applied Physics B: Lasers and Optics*, vol. 81, pp. 325–331, 2005.

[25] T. Martynkien et al., "Measurements of sensitivity to hydrostatic pressure and temperature in highly birefringent photonic crystal fibers", *Opt Quant Electron*, vol. 39, pp. 481–489, 2007.

[26] C. M. Jewart et al., "Ultrafast femtosecond-laser-induced fiber Bragg gratings in air-hole microstructured fibers for high-temperature pressure sensing", *Optics letters*, vol. 35, no. 9, pp. 1443–1445, 2010.

[27] C. Jewart et al., "Sensitivity enhancement of fiber Bragg gratings to transverse stress by using microstructural fibers", *Optics letters*, vol. 31, no. 5, pp. 2260–2262, 2006.

[28] T. Geernaert et al., "Transversal Load Sensing With Fiber Bragg Gratings in Microstructured Optical Fibers", *IEEE Photonics Technology Letters*, vol. 21, no. 1, pp. 6–8, 2009.

[29] K. S. C. Kuang et al., "Embedded fibre Bragg grating sensors in advanced composite materials", *Composites Science and Technology*, vol. 61, pp. 1379–1387, 2001.

[30] G. Luyckx et al., "Response of FBGs in Microstructured and Bow Tie Fibers Embedded in Laminated Composite", *IEEE Photonics Technology Letters*, vol. 21, no. 18, pp. 1290–1292, 2009.

[31] G. T. Kanellos et al., "Two dimensional polymer-embedded quasi-distributed FBG pressure sensor for biomedical applictions", *Optics Express*, vol. 18, no. 1, pp. 179–186, 2009.

[32] R. Guan et al., "Stress birefringence analysis of polarization maintaining optical fibers", *Optical Fiber Technology*, vol. 11, pp. 240–254, 2005.

[33] T. Geernaert et al., "Fiber Bragg Gratings in Germanium-Doped Highly Birefringent Microstructured Optical Fibers", *IEEE Photonics Technology Letters*, vol. 20, no. 8, pp. 554–556, 2008.

[34] T. Nasilowski, F. Berghmans with input from WRUT, and UMCS, "PHOSFOS Deliverable Report D1.1", 2008.

[35] S. Sulejmani, *FOS&S internship report*, VUB, 2009.

[36] Y. Namihira, "Opto-elastic constant in single mode optical fibers", *Journal of lightwave technology*, vol. LT-3, no. 5, pp. 1078–1083, 1985.

[37] E. Ferraris et al., "Embedding of fibre optic sensors within flexible host", *International Conferences on Multi-Material Micro Manufacture*, 2009.

[38] M. A. van Eijkelenborg et al., "Microstructured polymer optical fibre", *Optics Express*, vol. 9, no. 7, pp. 319–327, 2001.

[39] K. S. C. Kuang et al., "Plastic Optical Fibre Sensors for Structural Health Monitoring: A Review of Recent Progress", *Journal of sensors*, vol. 2009, no. 312053, pp. 1–13, 2009.

[40] B. M. A. Rahman, "Finite element analysis of optical waveguides", *Progress in Electromagnetic Research*, vol. 10, pp. 187–216, 1995.

[41] S. Selleri et al., "Complex FEM modal solver of optical waveguides with PML boundary conditions", *Optical and Quantum Electronics*, vol. 33, pp. 359–371, 2001.

List of abbreviations

BuMA	butyl methacrylate
CFRP	carbon fiber reinforced polymers
EHMA	2-ethylhexyl methacrylate
EM	electromagnetic
FBG	fiber Bragg grating
FEM	finite element method
FRP	fiber reinforced polymers
FWHM	full width at half maximum
HiBi	highly birefringent
MMA	methyl methacrylate
MSF	microstructured fiber
ORMOCER	organically modified ceramic
PCF	photonic crystal fiber
PDMS	polydimethylsiloxane
PMMA	polymethyl methacrylate
SHM	structural health monitoring

List of Symbols

Λ	period
λ	wavelength
λ_{B}	Bragg peak wavelength
$\Delta\lambda_{\mathrm{B}}$	Bragg peak separation
$\delta\lambda_{\mathrm{B}}$	change in Bragg peak wavelength
B	birefringence
n	refractive index
C	stress-optic coefficient
β	propagation constant
v	phase velocity
k	free-space wavenumber
E	elastic modulus
G	shear modulus
ν	Poisson ratio
σ	stress
ε	strain
p	strain-optic coefficient
α	thermal expansion coefficient
T	temperature